Nanobits - exchangable and customisable scanning probe tips

Yildiz, Izzet

Publication date:
2014

Document Version
Publisher's PDF, also known as Version of record

Technical University of Denmark
Department of Micro- and Nanotechnology

NANOBITS

EXCHANGEABLE AND CUSTOMISABLE SCANNING PROBE TIPS

Thesis by

IZZET YILDIZ

In Partial Fulfilment of the Requirements for the Degree of
Doctor of Philosophy

30 June 2014

Dedicated to my grandparents İsa and Hamiş,

and

to those who lost their lives during the Gezi Park protests in 2013

Preface

This thesis has been submitted in partial fulfilment of the requirements for the degree of Ph.D. The main part of the presented work was conducted at Department of Micro- and Nanotechnology at the Technical University of Denmark (DTU Nanotech). A smaller part of the project was carried out at the Institute for Information Technology (OFFIS) at the Carl von Ossietzky University of Oldenburg.

I would like express my gratitude to the following great people who contributed to this work:

First and foremost, I am amply grateful to my supervisor Peter Bøggild for the opportunity of working with him in the friendly and productive environment he created in the Nanocarbon group. I would like to thank him for his guidance and invaluable support during the course of this project.

I am thankful to clever people of the Nanocarbon group for always being fun, helpful and encouraging. Special thanks should go to Alexey Savenko, Dirch Hjorth Petersen, Timothy J. Booth and Alberto Cagliani for the fruitful discussions.

I gratefully acknowledge the OFFIS staff for the innovative and productive experiments we conducted together, and also for welcoming us and offering a friendly environment; especially Volkmar Eichhorn, Malte Bartenwerfer, Florian Krohs, and Albert Sill.

I am indebted to Danchip staff for their invaluable help and open-mindedness. Above all, I should mention Louise Jørgensen, Helle Vendelbo Jensen, Karen Birkelund, Peixiong Shi, Tine Greibe, Berit Geilman Herstrøm, Thomas Aarøe Anhøj, Mikkel Dysseholm Mar, Pernille Voss Larsen, Katharina Nilson, Elena Khomtchenko, Yvonne Gyrsting, Conny Hougaard, Jesper Hanberg, Jonas Michael Lindhard**…** briefly everyone.

I also would like to thank the NanoBits project partners NanoWorld (Erlangen, DE), EMPA (Thun, CH), IOF Fraunhofer (Jena, DE) and JPK (Berlin, DE) for sharing knowledge and for the constructive collaboration.

In DTU Nanotech, I should thank: Ole Hansen for the discussions, brainstorming, and for his advices in various subjects; Kristian Mølhave, Eric Jensen, Rolf E. R. Møller-Nilsen for their input and recommendations; Rafal D. Wierzbicki for his help during the microfabrication and for being a wonderful friend.

Finally, I am sincerely thankful to and owe a lot to my friends outside of DTU: Deniz Sanli, Tolga Bagci, Ceren Özgün, Hâldun & Sevilay Sevincli for being there in dire and incredibly fun times; and my family for their never-ending support and encouraging me to always follow the path of my own choosing.

This work was supported by EU FP7 Project NANOBITS (Grant agreement no. 257244).

Abstract

Invention of atomic force microscopy (AFM) pioneered a novel aspect for the surface metrology concept. A range of scanning probe methods have been developed over the years based on different sorts of tip-surface interaction: electrical, optical, thermal, force. Reproducible and fast fabrication of microcantilevers and probes together with alternative probing modes ease AFM's adaptation to altering technological needs. The need to constantly adapt to the ever-altering device architecture and perpetual size shrinkage calls for enhancements to address specific needs, like specialised probes. Device miniaturisation requires the scanning probes to adapt into finer geometries to provide higher lateral resolution. To meet these needs critical dimension AFM (CD-AFM) and deep trench AFM (DT-AFM) were invented, which use different types of AFM tips: high-aspect-ratio tips for DT-AFM and CD tips for CD-AFM. Unfortunately, these advanced tip types are fabricated by vertical means of fabrication which results in low throughput, and thus, high-cost and batch-incompatible processes. Another drawback is the wear problem of the silicon tips which reduces the efficiency since after a certain number of scans, tip diameter becomes wider losing its sharpness. Both changing of the sample (topography) and the blunting of the tips require replacement of the AFM tip with a newer, sharper or application-specific one. AFM can benefit from availability of adequate, surface-specific tips and AFM probes available for *in situ* replacement could greatly increase the efficiency and adaptability of a CD system.

In this PhD study, NanoBits – nano-sized customisable and exchangeable scanning probe tips – were developed to meet the demands of current AFM applications. Two different methods were followed for the fabrication of NanoBits; lateral nanolithography which utilises the focused ion beam milling of freestanding NEMbranes and microfabrication, where the NanoBits and hybrid structures were defined by electron beam lithography. The design of the NanoBits considered challenging application topographies like deep trench and critical dimensions: tips suitable for imaging high-aspect ratio structures and sidewall profiles were designed.

Tip diameters in the order of 30 nm were reproducibly obtained with the FIB milling and the smallest tip diameter achieved was <15 nm, with aspect ratios of 45 being possible. Scanning electron microscope investigation showed that the polycrystalline silicon NanoBits obtained by microfabrication had tip diameters of 15–30 nm at surface but increased to 275 nm along the thickness of the NanoBit, indicating wedge sidewalls. Therefore, post-processing sharpening of the microfabricated NanoBits was tested by physical etching methods: reactive ion etching (RIE), ion beam etching (IBE), and FIB milling. RIE and FIB milling were observed to be promising, resulting in increased overall tip sharpness while IBE experiments were inconclusive.

The out-of-plane bending of NanoBits which would accelerate the assembly process by providing direct picking up of the NanoBits by the AFM probe was investigated. Two different bending mechanisms were studied for out-of-plane bending studies: FIB irradiation- and the residual stress-driven bending in bimorph structures. With FIB irradiation studies, NanoBits were demonstrated to bend close to 90° and to a certain degree window (30°–60°). In addition, it was shown that the bending angle can be adjusted by controlling the irradiation dose. Tip angles varying from ∼25° to ∼130° were achieved by bending due to residual stress in bimorph structures. Further experiments with silicon nitride substrate and their comparison to

theoretical modelling were conducted to understand mechanism and factors in the bending process. The results showed that the main driving force for the bilayer bending is the intrinsic stress built up in the system. It was additionally demonstrated that the tip angle can be fine-tuned by thermal actuation such that up to 150°C the bending is reversible and the NanoBits' angle can be modified within ±10°. At higher temperatures reversal of stress from tensile to compressive, buckling, and changing of surface colour were observed, pointing to silicidation of the structure which may be starting at 170°C.

The fabricated NanoBits were assembled and their performance as AFM probes were tested at OFFIS. The NanoBits were successfully picked up by a microgripper, collected in a cartridge and mounted to an AFM probe. Performances of the assembled high-aspect-ratio NanoBits were investigated by imaging optical gratings. In most cases, the NanoBits showed better performance than the standard pyramid AFM probes, and long scan experiments proved that (i) the NanoBits did not get blunt even after 100 scans (continuous 30 h imaging), and (ii) stiction into the slit on the plateau tip was sufficiently strong. As a result, NanoBits can offer an unprecedented freedom in adapting to ever-altering surface topographies providing fast exchangeability and reliable outcome owing to their low-cost production (per NanoBit) and versatile capabilities.

Dansk resumé

Opfindelsen af Atomic Force Mikroskopet (AFM) har haft en stor indflydelse på overflade metrology. En række scanning probe mikroskopi (SPM) metoder er blevet udviklet over de sidste mange år, baseret på forskellige former for tip-overflade interaktioner, for eksempel elektriske, optiske, termiske og kontakt kræfter. Reproducerbar og hurtig fabrikation af mikro-bjælker og prober sammen med alternative målemetoder har været vigtig for at tilpasse AFM til krav og behov i industrien. Især har den konstante udvikling mod mindre strukturer og mere komplekse arkitekturer af mikro og nanostrukturer ført til krav om fleksible og adaptive probe teknologier, for ikke at tale om prober med mindre dimensioner. Critical dimension AFM (CD-AFM) og deep trench AFM (DT-AFM) blev udviklet netop til karakterisering af industrielle mikro og nanostrukturer, som f.eks. computer chips. Desværre er mange af disse specielle probe typer fremstillet ved upraktiske og langsomme metoder, hvilket gør prisen høj. En anden ulempe er slid på silicium tips som reducerer opløsning efter mange scans. AFM metrologi har brug for tips der kan tilpasses forskellige overflader, og her er det nærliggende at undersøge om udskiftelige prober kan øge og forbedre effektiviteten og kvaliteten af f.eks. et Critical Dimension metrologi system.

I dette PhD studie blev NanoBits – nanostørrelse udskiftelige og adaptive scanning probe tips – udviklet videre til at opfylde kravene til eksisterende AFM anvendelser. To forskellige metoder blev brugt til at fabrikere sådanne NanoBits ved hjælp af lateral nanolitografi; elektronstråle litografi og ionstråle litografi. Ved ionstråle litografi bombarderes en tynd membran med ioner, der skærer NanoBits ud i membranen en for en. Elektronstråle litografi er en langt hurtigere proces, på trods af at den er seriel. NanoBits med tips både til at måle på høj-aspect ratio strukturer samt sidevægge blev fremstillet.

Tip diametre på omkring 30 nm blev rutinemæssigt obnået ved ionstråle litografi (FIB), med den mindste tipdiameter under 15 nm. Længde-bredde forhold på omkring 45 blev opnået med denne teknik. Scanning elektron mikroskop undersøgelser viste at polykrystallinske silicium NanoBits fremstillet med mikrofabrikation potentielt havde tip diametre på 15-30 nm, men som på grund af utilsigtet skrå ætseproces blev gjort væsentligt bredere. Af denne grund blev det undersøgt om spidserne på proberne kunne gøres skarpere ved reaktiv ion ætsning (RIE), ion stråle ætsning (IBE) eller fokuseret ionstråle milling (FIB). RIE og FIB blev vurderet som mest lovende til at opnå dette, mens IBE målingerne ikke gav noget klart resultat.

Ved at designe NanoBits der kan bøje 90 grader ud af planet, opnår man at processen med at opsamle og montere spidserne gøres betydeligt nemmere, idet selvsamme AFM probe hvorpå NanoBits skal sidde, selv direkte kan montere komponenten. To metoder til at udbøje NanoBits membraner blev undersøgt: FIB bestråling og residual stress-drevet bøjning i lagdelte (bimorfe) strukturer bestående af forskellige materialer. Med FIB bestråling, var det muligt at bøje NanoBits i en bestemt vinkel op til 90 grader. Det blev også vist at vinklen kan styres ved at kontrollere ion-bestrålings dosen. Vinkler mellem 25 og 130 grader blev opnået ved hjælp af bimorf stress, som kan fremprovokeres ved at pådampe et tyndt lag metal på den ene side af NanoBits membranen. Yderligere eksperimenter med silicium nitrid substrat og sammenligning med teoretiske modeller blev udført for bedre og forstå mekanismerne bag udbøjningen. Resultaterne indikerede at den væsentligste drivkraft for bimorf udbøjning i dette tilfælde var det intrinsiske stress. Det blev vist at tip vinklen kan finjusteres med termisk aktuation; udbøjning op til 150°C kunne udføres reversibelt, hvilket førte til en ændringer af udbøjningsvinklen i størrelsesorden ±10°. Ved højere temperaturer var udbøjningen irreversibel, der formentlig skyldes omdannelsen af silicid.

NanoBits strukturer blev fabrikeret og monteret på AFM prober i samarbejde med Oldenburg Universitet. Først blev NanoBits samlet op af en mikropincet, anbragt i en dertil fremstillet mikro kasette, og derefter monteret på en AFM probe. Funktionaliteten af disse high-aspect ratio NanoBits blev undersøgt ved at scanne henover optiske gitre med mikroskala dimensioner. NanoBits havde bedre performance end konventionelle pyramidiske prober, og udviste en høj grad af robusthed og slidstyrke; spidsen holdt til mere end 100 scans uden at miste skarpheden. NanoBits tilbyder en stor frihed i forhold til at tilpasse scanning probe teknologi til det store udbud af overflade strukturer og materialer, i kraft af udskiftelighed og fleksibiliten der ligger i den laterale litografiske processering.

Table of Contents

List of Tables

List of Figures

1 Introduction

1.1. Background

Metrology instrumentation finds widespread use covering a broad spectrum of technological fields. Microscopy provides control over the device manufacture and the necessary feedback for improvement. Conspicuously after the advent of transistor in 1950s, driving forces building up ever higher have assisted microscopy to achieve the atomic resolution. Besides allowing a deeper insight into governing physics at the nanoscale, micro/nanometrology can as well be viewed as the prerequisite means for research and industry towards miniaturisation trend. Components with shrinking size tend to deliver higher performance, lower power consumption and lower production costs [1]. The International Technology Roadmap for Semiconductors (ITRS) predicts technological trends of microelectronics and has clearly indicated the continuance of miniaturisation for integrated circuits [2]. Continuously developing fabrication technology and altering device architectures impose prospective metrology demands.

Invention of atomic force microscopy (AFM, or scanning probe microscopy (SPM)) in 1986 [3], following the announcement of scanning tunnelling microscopy (STM) in 1982 [4], recast the surface metrology concept. A range of scanning probe methods have been developed over the years based on different sorts of tip-surface interaction: electrical, optical, thermal, force. Although STM is largely used in surface physics, AFM is rather preferred in industry and applied research areas for measurement purposes [5]. Reproducible, fast fabrication of microcantilevers and probes together with alternative probing modes ease AFM's adaptation to altering technological needs. AFM is a versatile tool: it is capable of topographical imaging, phase imaging, electrostatic force microscopy, magnetic force microscopy, nanoindentation, and nanomanipulation; among these, surface imaging is the most commonly applied technique. Material surfaces ranging from metals to aerogels can be investigated under ambient conditions with AFM, and today, live matter can be *in vivo* imaged [6].

Despite its advantages such as non-destructive imaging and atomic resolution, AFM needs to constantly adapt to the ever-altering device architecture and perpetual size shrinkage. SPM was initially targeted for imaging of flat surfaces, but over time, specific applications called for enhancements to address specific needs, like specialised probes. For instance, while photonic crystals and nanooptical devices place significance on information about line-edge roughness (LER, or sidewall profile), linewidth roughness (LWR), and via/trench depths [8], 3D integrated circuit designs are in need of undercut, indentation imaging

[9]. That is, device miniaturisation requires the scanning probes to adapt into finer geometries to provide higher lateral resolution. To meet these needs, in addition to contact, tapping, non-contact modes, two more modes have been developed for AFM: CD-AFM and DT-AFM. CD-AFM concerns imaging of the challenging architectures with undercuts and roughness while DT-AFM takes on high-aspect ratio designs.

1.2. State-of-the-art

Deep trench and critical dimensions applications

Deep trench (DT) (or high-aspect ratio (HAR)) and critical dimension (CD) AFM are largely used by the research and development (R&D) departments of the semiconductor industry in order to monitor and analyse the processing steps of morphologically challenging structures. These techniques are also advantageous on the grounds of providing non-destructive and traceable calibration for the similar CD metrology tools [7-8], such as critical dimension scanning electron microscopy (CD-SEM) and optical scatterometry [9]. The semiconductor and data storage industries, related R&D companies and tool manufacturers are thus the major users. The latest ITRS roadmap defines the technology nodes as 26 nm (for dynamic random-access memory (DRAM) ½ pitch) and 17 nm (Flash ½ pitch) for 2014 [10].

HAR probe applications: The smallest and most demanding structures are contact holes in DRAM (hole diameter ≤50 nm, aspect ratio (AR) > 20), and flash memory technologies (hole diameter ∼36 nm, AR > 15) [10].

CD probe applications: Measurement of the critical dimensions is accomplished done either by lateral or torsional oscillation of the AFM probes, or by using tips with an overhanging feature. The effective dimensions of sidewall features (e.g. line-edge roughness (LER), linewidth roughness (LWR), top/bottom CD) show variations in the range of 50–200 nm (width) and 30–500 nm (height) [10].

Current and future DT- (HAR) and CD-AFM probes

1) Current HAR probes: HAR probe tips are fabricated by
    - Focussed ion beam (FIB) milling (Figure 1(a)),
    - reactive ion etching (RIE) (Figure 1(b)), or
    - electron beam-induced deposition (EBID) of carbon (Figure 1(c)).

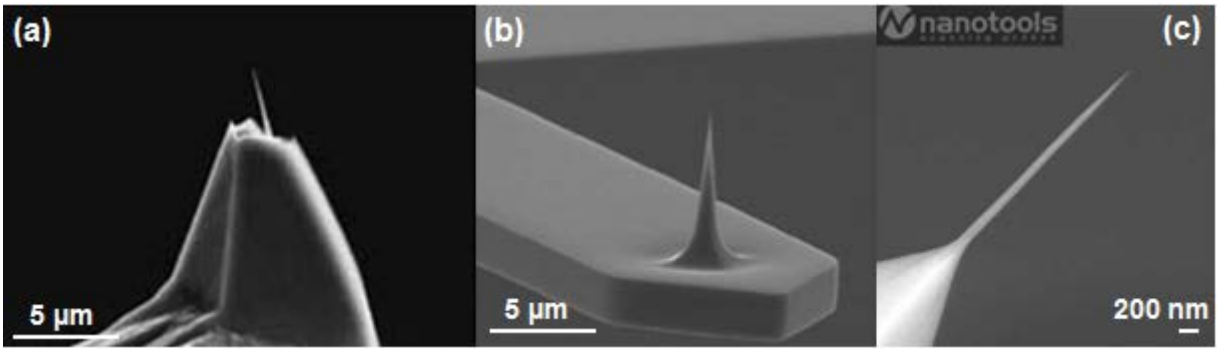

Figure 1 HAR probes fabricated by (a) FIB milling [11], (b) RIE [12], and (c) EBID of carbon [13].

Typical dimensions of HAR probes for deep trenches-vias and shallow trenches are listed in Table 1.

Table 1 HAR tips features for deep and shallow trench applications [11-13].

	HAR probes for DT and vias (Depth: 1–2 µm, width: 100–500 nm)	**HAR probes for shallow trenches (Depth: 200–500 nm, width: 50–70 nm)**
Length	1–5 µm	<1 µm
Diameter	≥20	≥20
Aspect ratio	50–250 nm	30–40 nm
Tilt accuracy	±0.5°	±0.5°

2) Current CD probes: CD probes are fabricated by
   - (i) Reactive ion etching and (ii) sharpening of silicon probes,
   - Deposition of a hard mask (silicon nitride, Si_xN_y) and underetching of the silicon substrate underneath (see Figure 2(a-b)), and
   - EBID of carbon (see Figure 2(c)).

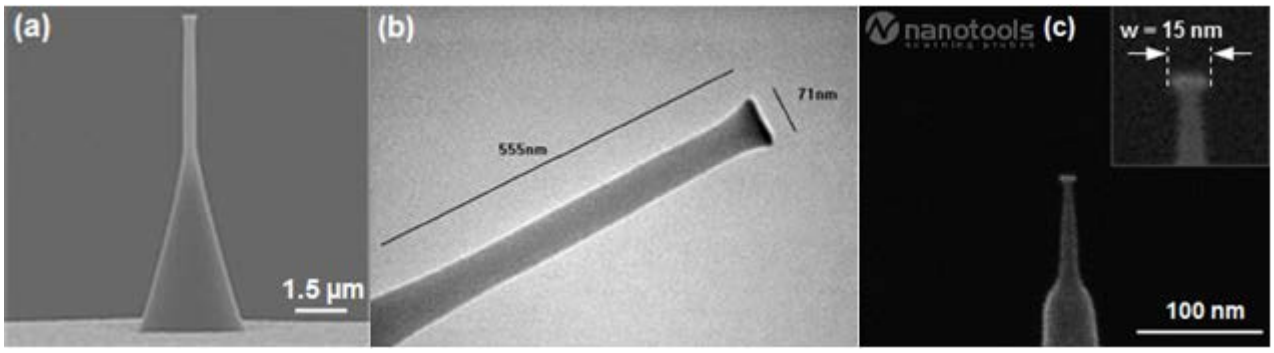

Figure 2 CD probes (a) fabricated by RIE [12], (b) with Si_xN_y cap [14], and (c) fabricated by EBID of carbon [13].

The typical CD probe dimensions are listed in Table 2. Figure 3 the sketch of a CD probe with the related terms.

Table 2 Dimensions of CD probes.

CD probe	Dimension [nm]
Effective length	100–5000
Tip width	32–850
Overhang	3–100
Vertical edge height	5–20

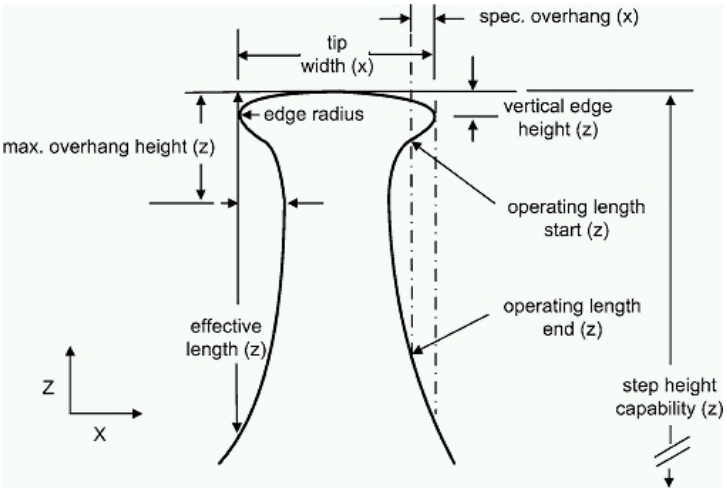

Figure 3 Definition of CD probes properties [15].

3) Future HAR and CD probes: In the start of the project in 2010, ITRS roadmap had anticipated the technology nodes to shrink form 45 nm to 28 nm (for DRAM ½ pitch) and from 32 nm to 20 nm (for Flash ½ pitch) for 2014 [16]. Table 3 lists the required dimensions for HAR- and CD-AFM probes in accordance with this estimation.

Table 3 Anticipated dimensions of future HAR and CD probes.

Dimension	HAR probes	CD probes
Length	300–500 nm	-
Diameter	≤20 nm	15 nm
Aspect ratio	≥25	-
Overhang	-	5 nm
Vertical edge height	-	≤0 nm

1.3. Problem formulation

The growingly demanding technological applications require the utilisation of advanced, special AFM tips for CD-AFM and DT-AFM: high-aspect ratio tips for DT-AFM and critical dimension tips for CD-AFM [9-12]. These advanced tip types, however, are fabricated by vertical means of fabrication: FIB milling and RIE.

Together with EBID, vertical fabrication provides low throughput and therefore are costly and batch-incompatible.

Another drawback is the wear problem of the silicon tips. Silicon tips scanning poly-silicon lines were observed to lose their sharpness by 0.12 nm per site (each site consists of 32 lines with 1 µm length) [9]. This means that after 100 scans, tip diameter already becomes >15 nm, which is not appropriate for challenging structures and needs replacing.

Both changing of the sample (topography) and the blunting of the tips require replacement of the AFM tip with a newer, sharper or application-specific one. That is, tip/probe exchange is a frequent action for the AFM operators. Beside possible variations in the imaging conditions, changing of the tip costs the operator a considerable time.

1.4. Approach

AFM can benefit from availability of adequate, surface-specific tips (HAR, CD, undercut, and many more). AFM probes available for *in situ* replacement could greatly increase the efficiency and adaptability of a CD system. In this thesis, a credible approach to tackle the abovementioned issues is discussed: NanoBits. The term NanoBits denotes nano-sized customisable and exchangeable scanning probe tips. NanoBits can be attached to standard AFM cantilevers, which would allow adapting of the scanning tips in various sizes and shapes to the application-specific topography. The replaceable AFM tips defined by lateral nanolithography could allow imaging of 3D HAR and CD features. With a miniaturised nanorobotic system, micro-/nanointegration of such tips into an AFM stage can be achieved, which would realise a library of exchangeable tips. Development of novel scanning modes could then allow taking full advantage of the fabricated NanoBits.

This thesis discusses lateral nanolithography of the NanoBits by focused ion beam milling of the blank freestanding NEMbranes (NanoElectroMechanicalSystems Membranes) and by electron beam lithography (EBL)-assisted nanofabrication. FIB milling allows and was mainly used for realisation of prototypical NanoBits thanks to its short turn-around time. Nanofabrication, on the other hand, is batch-compatible and can provide identical devices in great numbers. A main goal pursued in this work is the fabrication of customisable AFM tips whose performance is comparable to their commercial counterparts. Then, to enable quick assembly and usage of the NanoBits, and thereby minimise the time loss during tip-exchange, the methods to manipulate NanoBits out of their as-fabricated in-plane were investigated.

NanoBits is an FP7 EU project and a collaborative effort of a number of partners. During the course of this work, close collaboration was pursued with the following partners, and were mentioned where appropriate:

(1) NanoWorld (Erlangen, Germany) is a leading AFM probe company. NanoWorld supplied the AFM cantilevers and made invaluable contributions in terms of 3D-AFM requirements.
(2) OFFIS (Carl von Ossietzky University of Oldenburg, Germany) was responsible for nanorobotic assembly of the NanoBits as well as development of new AFM scanning modes. OFFIS was frequently contacted especially about the design of the NanoBits, and collaborative assembly experiments were performed periodically to test the fabricated NanoBits.

(3) IOF Fraunhofer (Jena, Germany) provided the topographically challenging optical samples for DT and CD measurements.

1.5. Overview of chapters

In Chapter 1, a brief historical background of atomic force microscopy was presented. Critical dimension- and deep trench-AFM were introduced with the state-of-the-art tips used today. Problems encountered with the fabrication and replacement of the tips was formulated and motivation for the PhD thesis was established.

Chapter 2 describes the design of the NanoBits considering the possible manipulation scenarios, lays down the requirements set by applications and fabrication, and finally presents the actual NanoBit structure.

Chapter 3 describes the methods used to fabricate the NanoBits: FIB milling and EBL-assisted nanofabrication, including the theory behind these fabrication tools. The end-products are presented.

Chapter 4 concerns the characterisation of the critical parameters of the NanoBits, describes the metrology and methodology used, compares FIB-milled NanoBits to the EBL-defined NanoBits, and eventually lists the post-processing methods that can be used to sharpen the NanoBits.

In Chapter 5, out-of-plane bending of NanoBits by inducing stress through FIB irradiation and metal deposition is described. Controlling and reproducibility of these mechanisms are discussed, and finally, thermal actuation of freestanding structures as a way of fine-tuning of the bending angle is presented.

Chapter 6 introduces the nanorobotic system used in manipulation experiments, elaborates on the procedure followed, and discusses the improvements implemented both the assembly and automation process. The chapter is finalised with demonstration and discussion of the scanning performance of NanoBits.

Chapter 7 provides a general look to the work done during the PhD study, summarises the results and comments on the possible prospective improvements that can be integrated to the manufacturing and manipulation of the NanoBits or similar customisable probe tips.

2 Design

In this chapter, design considerations of the NanoBits are discussed. The requirements and specifications set by manipulation (assembly and usage) scenarios, diversity of applications, performance concerns and microfabrication standards are taken into account. The actual design abiding by the given specifications is presented at the end of the chapter.

2.1. Manipulation scenarios

A manipulation scenario is defined as the combination of assembly and usage scenarios. An assembly scenario describes:

- Orientation and position of reservoir, gripper and target
- Type of reservoir, reservoir layout, tip layout, tip orientation and position:
    - Handling strategy: the transfer of the NanoBits to the AFM probe might be through 2 steps (gripper not used) or 3 steps (gripper used). These will be described below. Moreover, the angle of which the gripper approaches the NanoBits and the AFM probe makes a considerable difference.
    - Gripper vs. Handle (for 3-step handling): this concerns the design and interaction between the handle and the manipulation tool in the case of a 3-step tool-based transfer process.
    - Connector vs. Plug + attachment strategy: this concerns both the design of the connector (on the NanoBit) and the plug (target site on the AFM tip), and additionally, the method used to fasten the NanoBits to the AFM probe, e.g. through an adhesive material, deposition of encapsulating material on the junction, mechanical force, or simply through friction.

A usage scenario extends this to describe the orientation of tip against the surface, scanning mode and the expected output, which are discussed in Section 2.1.2.

2.1.1. Assembly scenarios

There are several terms and expressions, to which special meanings are attributed in the context of manipulation scenarios. These are listed and described in Table 4.

Table 4 The terms used in the manipulation scenarios with their descriptions.

Term	Description
Connector and plug (NanoBits)	The "connector" is the part of the NanoBit which is made to fit into the equivalent part of the AFM probe, termed the "plug".
(Micro)gripper/(micro)tweezer	Manipulation tool for detaching the NanoBit**,** and transporting it between reservoir, cartridge and the AFM probe.
Breakpoint (NanoBits)	The breakpoint is the mechanically weak point where the NanoBit is attached to the reservoir. This part is deliberately made thin in order to make the NanoBit break off in a controlled way.
Reservoir	Library of NanoBits fabricated on a chip, defined either by electron beam lithography or by focused ion beam milling.
Cartridge	Intermediate reservoir, where the NanoBits can be stored, preferably in an easily accessible way, so that they can be picked up later either by an AFM probe or by a microgripper.
Assembly scenario	Collective description of orientation and position of reservoir, gripper, cartridge and target AFM probe, as well as procedure for transferring the NanoBit from reservoir to a correct position in the AFM probe.

2.1.1.1. Microgripper approach

A. Inside reservoir: 3-step assembly (detach-move-place)

In the work leading to the EU project NanoBits, so-called "inside reservoir" had been realised [17]. In these reservoirs, the NanoBits are defined as suspended structures made by electron beam lithography, however, do not extend over an edge. They are thereby accessible only by using grippers, and only when approached from certain angles, roughly covering one quarter of a full unit sphere. The NanoBits are "inside" the wafer, as opposed to extending from an edge. The fabrication method can be very simple and give high quality results, and it is possible to pack tens of thousands of NanoBits on a 4" silicon wafer, with the limitation of available electron beam writing speed. Even with the state-of-art semi-commercial electron beam lithography systems, covering a major part of a silicon wafer with features on a scale relevant for SPM is, as a rule, extremely costly, so unless a cheaper method such as nanoimprint lithography is used, the advantage of the potentially large numbers on a single wafer is limited. In practice, even just hundreds of NanoBits with different shapes should be sufficient for most applications.

In terms of assembly, an issue with this scenario is the necessity of using a gripper. Although gripper-based assembly of NanoBits has been shown to be straightforward [17] – given that one has access to complex and advanced robotics system inside SEM – it is suggested that the intermediate manipulation using a gripper should be avoided to simplify the assembly process. It was found that the gripper should be nearly perpendicular to the surface for the process to work, as shown in Figure 4.

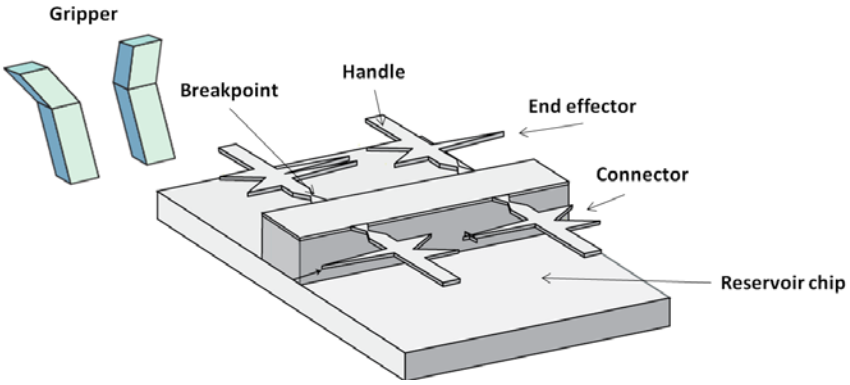

Figure 4 Inside reservoir: scenario for indirect picking using gripper. [Image reproduced with permission from Peter Bøggild.]

The process is then (1) identification of NanoBit using image recognition or by its known position on the wafer (e.g. by using alignment marks); (2) alignment of manipulation tool to the NanoBit; (3) actuation of gripper and detachment of the NanoBit; (4) removal of NanoBit reservoir and approach of the AFM probe while the NanoBit is being held in the gripper jaws; and eventually, (5) attachment of NanoBit to the AFM probe.

The microfabricated grippers/tweezers are highly capable tools in manipulating micro- and nanosized objects. Several microgripper applications and designs were introduced up to date, including micro electro discharge machined (μ-EDM) grippers [18], grippers made by bonding two microchips that have a bimorph cantilever and a piezoresistive sensor cantilever [19], electrostatic grippers [20-21], electrothermal (e.g. Guckel type [22], three-beam [23], ribcage [24]) grippers, and grippers that incorporated carbon nanotubes [25-26]. In this work the ribcage electrothermal microgrippers fabricated at DTU were used for handling NanoBits. One end-effector of the gripper is fixated to the carrier chip whereas the other end-effector is the extension of the ribcage body and connected to the fixated part. When a potential is applied to the ribcage body, the central beam of the body elongates due to Joule heating in the forward direction; the connection to the fixated part diverts the movement to the sideways and thereby allows closing onto the stable end-effector [24].

An alternative to avoid the gripper is shown in Figure 5. Here a so-called AdvancedTEC [27], a protrusive and “supersharp tip” from NanoWorld is FIB-milled into a form that may directly pick up the NanoBits. In this case, the design of the NanoBits should be different: the tip should not be pointing sideways, but rather the surface to be scanned; the structures had better be defined on the so-called NEMbranes (nanoelectromechanical system (NEMS) membranes, indicating the concept of template chips that can be adapted to a number of different NEMS applications through FIB milling) for flexibility concerns. Such an approach can be difficult to carry out in practice due to limitations in aligning the probe to the NanoBits, especially in *z*-direction, in the absence of an optical marker.

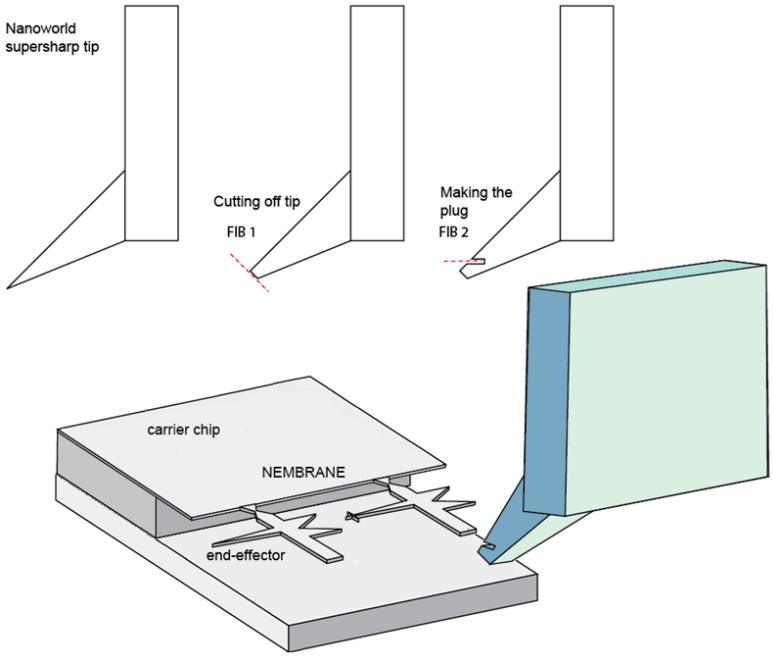

Figure 5 Inside reservoir for direct picking using AFM probe. [Image reproduced with permission from Peter Bøggild.]

B. Edge-/inside-reservoir with intermediate cartridge: 3-step assembly (detach-place-pickup)

A flexible approach for direct assembly from an edge reservoir could be the pre-mounting of NanoBits on a *cartridge,* which is designed for maximal accessibility, and thus, does not impose any constraints inherited from the silicon chip fabrication process such as a particular orientation resulting from planar lithography or a bulky chip. The cartridge, for instance, could be a freestanding membrane, and NanoBits can be fixated on the membrane edges by electron beam-induced deposition, which would allow very fast mounting. Perpendicular positioning of the cartridge/NanoBits to the target surface can additionally reduce the time spent during mounting to the AFM probe.

A more suitable and more advanced type of cartridge can feature holes opened by FIB milling, ion beam etching (IBE) or reactive ion etching (RIE). The NanoBits collected from the source reservoir can be inserted in these holes perpendicularly, and later be assembled directly by the AFM probe. Perpendicular orientation and an ordered library of NanoBits (types) should make the picking up particularly easy. Furthermore, such a cartridge would immediately allow exchanging the used (damaged, broken, worn) tip with a newer one, or even with one that is matching better the area to be imaged.

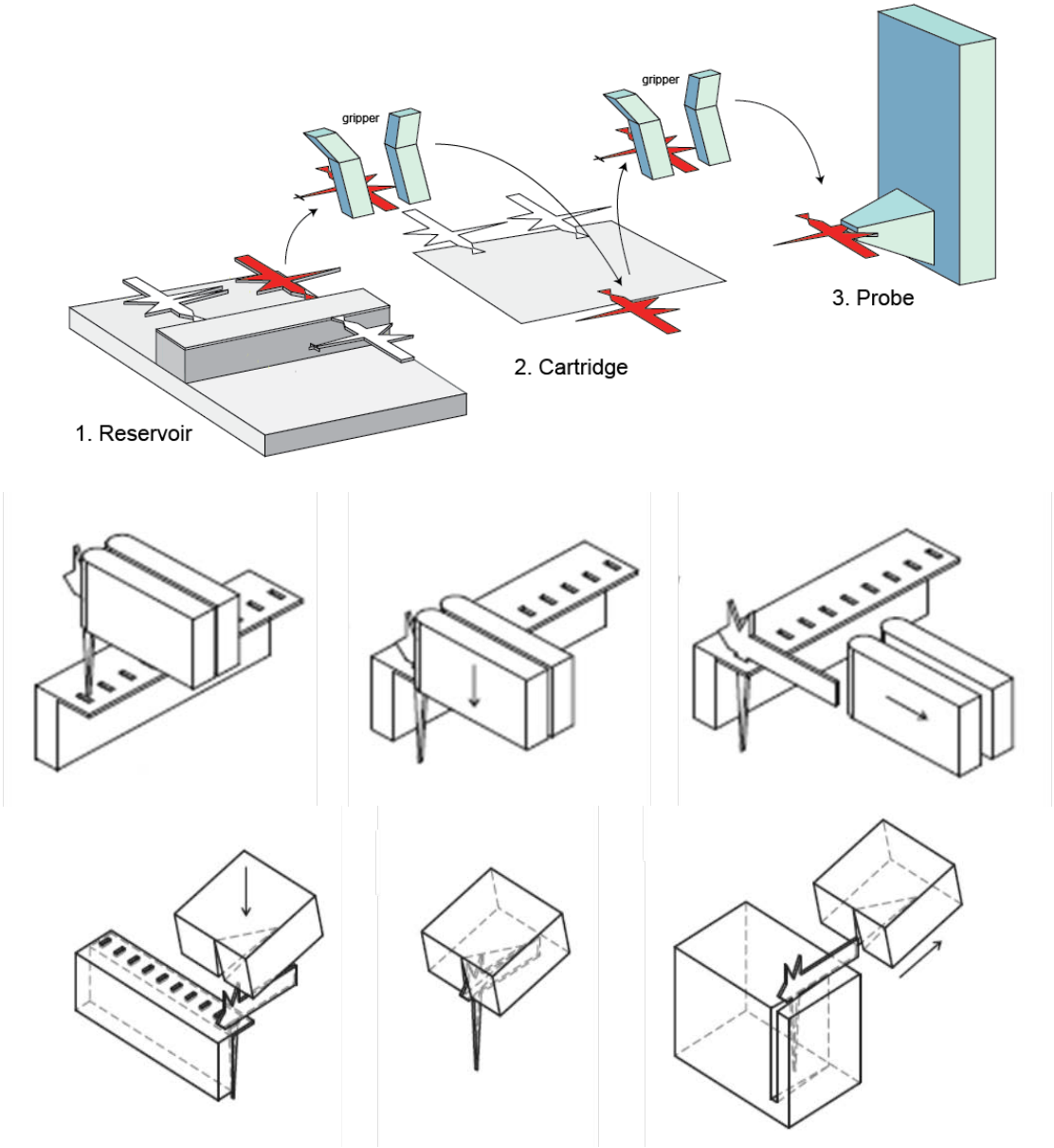

Figure 6 Illustration of cartridge concept, where (top) a gripper is used to mount the NanoBit on a membrane cartridge and then to insert into the plug, or (middle) NanoBits can be stored in the cavities opened in the freestanding membrane, and (bottom) can later be picked by the AFM probe, used, and eventually released to accommodate a newer tip, perhaps one that better suiting the scan area [28].

Advanced gripping schemes – rotating NanoBits for fast cartridge exchange:

The concept of a cartridge with cavities appears as a promising option especially on the grounds of identical and vertical alignment of the NanoBits, which ensures direct insertion to the plug and AFM probe becomes ready for scanning. In this case, a NanoBit should be rotated from their as-fabricated in-plane orientation to out-of-plane (downwards). Two possible methods are:

(1) The microgripper end-effectors (jaws) can be shaped by FIB milling, RIE or IBE to possess non-vertical sidewalls, which while gripping would induce a torque on the NanoBit and thereby turn it in between the end-effectors.
(2) Mounting of either the microgripper or the reservoir at a small tilted angle, essentially provoking the same effect and outcome.

Both methods are shown in Figure 7.

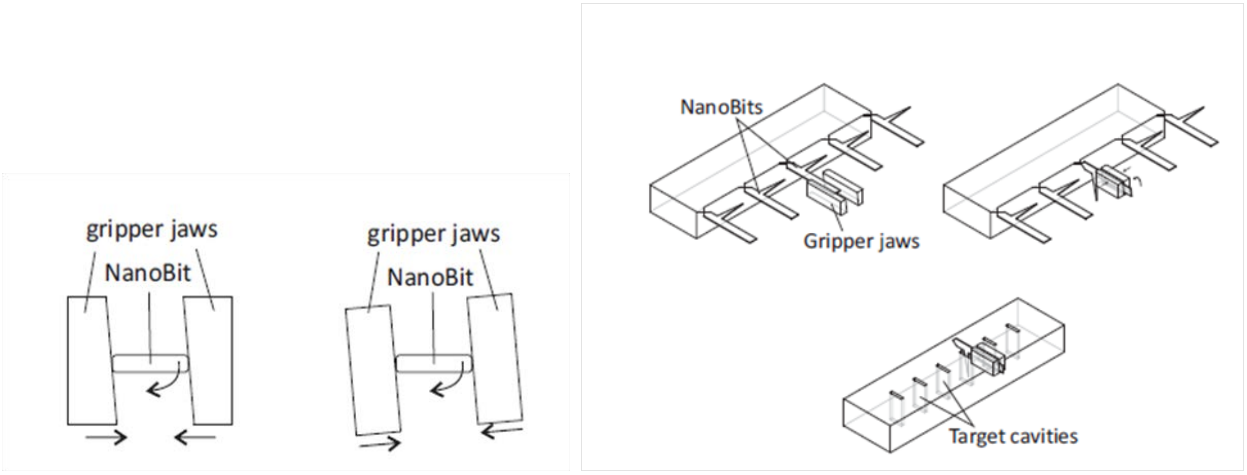

Figure 7 (left) The effect of rotation is achieved by cutting the gripper using focused ion beam milling in order to form asymmetric jaws or by rotating the gripper slightly, in both cases generating a torque on the NanoBits. (right) Illustration of NanoBits being turned during the gripping process [28].

2.1.1.2. Out-of-plane-bent NanoBits approach

A. Inside reservoir: 1-step assembly (detach)

Attachment of NanoBit onto AFM probe tip is one of the most important and challenging tasks. Alignment of upward-bent NanoBits can make assembly procedure easier and more convenient for automation. That is, instead of using a microgripper and cartridge as intermediary tools for NanoBit's transfer, one can rather benefit from direct insertion of NanoBit into a slit opened on a plateau-cantilever surface. Such an approach would enhance the accessibility also, as the NanoBits are bent out of their as-fabricated lateral plane. The bent NanoBit (i) can either be aligned perpendicular to the surface so that it can be grabbed by AFM probe approaching from above, or (ii) can stand in an angled position allowing an AFM probe with a specially shaped side-slit to lock in with the NanoBit whilst scanning surface. The latter option is considerably more convenient since resulted angle of bending can vary to some extent due to reproducibility issues during fabrication process; these deviations, nonetheless, may be rendered insignificant for the assembly operation because side-slit approach would allow fastening of NanoBits having a certain angle window (e.g. 30-60°).

There are few possibilities in the literature that could be used for bending of the NanoBits, such as capillary forces- [29] or residual stress-driven bending [30]. Regarding the NanoBit structures and that they will likely be positioned at the edge of a freestanding membrane, two suitable methods can be used:

I. *Bending by stress built-up in bilayer structures*: in-plane NanoBits/NEMbranes can be deposited with stressful metal layers. Since the evaporated metal films generally have tensile stress [31],

upon relaxation of this stress, the bilayer membrane will curl upwards, deflecting the NanoBits out of their lateral plane. If the substrate material or the deposition chamber heats up during the process, cooling of the structure to room temperature will also contribute to bending, because metals have higher thermal expansion coefficients than the semiconductors or insulators, allowing them to shrink more when cooled.

II. *Bending by FIB irradiation*: NanoBits/NEMbranes can be subjected to FIB irradiation, for instance at their bases, and be bent out-of-plane as the stress in the exposed area will alter as a consequence of Ga contamination and material ablation. Although this approach may not be feasible on a large scale, it stands as an option for obtaining early examples of such tips, allowing feasibility investigation of the concept.

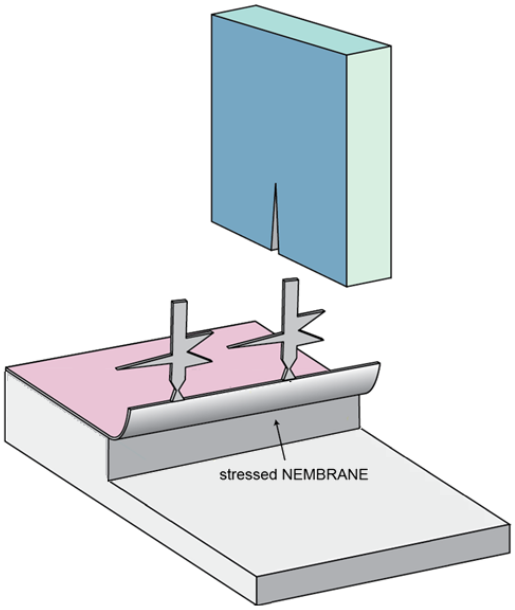

Figure 8 . Concept sketch for picking up of out-of-plane-bent NanoBits from an edge directly with an AFM probe with a FIB-milled plug. [Image reproduced with permission from Peter Bøggild.]

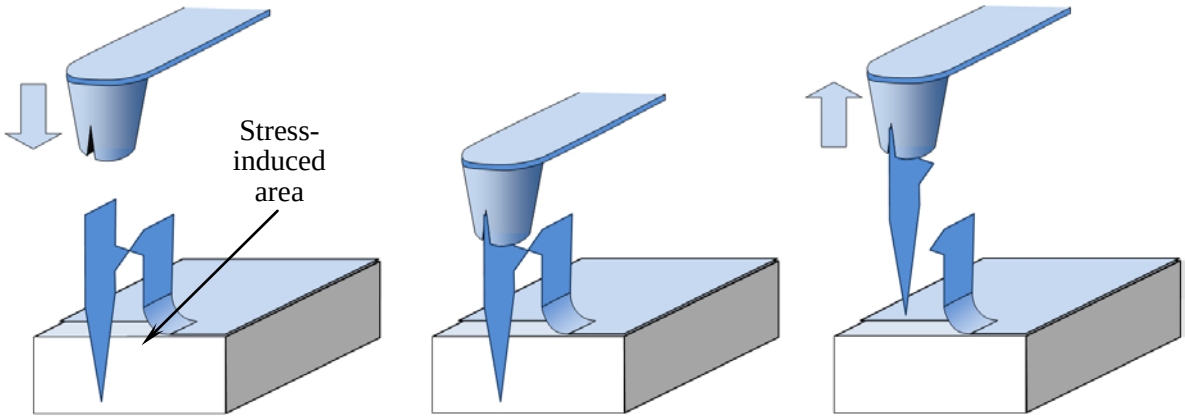

Figure 9 (From left to right) manipulation sequence showing an AFM probe with a slit opened on plateau surface approaching from top towards the NanoBit standing at right angle, locking in with NanoBit, and parting with NanoBit having detached the tip from the break-point [32].

Insertion of the OOP-bent NanoBits is not necessarily as easy to implement as Figure 9 suggests; however, when optimised, it should present a significant simplification of the procedure, in which ready-made NanoBits can immediately be inserted into the workstation for *in situ* exchangeability of the NanoBits. This requires a consistent design of the AFM probe, the reservoir and the NanoBits, yet, also is likely to possess the greatest commercial/practical perspective in the future.

At this point, the focus has not been on the detailed shape of the NanoBits or the connector itself, as this is clearly a function of the chosen scenario. The scenarios differ greatly in complexity, orientation and space requirements, requirements on shape of AFM probe, and type of 3D-AFM probe that is the result of the assembly process. Since it is not possible to devise a generic 3D-AFM probe that is suitable for imaging all types of target structures, which is in part the motivation for the exchangeability and flexibility concept of the NanoBits project, it is possible that more than one of these strategies may be pursued.

2.1.2.Usage scenarios

In determining the usage scenarios, the input and feedback from end-users and commercial tip companies were important to ensure the relevance of the approach and solutions. In this regard, the recommendations and guidance of NanoWorld as an SPM tip manufacturer and a Nanobits project partner were greatly appreciated.

Requirements for the mounting of the NanoBit: Ordinary pyramidal tips of AFM probes can lead to a misorientation of the NanoBit. Therefore, a plateau tip is preferential. In this case a slit opened by FIB milling in the plateau tip can serve as the connector platform, into which insertion of the NanoBit should be achieved by closure-based means rather than gluing with electron beam-induced deposition, in order not to hinder removal of a used NanoBit. An optical marker indicating the slit position on the AFM cantilever back may be necessary for precise alignment of the probe to the NanoBits to be picked up.

Cantilever requirements for the 3D-AFM scanning method: detection of torsional deflection of the cantilever. A torsional sensitivity in the same order of magnitude as the lateral sensitivity is likely to be needed since the cantilever has to be soft and will be operated in contact mode.

NanoWorld's proposal for the 3D-AFM probe tip: Use of a plateau tip instead of a pyramidal tip for easier and more precise mounting of the NanoBit. Slit manufacturing can be done most easily by FIB milling. If no reliable microfabrication-based method can be found for the optical marker, it can as well be made by FIB milling. The cantilever needs to be very soft: maximum torsional deflection sensitivity with simultaneous suppression of lateral movements can be achieved via a triangular AFM cantilever.

The design specifications of the 3D-AFM probe extracted from finite element analysis follow:

- Tip/connector platform: plateau tip, silicon, 10 µm tip height, 5–10 µm plateau diameter.
- Cantilever: triangular shape, ~0.1–0.2 N/m lateral stiffness, torsional and lateral sensitivity in the same order of magnitude, silicon or silicon nitride.
- Other properties: back-side metal coating to enhance the laser reflection, front-side metal coating to prevent charging (if needed).

2.2. Requirements and considerations

For the given manipulation scenarios, geometrical and structural features of the NanoBits need to be defined in association with certain requirements. These requirements are considered under four categories: application, simplicity, reliability and customisability.

Relevance for applications

Typical examples of challenging topographies for NanoBits are deep trenches/vias (e.g. photonic crystals, base-substrate for suspended structures such as graphene) and structures with rough sidewalls (e.g. finFETs, optical gratings). Figure 10 shows a perforated SiO_2 layer fabricated with the intention of serving as a base-substrate for suspended graphene, representing a demanding research application. The holes have an average diameter of 25 nm, and a depth of ~30 nm, which is not far from the dimensions of modern day integrated circuits. Scanning such a surface requires a super-sharp tip [11, 13] to be able to reach trench/via bottom. Specific to the topography shown in Figure 10, the scanning probe should have a diameter of <20 nm at >30 nm height. In Figure 11 an SEM image of an optical grating received from IOF Fraunhofer is displayed. In the magnified image, lines are seen to have down to 66 nm width, with line width roughness exceeding 10 nm. For this specific example, scanning tip needs to have a different shape in order to probe the sidewalls: tips with overhanging and flared tips [12-14] are among possible candidates.

Since vias, feedthroughs and optical gratings can be micron-deep, NanoBits are required to span a substantial length range, i.e. from hundreds of nanometers to several microns, without becoming too broad to enter narrow, constricted areas. Although it is difficult to give a number for the aspect ratio (length divided by width), one should expect to achieve lengths up to 5 µm, with aspect ratios in the order of ≥10.

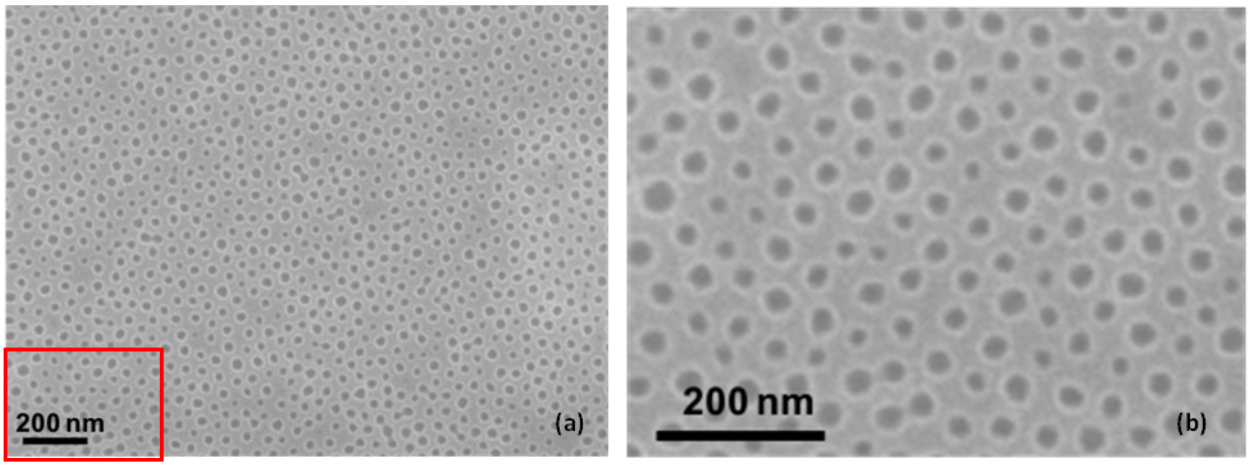

Figure 10 (a) SEM micrograph of perforated SiO_2 prepared for partially suspended graphene; (b) magnified image of red rectangle in (a). Holes have an average diameter of 25 nm and a depth of 30 nm.

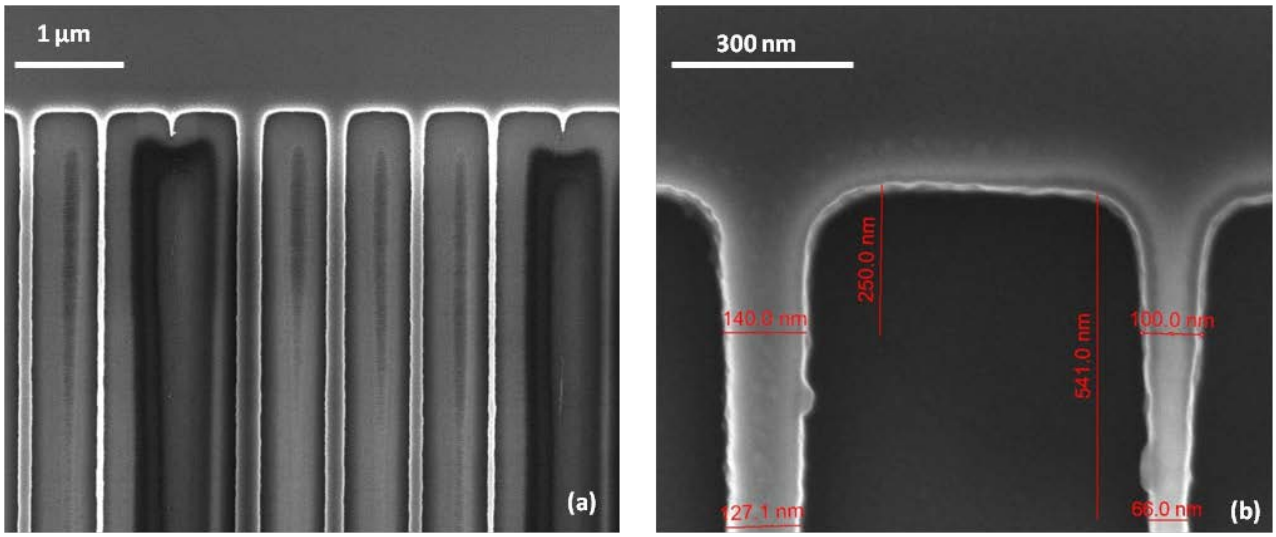

Figure 11 (a) SEM image of an optical grating with 0.5 µm pitch; (b) magnified image of (a): line widths narrow down to 66 nm, with line width roughness around 10 nm.

Simple, cheap processes

"Simplicity" in this context denotes the qualitative measure of how many steps, and in particular critical or difficult steps, there are in the NanoBits production line and nanorobotic manipulation sequence. By pursuing straightforward process flow with standardised steps, the NanoBits could be fabricated in any cleanroom facility more cheaply and reproducibly. To achieve this:

- Prioritisation of standard micro-processing tools and techniques in the process flow should be pursued; and,

- Fabrication should favour avoiding steps/tweaks that call for certain expertise, technical skills, or highly specialised or expensive equipment. (As will be seen in the following, the choice of electron-beam lithography makes this criterion difficult to follow.)

Such a process flow should allow one to produce the targeted NanoBit structures by following the fabrication sequence. In terms of manipulation, NanoBits need to be easily accessible, easy to pick-up, and controllable.

- Accessibility: microfabrication produces in-plane structures. Unless they are bent out of their plane, accessibility can be achieved through creating freestanding devices. This is possible via (i) underetching of structures, (ii) defining them at the edge of a chip, and thus making them nearly 360° accessible.

- Pick-up: possible difficulties during picking up of NanoBit can be alleviated by optimising the NanoBit connector. Too narrow connectors may result in unstable or even loss of NanoBits during fabrication and/or manipulation whereas too wide connectors may render NanoBits hard to detach from the source.

- Control: NanoBits should not display any undesired or unforeseen behaviours during manipulation: structural integrity of the NanoBit should be ensured concerning material rigidity, durability and thickness.

Reliability

- Material: widely accessible materials with well-known properties (hardness, flexibility, durability) should be preferred; e.g. silicon (Si), polysilicon (pSi), (stoichiometric/silicon-rich) silicon nitride (Si_3N_4/Si_xN_y, respectively). Besides their properties, scan adaptabilities and scan qualities of these materials are known commonly as well. Table 5 lists the compatibility between various probe and sample materials [8].

Table 5 Compatibilities of various sample and probe materials [8].

Sample / Probe	Resist	Silicon	Poly-Si	Dielectric
Silicon	Excellent	Good	Fair	Poor
SiN-cap	Excellent	Excellent	Excellent	Good
SiN coating	Excellent	Excellent	Good	Fair
Carbon coating or CNT	Poor	Excellent	Excellent	Excellent

Excellent: >1000 sites*
Good: 200-1000 sites
Fair: 50-200 sites
Poor: <50 sites or un-scanable
*Tip lifetime is application-dependent, numbers here are typical values

- Shape: NanoBit geometry and size should be defined in accordance with the topographies to be probed (cf. “Relevance for applications”). In the batch-fabricated samples, exotic dimensions and features need not be prioritised, as special, customised tips can readily be created on a one-by-one basis using FIB milling of membranes or of hybrid NanoBits (partly shaped NanoBits, which only need final specification by FIB milling).

Customizability

Using the electron beam writer is very convenient and fast, provided the cleanroom has access to one. JEOL JBX9500FSZ used in this work fulfills the simultaneous requirements of high quality, wafer scale exposure and throughput, owing to its Schottky filament with high brightness, 100 keV accelerating voltage, and very fast (up to 100 MHz) electronics (see section 3.2). Since this is not necessarily the case, and to combine the advantages of high throughput (EBL) and high customizability (FIB), we have incorporated both non-patterned membranes, which can be shaped freely into any shape, and “rough” NanoBits, which have a

generic shape defined by EBL and can then be finalised with respect to sharpness and end-effectors using FIB – with a great reduction of fabrication time as a consequence, since the slower FIB milling process is only used minimally for the final shaping.

2.4. Actual design

Final design is shaped by the criteria set by assembly and usage scenarios, specific surface profiles (applications), pursuit of simplicity (during fabrication and manipulation) and reliability/predictability concerns.

Geometry

The NanoBit shape with featured elements and dimensions is presented in Figure 12.

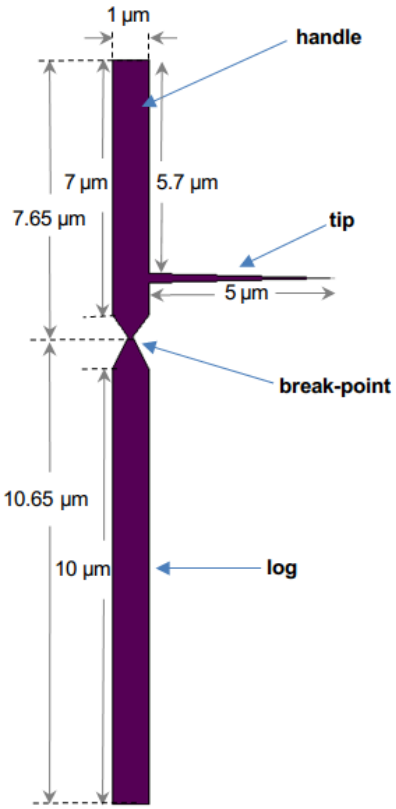

Figure 12 NanoBit design with structural elements pointed by blue arrows: handle, tip, break-point, log. Dimensions of the respective segments are illustrated.

Handle: The handle has straight edges to ensure safe insertion into the plug (FIB-milled slit on the plateau AFM probe). The handle has a 7 µm length, an additional 0.65 µm until the break-point, and 1 µm width to provide a reliable mechanical fastening into the slit. To give the electrothermal microgripper sufficient space for picking up and manipulating the NanoBit, the tip is located 5.7 µm away from handle end.

Break-point: The NanoBit is intended to be detached at this very point. Information on the optimal working width was collected from previous experiments by Rajendra Kumar [17] and prototypical FIB-milled NanoBits: 150 nm. Break-point is 1.5 µm away from the tip to avoid damaging the tip while manipulation.

Log: This long section is the element that will connect the NanoBit body to the chip body. Log is designed long (10 µm) to minimise the risk of misalignment during EBL-PL mix-and-matching.

Tip: The tip displayed in Figure 12 is a HAR tip. Its length is 5 µm, base width is 0.25 µm; i.e. aspect ratio: 20. Different tip types have different lengths, but the base width of all NanoBit types is constant. Alternate tip features are detailed in the following section.

End-effector

Based on the topography types that call for DT-AFM and CD-AFM, 3 types of end-effectors have been implemented to NanoBits: tapered (HAR tip), deflected (side-tip) and cross. These are shown in Figure 13.

Tapered (HAR tip): the end-effector narrows down to 2 nm in order to attain smallest tip feature size possible (see Figure 13(b)). HAR tips have 5 µm length and 250 nm base width, and aim to scan surfaces that have challenging features in *z*-direction.

Deflected (side-tip): The end-effectors of side-tips are deflected by 45° to probe sidewalls of protruding structures. Tilted part extends both to side and farther by 400 nm. The neck, where deflection starts, has a 1 µm width (see Figure 13(c)), which should ensure the integrity of the tip. Total tip length is 4.4 µm.

Cross: Cross end-effectors (or cross-tips) are a variation to tapered end-effectors with 3 small kinks extending ahead and to sides. At cross midpoint, where all the smaller kinks meet, tip breadth is 150 nm. Each kink is 1-µm- and tip is 7-µm-long. Shape and dimensions are exhibited in Figure 13(d).

HYBRID/CUSTOMISABLE STRUCTURES

A 4" wafer can facilitate 330 NanoBit microchips that are comparable to a commercial AFM probe chip in size. Two-third of these chips has been reserved for NanoBits. On half of the remaining chips (∼50 pc.), hybrid structures were implemented. A hybrid structure has a *rough* shape of a NanoBit (see Figure 14). The name *hybrid* is adopted since these patterns are intended to be finalised through a hybrid of processing: microfabrication and then FIB milling. This approach is anticipated to not only give room for flexibility but also to help saving a considerable time, because these structures can later be (i) sculpted and (ii) sharpened by FIB milling without having to mill/define the whole NanoBit pattern. Two types of hybrid structures differ in their tip width only: 1 µm and 1.5 µm. Tip length: 10 µm.

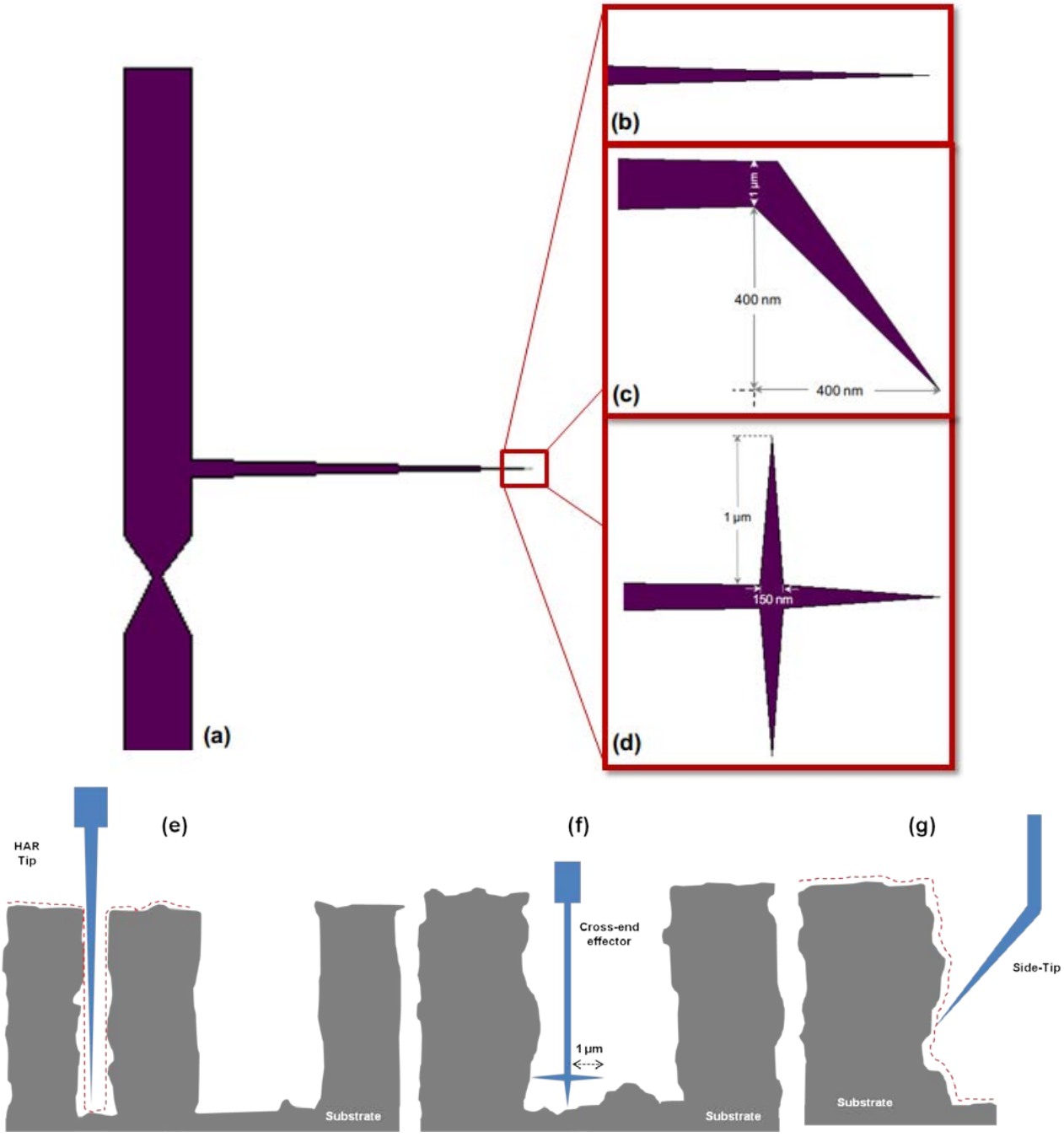

Figure 13 A NanoBit pattern with designated end-effectors are sketched: (a) NanoBit body, (b) tapered HAR tip, (c) deflected end-effector of side-tip, and (d) cross-shaped end-effector. (e-g) From left to right: illustrations of HAR tip, cross-shaped tip and side-tip in action.

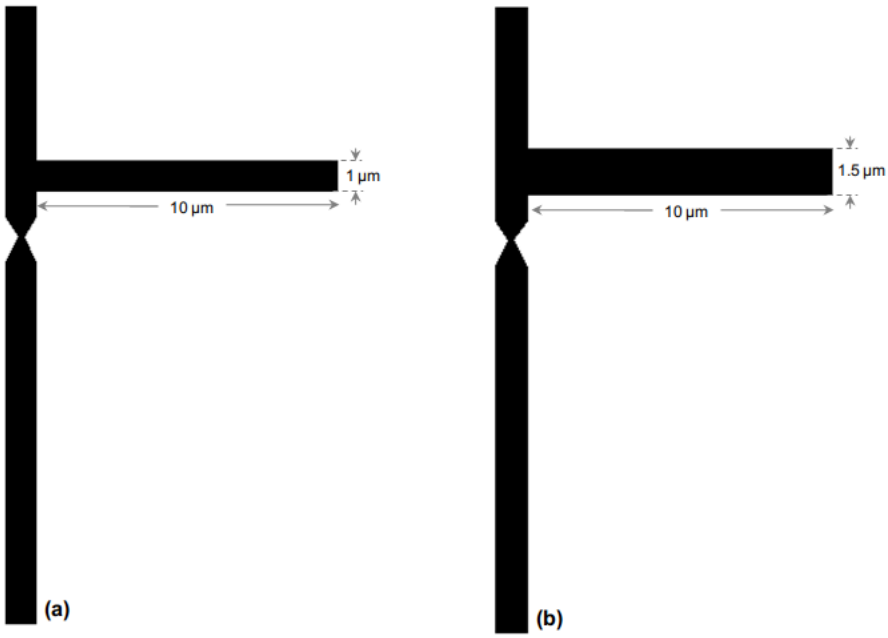

Figure 14 Two sorts of hybrid structures. NanoBit body preserves the dimensions mentioned earlier, whereas "tips" are longer (10 µm) and wider (1 µm, 1.5 µm) to give space for FIB processing.

TEMPLATES

All previous structures are designed to extend from the edge of a freestanding membrane. Membranes to hold the NanoBits and hybrid structures are 400-µm-wide and 80-µm-long. After the release of chips, 16 µm (excluding the additional length these structures add up) is planned to extend freely. In addition to these membranes, *templates* (membranes with no structures attached) were assigned to ~50 chips as the third kind. With templates, providing blank and large substrate blocks for FIB milling/prototyping is aimed. They are 400-µm-wide and 90-µm-long; the additional 10 µm length was introduced to provide an increased space for FIB processing (freestanding length: 26 µm). If needed, the templates can as well be shaped into cartridges for the NanoBits, which would save enormous fabrication time due to their thinness. Designed all three membrane kinds are shown in Figure 15 (finished structures are given in Figure 32).

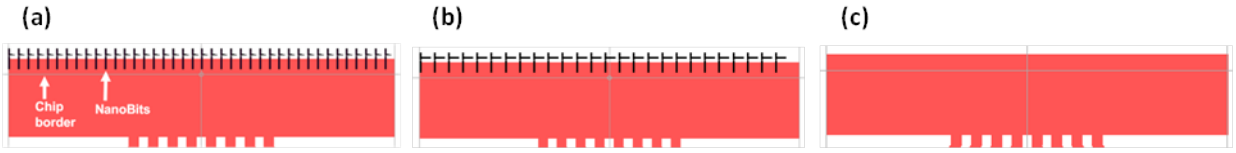

Figure 15 Tanner EDA layout editor L-Edit® snapshots of different membrane/template types. (a) Membrane with NanoBits at the edge; gray line extending across the membrane indicates the chip front-border; (b) membrane with hybrid structures; (c) a template (a long longer membrane without any patterns).

3 Fabrication

The NanoBits are precisely shaped microparts that can be cut out of a thin membrane of rigid material, such as SiO_2, Si_3N_4, Si, diamond or hard metals. Two main approaches can be used to make high aspect ratio NanoBits with a small tip diameter by *cutting* structures in a membrane: EBL and ion beam milling. Both methods focus a beam of charged particles onto a surface, allowing the beam to scan the surface with nanometer precision, to transfer the desired pattern. The basic principle of pattern transfer, however, is completely different. In Table 6 we briefly highlight the differences as relevant for NanoBits fabrication.

Table 6 Properties and features of EBL and FIB milling concerning NanoBits fabrication.

Electron beam lithography	**Focused ion beam lithography**
Electrons	Ions (7k-100k times heavier)
Changes locally the solubility of a thin polymer film, which after dissolution is used to make a metal mask for a highly directional reactive ion etching process that eventually defines the structure.	Directly knocks out atoms of the target material, which leave the target, redeposit on the target, or move in the material and knock other atoms out.
Serial process, but can be quite fast: 3000 $\mu m^2/s$ (using a JEOL JBX9300FS electron beam lithography system). Advantage: very fast.	Serial process, much slower.
Requires the EBL step to be carried out before chip fabrication; patterns have to be decided when starting the nanofabrication.	Can be carried out on finished chips, which can then be equipped with a "blank" writing area. Advantage: the chips can be fabricated without knowledge of the shape or function of the final device/NanoBit.
Presumably fastest for mass production	Presumably fastest for prototyping and development
Highest throughput	Most flexible
Less problems with contamination, amorphisation, and drift (because EBL is much faster).	Less problems with fabrication process: lithography is the last step.
Requires a well-equipped cleanroom	Can be done without a cleanroom, provided a stock of pre-made template chips is available.

3.1. Focused ion beam milling

The manufacturing of NanoBits by focused ion beam milling was led by Dr. Alexey Savenko, while I helped in preparations of the pattern files, designing of the NanoBits and contributed in discussions for attainment of sharper, high-quality NanoBits. The details of fabrication and the images in this dissertation are reproduced with his permission.

FIB milling is sculpturing of a substrate material, where a highly energetic ion beam ablates targeted substrate atoms through irradiation. The NanoBits are fabricated in DTU Center for Electron Nanoscopy (CEN) using Quanta 3D and Helios NanoLab FIB/SEM dual-beam systems – both systems use 30 kV gallium ions (Ga^+) – for FIB milling, and microchips with freestanding membranes made of Si/SiO_2 (bilayer), Si and Si_xN_y for the NanoBits.

FIB mills one point at a time, hence overall pattern should be determined as a sequence of serial milling points. To-be-exposed area can be introduced as a bitmap, stream file or be drawn on the spot by operator manually. Following the determination of exposure dose and current depending on the substrate properties (material, thickness, desired feature size, etc.), FIB milling is performed in one of the three ways:

I. Raster scan,

II. Circular (or elliptical) scan,

III. Large-area-first (or Milling-toward-edges) type scan.

Raster scan is the conventional sweep method where a beam of ions (or electrons, in respective machinery) scans one line—sideways or vertical—with sequential dot exposures, then moves to the second line and continues until whole pattern is swept. Circular scan, similar to raster scan, exposes a line of dots but differs in two ways: dots are not irradiated in juxtaposition, and the trajectory of a scan-line inscribes an arc instead of a straight line. The large-area-first type approach takes into account the specifics of the pattern to be milled; that is, ion beam is instructed to start milling from the center of largest area, then proceed to a smaller area, continue in this fashion and eventually, finish by scanning fine-featured areas.

FIB milling suffers from several serious artifacts, including drift (unwanted movement of the sample during milling), re-deposition (unwanted deposition of material that has already been removed from another part of the structures) and amorphisation (unwanted destruction of the crystal structure which leads to degraded mechanical and electrical properties) due to multiple exposures. In Figure 16 exemplary drawings of re-deposition and stage drift is given.

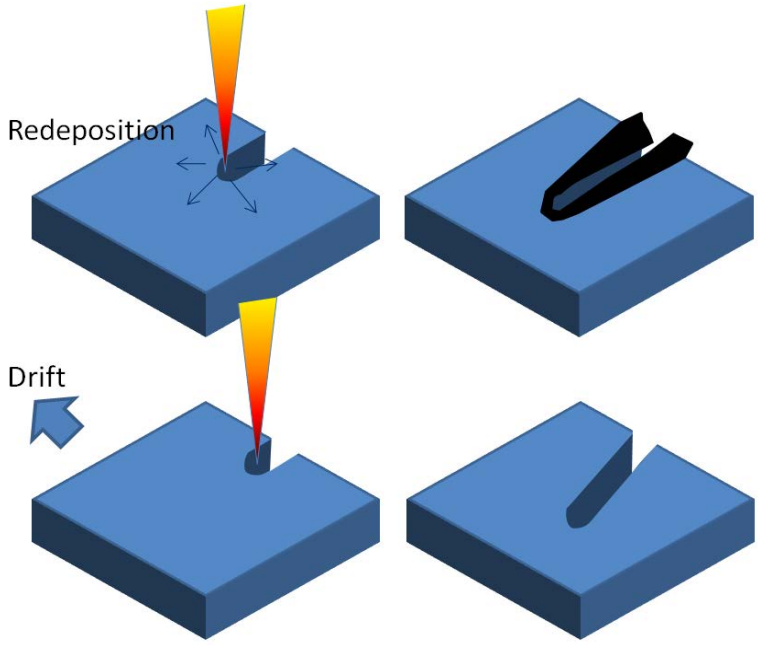

Figure 16 Top: illustration of redeposition. The material (black) being sputtered, redeposits on earlier-made structures and reduces their dimensions, with earliest structures receiving the largest amount of material. Bottom: illustration of drift. If the sample moves during milling, the structures will be deformed. Proper milling strategies reduce these problems.

During milling, ion beam sputters substrate material via energetic Ga ions, but sputtered substrate atoms, molecules, even clusters in return deposit on the milled regions, called re-deposition. This artefact can be rid by using the back-scan method which allows ion beam to reverse its motion to re-expose the milled region. This re-exposure helps the operator to finely re-mill these parts, and thereby remove the re-deposited material.

Stage drift is a problem inherent to any FIB writing strategy; the level of the drift, however, can show variations across different machines and for different writing strategies. Circular and large-area-first scan types had originally been developed in order to circumvent this problem encountered with Quanta 3D system [33]. On the other hand, Helios NanoLab system does not suffer from the drift as much, leaving amorphisation as the only major problem that needs tackling.

Multiple-exposure of an area occurs in the circular scan. Since the points to be exposed cannot be arranged in sequential order, the ion beam bounces back and forth within the arc trajectory, exposing a certain area multiple times. Multiple exposures can cause material to amorphisise, go soft, leading to accumulation of soft material in clusters, and eventually the formation of *blobs*.

During the initial stages of the fabrication however, regardless of FIB milling strategy used, blobs were observed on the very tips and edges of the NanoBits that had aspect ratios higher than 5 (see Figure 17). To tackle the blob formation, raster scan was combined with the circular scan. By this way, dots are exposed in sequential order following an arc line. This method not only decreases the total milling time but also prevents multiple-exposure of an area. NanoBits were most frequently milled using this sweep strategy combining two scan types. Although this strategy helped in riddance of the blobs on the devices, tips continued to bear the artefacts. It was clear that the material here was entirely amorphisised and that the energetic Ga ions were sufficient to amorphise a region in a single exposure given the target structure is

slender enough. Formation of blobs at the very tip of NanoBits was eventually eliminated by leaving such delicate points – connector and break-point included – attached to the milling frame and detach-milling in the very end.

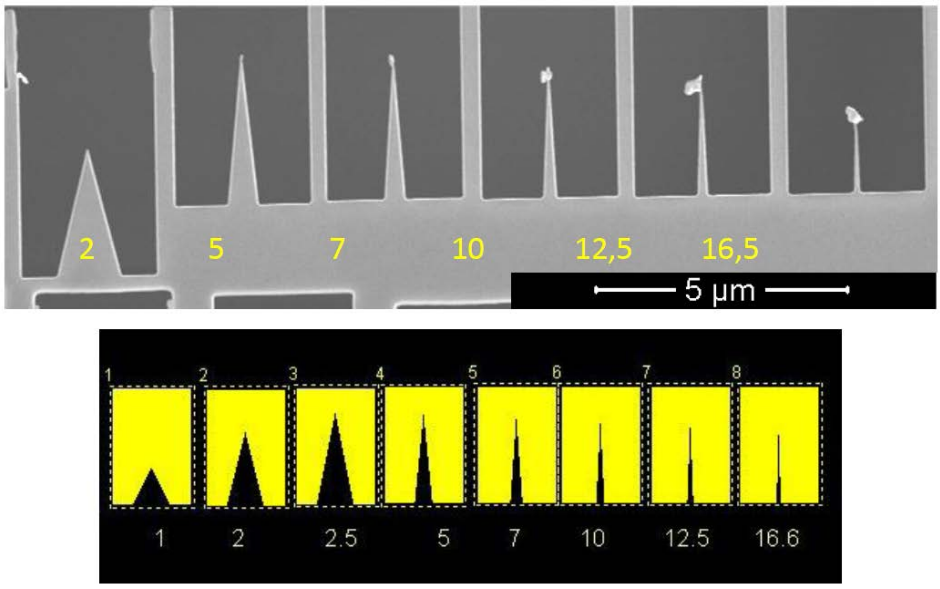

Figure 17 Blob artefact formation due to amorphisation at the structure borders.

The latest and most advanced milling strategy utilises all three scan types, includes the back-scan, and is carried out in Helios NanoLab dual-beam system. In this combined strategy, (i) raster with circular scan allows sequential milling of to-be-exposed dots with minimum stage drift; (ii) large-area-first scan prevents damaging of three critical areas, i.e. NanoBit tip, connector and break-point; (iii) back-scan removes the re-deposited material; and lastly (iv) detach-milling ensures the integrity and finesse of the final NanoBit structure by precluding blob formation due to amorphous structure. The three scan types and final combined strategy is illustrated in Figure 18 with the SEM images of NanoBits shaped by the respective strategy.

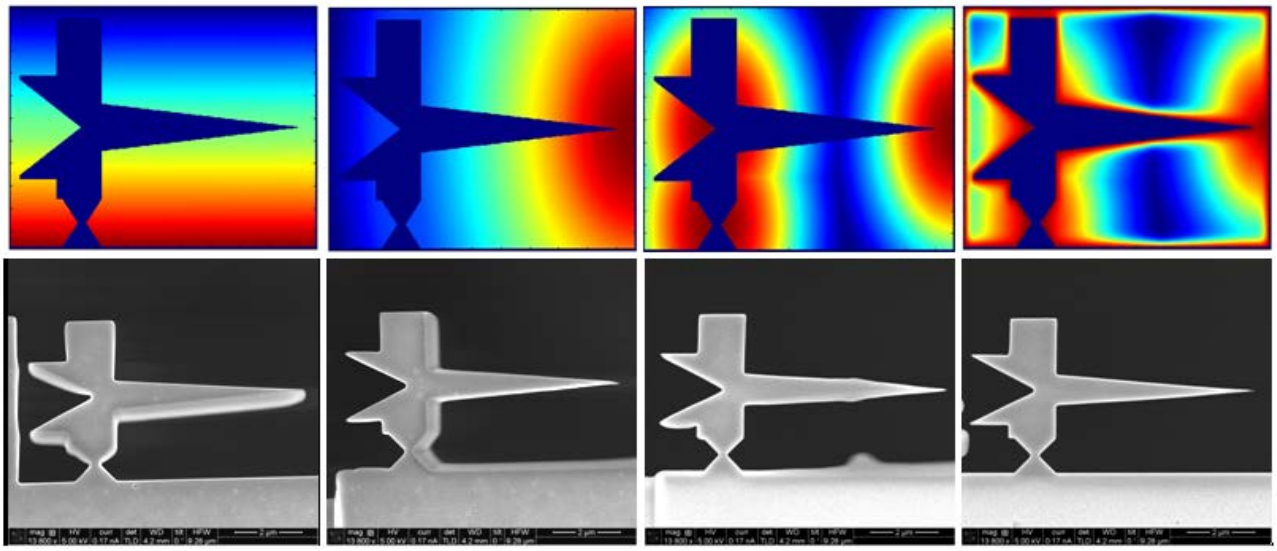

Figure 18 FIB milling strategies with resultant NanoBit structures below respective scans. Milling progresses from dark blue to dark red. (From left to right) raster scan from top to bottom; circular scan with tip milled last; circular scan with three points milled last; combination of raster and circular scan with same three points being milled last.

In Figure 19, NanoBits defined on a Si NEMbrane, protruding from the edge are shown. Depending on the manipulation scenario and topography to be imaged by AFM, NanoBits can be milled with appropriate connectors (triangular, flat or step) and end-effectors (tapered, side-tip, cross) in a very short time. SEM micrographs of few examples are given in Figure 20.

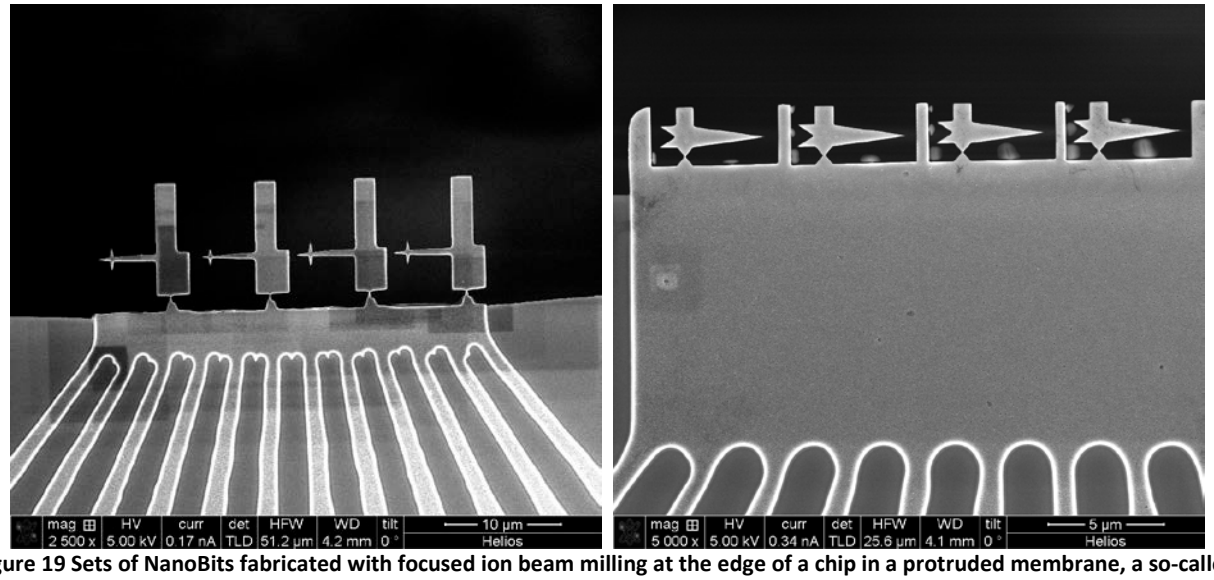

Figure 19 Sets of NanoBits fabricated with focused ion beam milling at the edge of a chip in a protruded membrane, a so-called NEMBRANE.

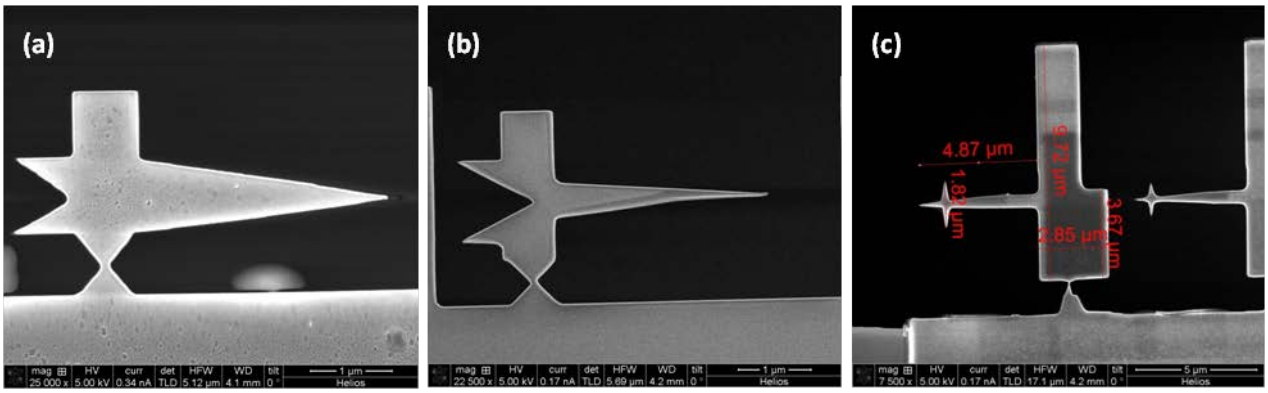

Figure 20 Experimental samples of NanoBits. (a) Aspect ratio (AR): 3.5; (b) AR: 6.5, (c) NanoBits with the connector (top part) shaped for slit insertion experiment.

3.2. Electron beam lithography

3.2.1. Basic principles

Electron beam lithography is a special technique developed to create very small patterns. EBL uses a concentrated beam of electrons to scan a surface covered with an electron-sensitive resist. Irradiation of this polymer-based resist entails some changes in its microstructure: breaking (scission) or formation (cross-linking) of molecular bonds; depending on the effect, the resist is called positive or negative (tone) resist. The accurate control and deflection of the electron beam can then provide writing of any pattern with very high resolution in nanometer range, close to the incident beam size.

An electron beam writer mainly consists of an electron emitter (or electron gun) to produce electrons, lenses, a deflector to accurately deflect the beam, apertures to define the beam, a stigmator to correct astigmatism, a blanker to turn on and off the beam, and an electron detector for locating the marks on the sample.

3.2.2 Resolution

Beam diameter:

The highest achievable resolution with EBL is determined by combination of a number of factors affecting the beam diameter and those arise from electron-substrate interaction.

Electrons can emanate from the electron source in three ways: by thermionic emission, by cold field emission, and by thermal field (Schottky) emission (a combination of the former two). Common types of electron sources are listed in Table 7.

Table 7 Properties of common electron emitters [34].

Source type	Brightness [A/cm^2-sr]	Source size [nm]	Energy spread [eV]	Vacuum requirements [Torr]
Tungsten (W) thermionic	~10^5	~25,000	2-3	10^{-6}
Lanthanum hexaboride (LaB_6)	~10^6	~10,000	2-3	10^{-8}
Thermal (Schottky) field emission	~10^8	~20	0.9	10^{-9}
Cold field emitter	~10^9	5	0.22	10^{-10}

In thermionic emitters, the source material (e.g. W coil) is heated up by passing current to provide electrons sufficient energy to overcome the work function of the conductor. The temperature T governs the distribution of electrons around the Fermi level, E_F, by Fermi-Dirac distribution:

$$F(E) = \frac{1}{e^{(E-E_F)/k_BT}+1}, \quad (1)$$

where E is the electron energy and k_B is the Boltzmann constant. As T increases, electrons occupy higher energy levels, which is characterised by the Boltzmann distribution: $F(E) \rightarrow \exp[-(E-E_F)/k_BT]$ (see Figure 21). Electrons with energies higher than the work function leave the source and form the beam. The field emitters are basically sharpened conductor needles that allow creating very high electric fields. With sufficiently high electric fields, the vacuum level of the electrons can be lowered, thereby enabling electrons to tunnel into the vacuum.

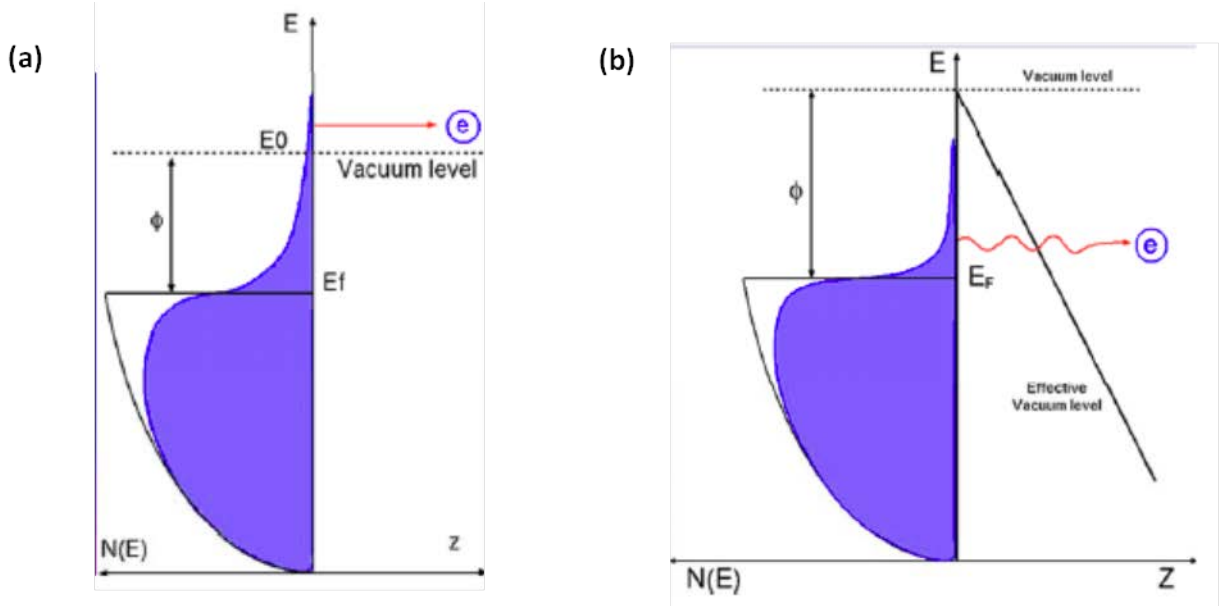

Figure 21 Boltzmann distributions of electron energy levels with increasing temperature. (a) thermionic emission and (b) field emission of electrons from the source filament.

Schottky emitters utilise both the electric field and thermionic sources with only sharper tips; thus, they can deliver higher brightness than the thermionic emitters while having source sizes and energy spread comparable to cold field emitters. The virtual source sizes are given in Figure 22.

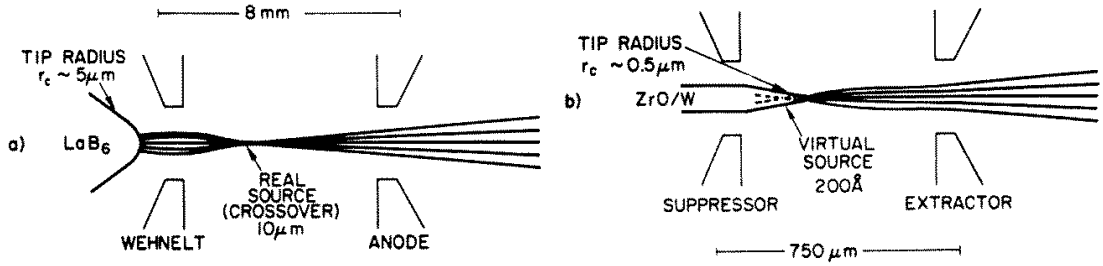

Figure 22 Source sizes of (a) a thermionic emitter (LaB_6) and (b) a field emitter [34].

The source size is important since this determines the degree of demagnification, M, required to obtain a small beam diameter. The resultant beam diameter is a function of virtual source size, d_v, and demagnification: $d_g = d_v/M$. Brightness is the current density of the beam per solid angle, and is rather a measure of beam dwell time on a certain spot to fully develop the irradiated area.

Electrons with a large energy spread cause the chromatic aberration, d_c: the electrons with lower energies are focused at a larger angle than the electrons with high energies. This effect results in widening of the beam diameter and is given by $d_c = C_c\alpha(\Delta E/E)$, where C_c is the chromatic aberration constant, α is the convergence half-angle of the beam, ΔE is the energy spread, and E is electron energy. In a similar manner, electrons far from the optical axis are focused more strongly by lenses. The effect is called spherical aberration and relies heavily on the quality of the lenses; beam diameter is $d_s = (C_s\alpha^3)/2$. Figure 23 illustrates the chromatic and spherical aberration.

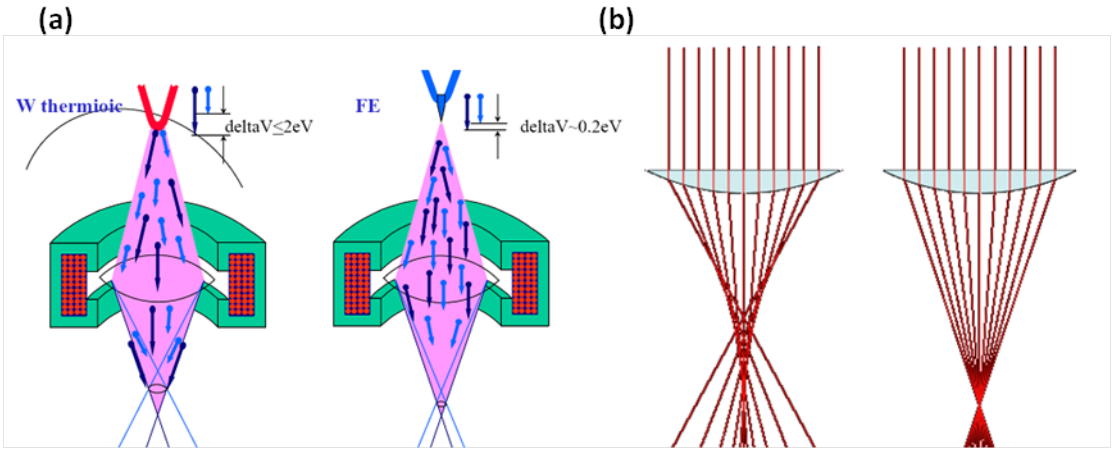

Figure 23 Schematic representations of (a) chromatic and (b) spherical aberrations.

The electron diffraction contributes to beam diameter by $d_d = 0.6(\lambda/\alpha)$, where electron wavelength $\lambda = 1.2\ E^{-0.5}$. The final theoretical beam diameter before exposing the target material is determined by adding these factors in quadrature:

$$d = \sqrt{d_g^2 + d_c^2 + d_s^2 + d_d^2}. \quad (2)$$

A theoretical *d* estimation for the JEOL JBX9500FS e-beam writer at DTU Danchip is made in Figure 24 by assuming C_c = 25 mm, C_s = 45 mm, beam current *I* = 1 nA, and the effective beam size was calculated by

$$F(r) = \frac{1}{2\pi d} e^{-\left(\frac{r^2}{d^2}\right)}, \quad (3)$$

assuming the contribution of each parameter above is Gaussian. The actual beam diameter (~10 nm) is higher than the theoretical 6 nm.

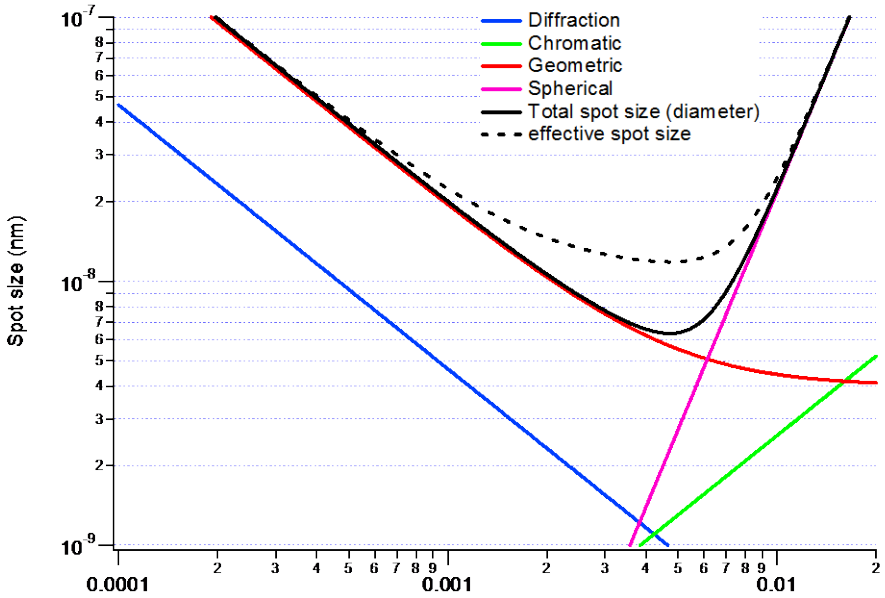

Figure 24 A theoretical estimation of beam diameter for 100 keV JEOL JBX9500FSZ e-beam writer.

Electron-substrate interaction

When an accelerated electron beam is directed to a substrate, the primary electrons penetrate into the substrate and undergo elastic and inelastic scattering. Inelastic scattering occurs when the incident electrons collide with the valence electrons of the substrate or resist nuclei. The collision can result in ionisation of the atom (secondary electrons (SE)), excitation of the valence electron, photon emission or heat, and primary electron loses some of its energy. Scattering angle is small. In elastic scattering, the electrons are scattered due to Coulomb interaction with the substrate nuclei and the scattering angle is large. These backscattered electrons (BSE) can be directed towards the surface and leave the substrate exposing the resist.

The forward scattering and backscattering deposit energy to the resist; the energy profile is modelled as a combination of two Gaussian distributions [35]:

$$f(r) = \frac{1}{\pi(1+\eta)}\left[\frac{1}{\alpha^2}e^{\frac{-r^2}{\alpha^2}} + \frac{\eta}{\beta^2}e^{\frac{-r^2}{\beta^2}}\right], \quad (4)$$

where α and β are forward scattering and backscattering range parameters, respectively, and η is the ratio of backscattered electrons. The simulation of the two-Gaussian distribution and a representative sketch of the scattering process are given in Figure 25.

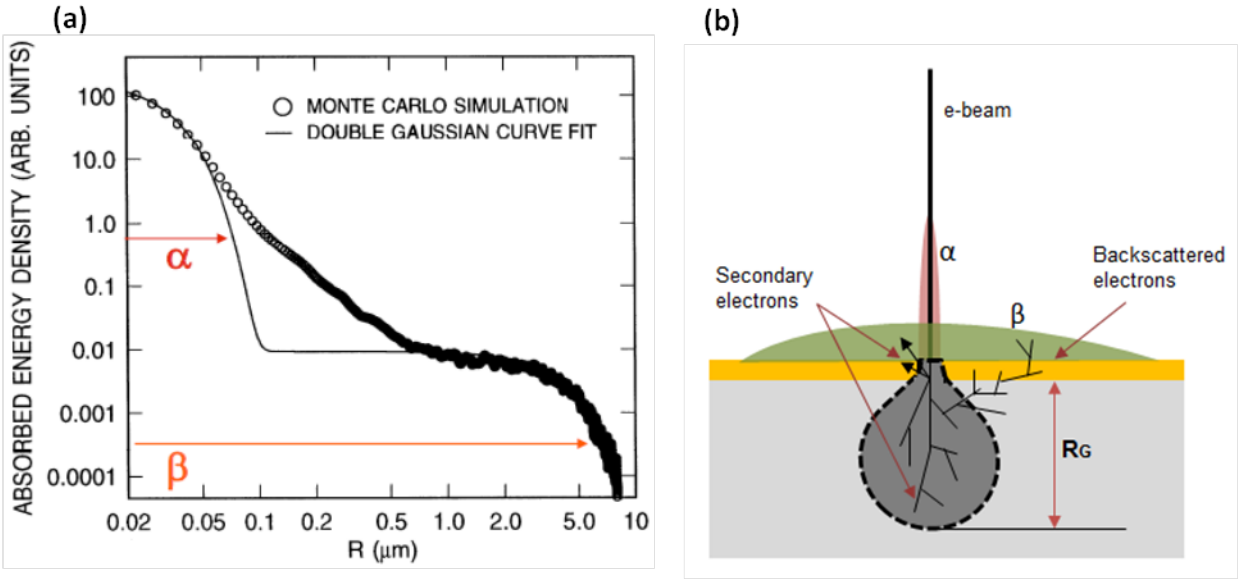

Figure 25 (a) Gaussian distributions of energy profiles and (b) schematic of scattering process.

Inelastic forward scatterings exposes the resist and increases the beam diameter by $d_f = 0.9(h/V_b)^{1.5}$, where h is the resist thickness and V_b is the beam voltage. Table 8 lists these parameters as a function of beam energy for 0.5 μm resist on Si substrate, where α is calculated, β and η are experimentally found.

Table 8 Scattering parameters as a function of beam energy. The values in brackets are extrapolations [36].

Beam energy (keV)	α (μm)	β (μm)	η
5	1.33	[0.18]	[0.74]
10	0.39	[0.60]	[0.74]
20	0.12	2.0	0.74
50	0.024	9.5	0.74
100	0.007	31.2	0.74

For the e-beam writers with very high beam voltages, such as 100 keV, suffer less than those with lower energies. However, even with 100 keV beam, 7 nm increase in the beam diameter is observed; adding to the 10 nm actual beam spot size found before (cf. Figure 24), the expected resolution is lowered to the range of 20 nm. As the beam voltage increases, β increases as well, since the BSE emanates from deeper within the substrate. When energetic, the primary electrons penetrate the substrate, they collide with particles elastically and inelastically, travel a certain distance in the matter, lose energy, and finally come to halt. This total vertical distance covered by electrons is called the Grün range, R_G (see Figure 25), and given by:

$$R_G = \frac{4.6\times10^{-6}}{\rho} E^{1.75}, \quad (5)$$

in units of cm. ρ (g/cm^3) is the substrate density and E is the electron energy (keV). That is, electrons with higher E's travel deeper into the matter, e.g. Si, as well as widening the breadth of the Grün range profile, which allows SEs leaving the substrate at distant points, exposing the resist. The range of BSEs for different materials is given in Figure 26.

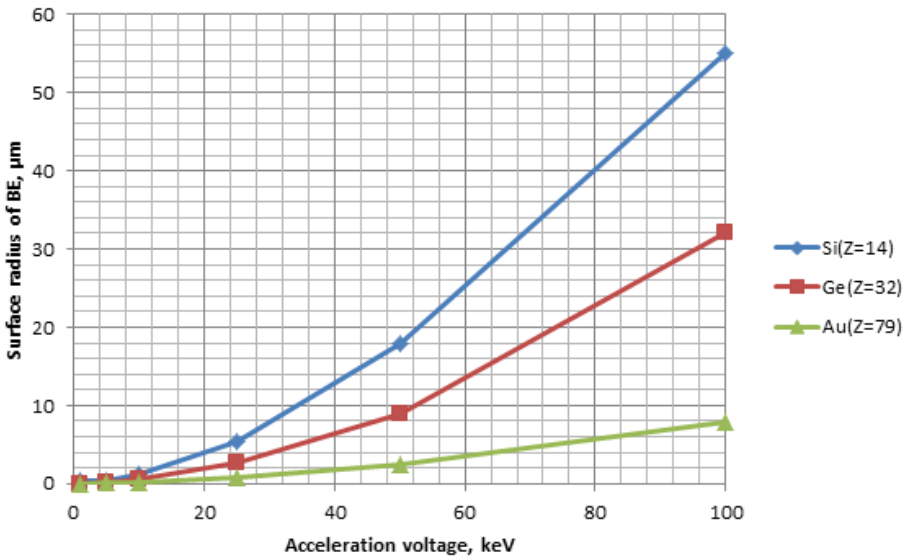

Figure 26 BSE electron range as a function of e-beam acceleration voltage for different materials.

This undesired, extra exposure of the resist is called proximity effect. Proximity effect can be tens of microns for 100 keV e-beams, as can be seen in Table 8. Therefore, realisation of the closely packed dense structures and/or small features becomes difficult, lowering the resolution the resolution even further to >20 nm. The proximity effect can be reduced to an extent by dose (energy deposition to a point) modulation or pattern modification.

3.2.3 Properties of ZEP520A

EBL requires resists that can provide high resolution and preferably with high etch resistance. Polymethyl methacrylate (PMMA) is the first e-beam-sensitive polymeric material discovered [37]. The most distinctive features of PMMA are high resolution, high contrast, and low sensitivity. Feature sizes below 20 nm allowed PMMA to find wide use until to date. Resist contrast is a measure of its sensitivity to a certain dose range, or how immediately the exposed molecular bonds can be broken (for positive resists) along thickness. A schematic of contrast is given in Figure 27, and defined mathematically as

$$\gamma = \left(\log_{10}\frac{D_f}{D_0}\right)^{-1}. \quad (6)$$

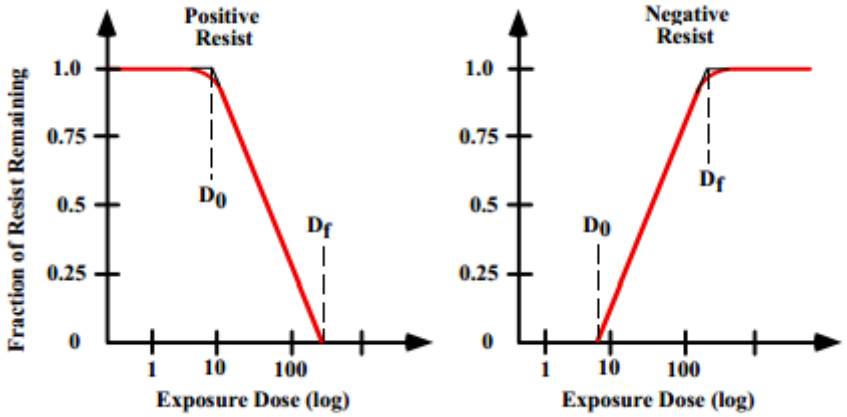

Figure 27 The contrast of a resist is defined by the initial dose, D_0, and the clearing dose, D_f.

The resist sensitivity indicates the level of required dose to start to break the bonds in a resist. Lower doses denote highly sensitive films to the incident irradiation, and are favourable regarding that the EBL is a costly technique. The writing time of a pattern is governed by

$$t = \frac{DA}{I}, \tag{7}$$

where *D* is the electron dose, *A* is the exposure area, and *I* is the current. The necessary dose to develop the e-beam resist is directly proportional to the writing time.

ZEP520 resist was developed to replace PMMA. The positive-tone e-beam resist ZEP520, produced by Zeon Corporation, is a copolymer of methyl (α-chloroacrylate) and α-methylstyrene [38]. The characteristic features of ZEP520 follow as high resolution, high contrast and high sensitivity. Its sensitivity is reported as 5-10 times higher than PMMA whereas the dry etch resistance is at least 5 times higher [39]. Table 9 compares a variety of e-beam resists irradiated by 20 keV.

Table 9 Conventional e-beam resists and properties.

Resist	Resist tone	Resolution	Sensitivity	Developer
PMMA	+	10	100	MIBK : IPA
ZEP520	+	10	30	xylene : p-dioxane
ma-N 2400	-	80	60	MIF726
EBR-9	+	200	10	MIBK : IPA
PBS	+	250	1	MIAK : 2-pentanone 3:1
COP	-	1,000	0.3	MEK : ethanol 7 : 3

The type ZEP520A available at DTU Danchip and used in this work is diluted with anisole, hence the name incorporates the letter A. The contrast and sensitivity of a resist depends on the developer (resist solvent) type and beam energy. Figure 28(a) shows that the highest contrast for ZEP520(A) is attained ZED-N50 (*n*-amyl acetate) and MIBK : IPA (methyl isobutyl ketone : isopropyl alcohol) 1 : 3 while IPA:H2O fails to develop the resist fully. Additionally, the resist show the highest sensitivity when developed with ZED-N50 at room temperature (22°C). Figure 28(b) compares seven types of alkyl-acetate-based solvents: as the percentage of the alkyl group increases, the contrast increases but sensitivity decreases. ZED-N50 appears

as a good compromise between the two factors. In this work, ZED-N50 is used as the developer for ZEP520A as is also recommended by Zeon Corporation [40].

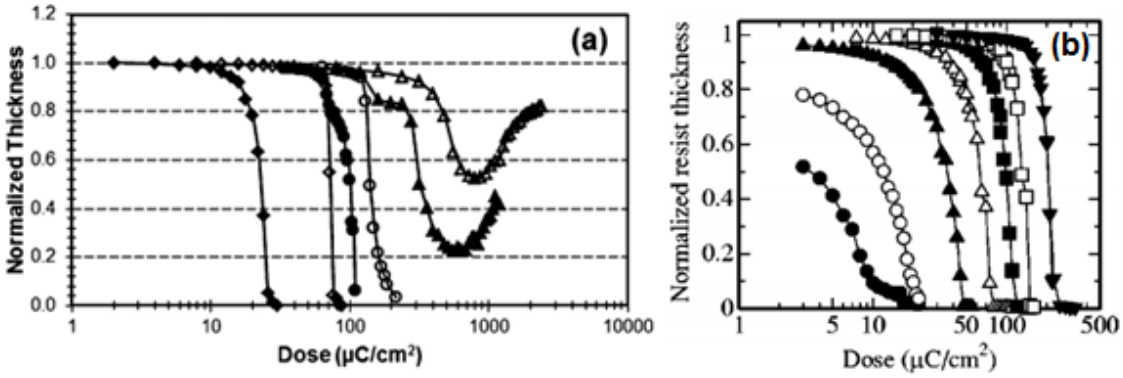

Figure 28 Contrast curves of ZEP520A e-beam resist developed with different solvents. (a) The patterns exposed with 10 keV. Developers ZED-N50 (diamond), MIBK : IPA 1 : 3 (circles) and IPA : H2O 7 : 3 used to develop the pattern at 22°C (filled symbols) and -15°C (open symbols). Image taken from [41] (b) Contrast curves of ZEP520 resist with *n*-alkyl-acetate developers: methyl-acetate (filled circle), ethyl-acetate (open circle), propyl-acetate (filled triangle), butyl-acetate (open triangle), amyl-acetate (filled square), hexyl-acetate (open square), and octyl-acetate (inverse open triangle). Beam energy: 70 keV. Image taken from [42].

In Figure 28, e-beam energies used are 10 keV and 70 keV in (a) and (b), respectively. For the same developer (ZED-N50), a decrease in sensitivity (or increase in required dose) is obvious. The required dose increased from ∼30 keV to ∼200 keV. This is expected because more energetic electrons collide dominantly elastically; therefore, energy deposition to the interacted resist decreases compared to the energy transferred by the less energetic through inelastic collisions. Absorbed energy density of a resist is given by the empirical formula by Greeneich [43]:

$$\varepsilon = \frac{DE}{eR_G}\lambda(f) \tag{8}$$

in units of eV/cm^3. D is the electron dose (C/cm^2), e is the electron charge, R_G is Grün range (cm), and $\lambda(f)$ is the depth factor given by

$$\lambda(f) = 0.74 + 4.7f - 8.9f^2 + 3.5f^3. \tag{9}$$

Dimensionless depth is given by $f = z/G_R$, where z is the depth in Grün range. As the beam energy increases, RG increases faster than the energy (cf. Eqn. 5). Thus, in order to deliver the required amount of energy to the resist, dose needs to be higher as well.

3.2.4 The JEOL JBX9500FSZ electron beam writer

The JEOL JBX9500FSZ at DTU DTU Danchip is a high-end e-beam writer. A sharpened ZrO/W thermionic field emitter (Schottky) is used as the electron gun. 100 keV beam energy and high brightness (∼10^8 A/cm^2-sr) offer a good compromise between the beam diameter (minimum 4 nm) and current (up to 100 nA). Fast electronics/scan speed (100 MHz) allow minimum time spent on the stage movement between exposures

of various points of the pattern. Combined with the fast scan speed, one can perform accurate mix-and-matching across a full wafer (full range: 23 cm × 23 cm) thanks to high-precision motor stage (0.15 nm).

3.3. Microfabrication

The microfabrication process was based on standard, standard microprocessing techniques. Most notably, electron-beam lithography was adopted for high resolution lithography; photolithography was included owing to its high throughput capability; and, chip-based production was pursued to create freestanding structures, hence render the NanoBits accessible. The use of wafer-scale electron beam lithography is not a cheap process, but considering that ≥10,000 NanoBits (if the wafer layout is targeted towards high numbers) can be made on a single wafer, the price per NanoBit is overlookable. Since electron beam writers with comparable quality to JEOL JBX9500FSZ at DTU Danchip is not commonplace in cleanrooms, it is appropriate to note here that the EBL is routinely used for making nanoimprint masks, which greatly lowers the production costs; this can be carried out with trivial changes to the process flow. Thus, it is reasonable to argue that the fabrication flow followed in this work can be conducted in most cleanrooms.

Substrate

Starting wafers are single-side-polished, p-type, 4” silicon wafers with <100> surface crystal orientation and 1–20 Ω-cm resistivity. On 10 wafers, 0.95 µm wet SiO_2 was grown at 1050°C, followed by deposition of 200-nm-thick pSi layer by low-pressure chemical vapour deposition (LPCVD) at 620°C. These layers were intended as buffer (or “etch-stop”, for later KOH bath) and device layers, respectively. Thickness measurements were done using Dektak 8 surface profiler.

Pattern definition

In the fabrication, one pattern for EBL and two masks for PL were prepared. EBL was intended for defining fine-featured structures (NanoBits and hybrids) whereas PL was intended to realise the chip-top and the release windows on the back. Tanner EDA Layout Editor (L-Edit) was used for all three patterns.

a) Electron beam lithography:

For the definition of NanoBits and hybrids, 180 nm ZEP520A (diluted by 1:1 in anisole) e-beam resist (EBR) was spun on one wafer at 1500 rpm with fully automatic Maximus 804 from ATMsse Gmbh (SSE Spinner), and baked at 180°C for 2 min. EBL was carried out with the following parameters:

- 100 kV e-beam voltage,
- 0.8 nA beam current,
- 300 µC/cm² (for hybrid structures, logs and handles of the NanoBits) and 350 µC/cm² dose (for NanoBit tips).

EBR development recipe follows:

- Immersion into ZED-N50-filler petri dish: 2 min,
- IPA flush: 30 s,
- DI water rinse: 3 min,
- Blow-dry by N_2 gun.

For metal lift-off, 20 nm Cr was electron beam evaporated in Wordentec QCL 800 vacuum deposition system. As the lift-off metal, Cr was selected instead of more common Al due to its selectiveness against sodium hydroxide (NaOH). NaOH is inherent to AZ5214 photoresist (PR) developer (Developer AZ 351), which would be used after photolithography with lift-off metal still present. Lift-off was done by introducing the Cr-deposited wafer into a petri dish filled with 1165 solution. The petri dish was disturbed gently to create a circular flow of the solution around the EBR for 2 min, and then the wafer was rinsed with wafer for 30 s. The same treatment was repeated few times until no visible particles floated in the solution and applied ultrasound with 5 W for 2 min.

Measured minimum feature sizes (NanoBit tip diameters) were 20±5 nm. Figure 29 shows a descriptive SEM micrograph. Two additional wafers were processed in the same way.

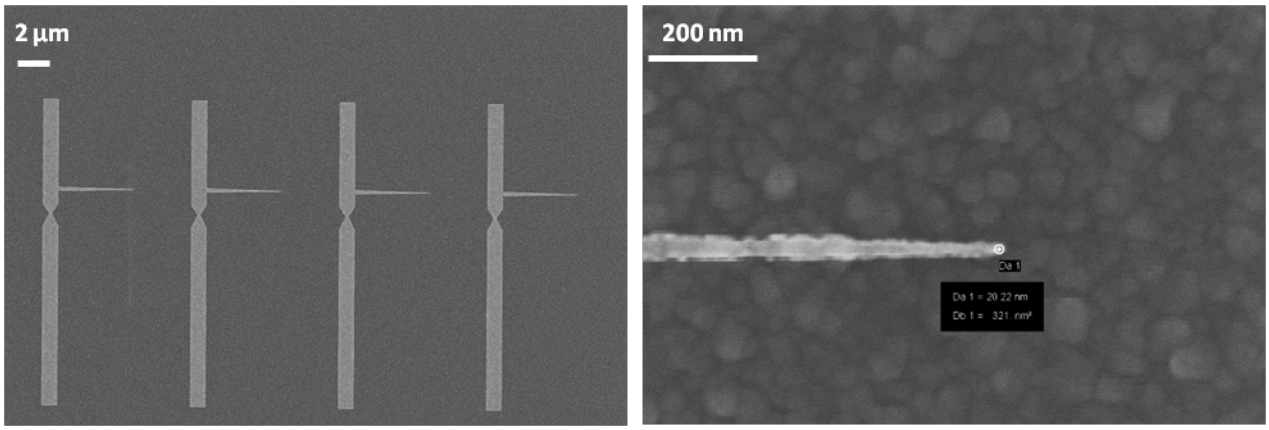

Figure 29 SEM images showing (left) 4 NanoBits after Cr lift-off; (right) tip diameter: 20 nm.

b) Photolithography:

With the e-beam patterns (NanoBits and hybrids) defined, front-PL was done to finalise the chip-top mask. All four wafers were hexamethyldisilizane (HMDS)-primed in Star2000 HMDS/Vapor Prime Oven from IMTEC (HMDS Oven). During priming, surface OH groups (if the wafer is hydrophilic due to native oxide or other hydrophilic material) are bound with HMDS, making the surface hydrophobic; this process is essential for adhesion of PR onto the wafer surface. 1.5-µm-thick AZ5214 resist was then spun on wafers and baked at 90°C for 2 min using SSE Spinner. The alignment of e-beam pattern to the front-side mask was done with EVG 620 Double-side Mask Aligner; PR was exposed for 3 s and developed with Developer AZ 351 for 70 s. Optical microscope images showed successful alignment of two patterns (see Figure 30).

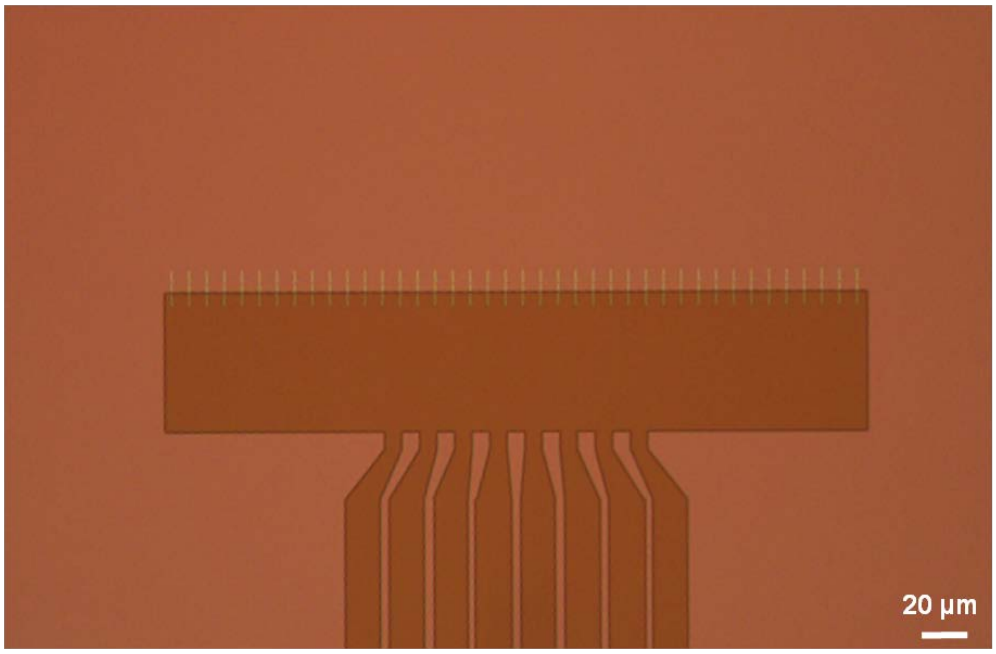

Figure 30 EBL & PL mix-and-match. PL mask is well aligned to e-beam NanoBit patterns.

In the case of failure to obtain a good mix-and-matching, the user is advised not to perform ashing of the PR since the O_2 plasma will remove the thin metal layer, as well. Instead, 30-min-soak in acetone should remove all PR – if PR residues are still present, 10 min of in 7-up solution (contains 98% H_2SO_4 and $(NH_4)_2SO_4$) should ensure entire removal of the residues.

With the topside mask finalised, the layout was transferred to pSi by RIE using SPTS ICP Metal Etch MP0637. To avoid any damage to the delicate structures, wet treatment was preferred: PR was removed following acetone dip and 7-up chemistry; Cr was etched by a commercial Cr-etch solution.

Backside processing

Microchips with freestanding NEMbranes were realised by selective potassium hydroxide (KOH) etch. Standard 28 wt% KOH etches Si <100> at a rate of 1.3±0.1 µm/min at 80°C while etch rate of Si <111> surface is negligibly small (if not zero). For definition of the microchips, etch-windows needs opening on the backside via RIE, through which KOH would etch the bulk Si until the buffer oxide on the topside. Once the windows are opened, pSi and SiO2 layers that were also deposited on the wafer back would be exposed, which would jeopardise a successful KOH etching since the etch rates of pSi and SiO2 are ≥1.3 µm/min and 6 nm/min, respectively. While relatively low etch of SiO2 is advantageous for using as an etch-stop layer, this layer may be etched utterly (together with pSi) depending on exposed surface area on the backside. Therefore, before any further processing, frontside was protected with 10-µm-thick AZ4562 PR, and these two layers on the back were etched by RIE in RIE1: part of STS Cluster System C010. PR was removed afterwards.

To protect the frontside against backside processing and KOH chemistry, firstly, the wafer was deposited 250 nm low-stress (Si-rich) Si_xN_y at 835°C using Tempress LPCVD nitride furnace. Etch rate of silicon nitride in KOH is negligible. Then, onto frontside 10-µm-thick AZ4562 PR was spun to protect the nitride layer

against scratching or any kind of damaging. For the backside PL, same steps as the frontside PL were followed. Si_xN_y openings on the back were etched using RIE1. After removing the PR, the wafer was put into KOH etch for 6 h. Figure 31 shows the wafer frontside and backside after KOH.

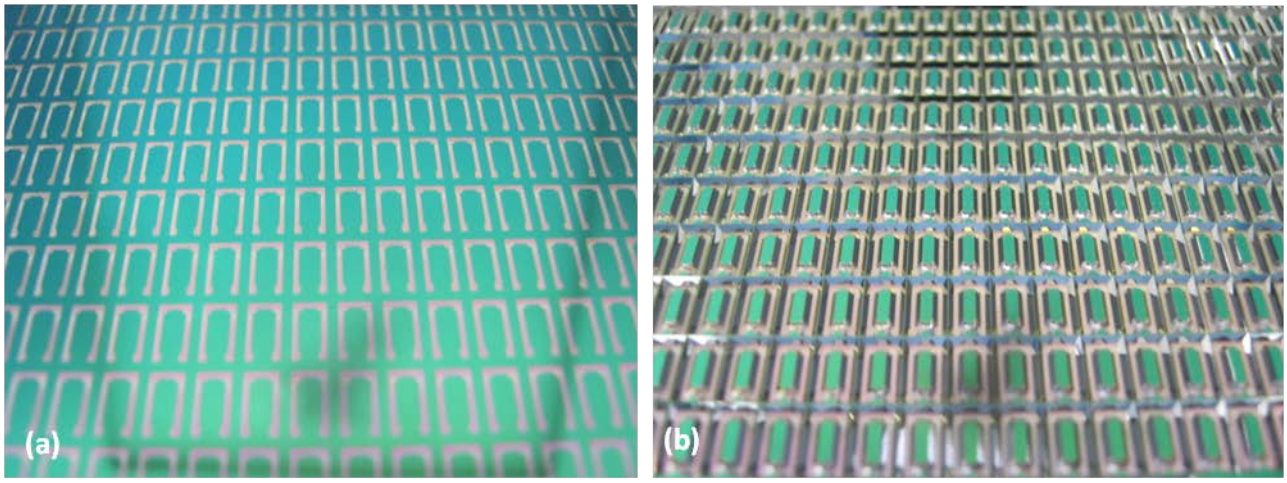

Figure 31 LPCVD nitride-protected wafer (a) frontside and (b) backside after KOH etch.

Chip release: suspended structures

Microchips with NanoBits, hybrids and templates were eventually released by etching first the Si_xN_y in phosphoric acid (85 wt% H_3PO_4) at 180°C, and then the SiO_2 layer in buffered hydrofluoric acid (BHF). Figure 32 provides the optical microscope images of the chips before and after the release.

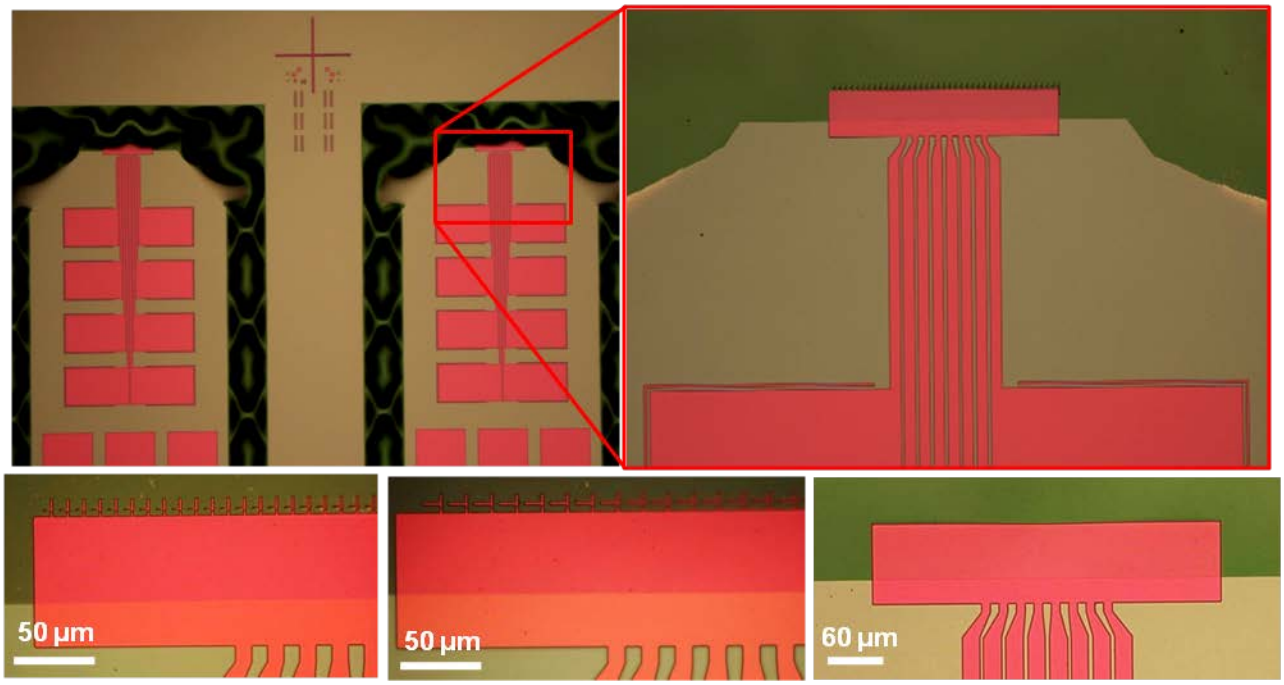

Figure 32 (a) Two chips after KOH, (b) microchip with NanoBits protruding from the NEMbrane edge, (c-e) magnified images of NanoBit (sidetip) array, hybrid structures and a template, respectively.

The fabrication process took place in DTU Danchip cleanroom facilities and considers the batch production of pSi NanoBits, hybrids and templates. The main fabrication steps are provided in Figure 33.

Figure 33 Main steps of NanoBits fabrication flow: (a) NanoBit patterns are defined via EBL; (b) metal lift-off; (c) transfer of topside pattern to device (pSi) layer; (d) SixNy deposition and back-side UVL; (e) KOH etching until oxide, followed by total etching of nitride layer and underetching of SiO_2.

4 Characterisation & Postprocessing

4.1. Critical parameters

The critical parameters and dimensions of the structures are defined by a combination of requirements set by target surface topography, assembly and usage scenarios. The significant elements follow:

Tip/end-effector sharpness: sharp probe tips are essential for precise and correct measurement of the surficial features, such as surface/sidewall roughness and grain morphology. Sharper tips provide more detailed information about the topography under investigation, and thus largely favourable. (With 0.8 nA e-beam current, the minimum beam diameter, thus the smallest attainable feature size is ~20 nm. Tip diameters ≤30 nm are aimed with NanoBits.)

Tip aspect ratio: high-aspect-ratio surface structures like vias and feed-throughs require AFM tips that could reach the trench bottom, or in the case of pillars, AFM tip should provide the correct step height with the minimum possible convolution. (HAR NanoBits were designed to have AR = 20.)

Break-point: regardless of the assembly scenario to be used, the break-point should be mechanically stiff to hold the NanoBit in the fabricated position whereas it should be delicate enough to allow either microgripper or the AFM probe to detach the NanoBit. (Based on early experiments on FIB-defined NanoBits, the break-point was designed 150-nm-wide.)

Tip's distance to NEMbrane edge: in the microgripper-based manipulation scenario, an electrothermal gripper is used. When a positive voltage is applied, the gripper jaws reach higher temperatures due to Joule heating and extend forward and toward each other. During gripping of the NanoBit by the handle and breaking from the break-point, the end-effectors keep extending, therefore pushing the NanoBit towards the NEMbrane edge. To avoid any NanoBit tip damage, the tip should be sufficiently distant from the NEMbrane. During mix-and-match, this distance was aligned to 4.5 µm.

Handle dimensions: the length, width and thickness of the handle are of utmost importance since they determine (i) the level of ease while picking up with the gripper, (ii) the bonding strength with the plug, and relatedly, (iii) the reliability during surface imaging. (Design dimensions: 7 µm x 1 µm x 0.2 µm.)

4.2. Scanning electron microscope metrology

4.2.1. Basic principles and electron-substrate interaction

The operation principles of SEM are virtually identical to electron beam writer (see section 3.2). Briefly, electrons are emitted from a source gun (thermionic, Schottky, cold field emitter), condensed with electromagnetic lenses, beam diameter narrowed down by the apertures and the final few-nanometer-wide beam (cf. Figure 24) impinges on the target sample.

Upon interaction with the substrate, impingent (or primary) electrons (PE) create BSEs and SEs. SEs can be divided into two categories: the ones created directly by the PE (SE1) and the ones created by BSEs (SE2). On a typical conducting sample, 10–30% of the PEs become BSEs with energies reaching 50% of the PE. The fraction of the BSEs depends on the atomic number and the surface geometry of the substrate [44]. Since the BSEs have high energies and undergo elastic scattering, they reach deep into the matter and reflect at high angles, delivering matter interior information. This range was formulated by Kanaya and Okayama [45] as

$$R = \frac{0.0276AE_0^{1.67}}{Z^{0.889}\rho} \tag{10}$$

in units of μm. Using Eqn. 10 the approximate range that electrons can reach in silicon is given in Table 10. SEs are classified as the electrons with energies 1–50 eV [44]. These are created by the inelastic scattering events and carry information about the substrate surface or near-surface depths.

Table 10. Electron range for several accelerating voltages in silicon, calculated using Eqn. 10 [44].

keV	1	1.5	2	5	10	15	20	30
μm	0.032	0.062	0.101	0.466	1.48	2.92	4.72	9.29

4.2.2. Critical dimension metrology

Measurement of the critical, small-sized featured can be affected by various means, which are possible to divide in two categories: imprecision introduced by machine-related (or environmental) factors and by variations in the sample.

The first category includes environmental influences such as particle count contaminating the machine and sample, stray magnetic fields distorting the image, vibrations affecting the image quality as well as the measurement accuracy. Relatedly, machine maintenance is an important factor since accumulating contamination can lead to partial or total blockage of the beam path, build-up of charged particles can lead to deflection of the beam, etc. [44].

The second category concerns the changes in the sample under investigation. Especially non-conducting materials can trap the impinging electrons and become charged. At low electron energies, the secondary electron emission from the substrate surface is higher than the incident primary electrons; emission of negatively charged particles leads to positively charging of the sample. PEs with low energies are then deflected and attracted to this charged region, leading to widening of the feature size/line width [46]. At

increased energies, substrate begins to sink electrons, which eventually create a transverse electric field above the surface. Imaging of a sample leads to physical adsorption of the contaminants on the surface, called electron beam-induced deposition (EBID): high-energy PEs create BSEs and SEs, these break down the bonds of molecules present in the SEM chamber, and decomposed molecules deposit on the surface. EBID can manifest itself in the darkening/brightening of the imaged area: physical change of the surface entails contrast difference. When a transverse electric field is present, the contaminant atoms migrate under the influence of this field. Long or repetitive exposures/imaging of a certain area contributes to further deposition of contaminants and farther migration of them, which ends up in "moved edges" of a line or feature. The effect is called *carry-over* [46]. Moreover, materials sensitive to electrons, e.g. e-beam resist, additionally undergo degradation and even loss of material due to deposited energy especially by the SEs. This energy can cause bond-breakage, cross-linking, formation of shorter bonds, or excitation of the vibrational states, thereby producing heat. Such effects can result in shrinkage or swelling of the polymeric film, which makes the precise characterisation of the sample even more challenging.

In occasions where the sample remains unaltered structurally and chemically, inaccuracies may arise due to different intensities of the collected electrons from different regions of the sample. Figure 34 shows an idealised post (or cross-section of a line) with non-vertical sidewalls. As the beam scans the post, the intensity profile fluctuates: when electrons hit the post upper corner, the yield of SE1 and SE2 increases due to increase in the surface area that secondary electrons can escape the substrate (Figure 34(a): region of interest is coloured black). The signal increase can be described by an exponential function: $\sim e^{x/t}$, where t is the width [47]. Moving to the sidewall, the intensity profile obtained can be approximated by $\sim 1/\cos\phi$, where ϕ is the so-called surface tilt angle [48] (Figure 34(b)). As beam is incident on the bottom corner of the post, generated BSEs and SEs are absorbed by the sample, leading to a *shadowing effect*. However, SE2 created by the absorbed BSEs and escaping the material reduces this effect. The signal intensity profiles of these areas are provided in [49]. Illumination of the structure contour due to increased signal intensity is called *edge-blooming*. Figure 34(d) shows a HAR NanoBit with the intensity profile obtained from cross-section of a NanoBit handle. Edge-blooming is shows itself as spiking of the intensity level on grey-scale.

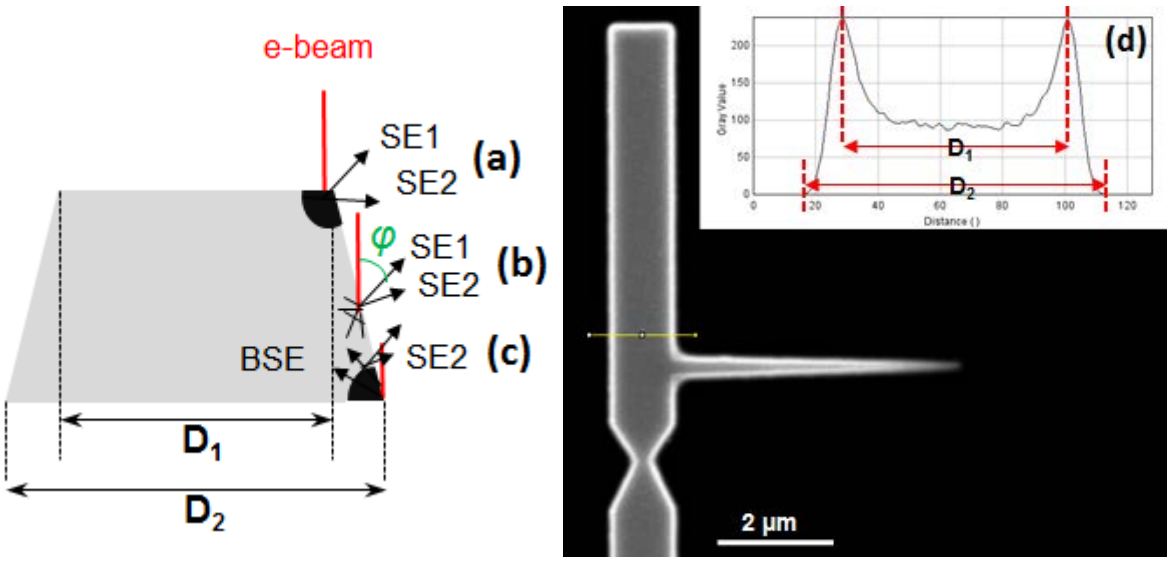

Figure 34 Representation of an idealised post with non-vertical sidewalls.

While characterising critical dimensions, it is important to signify the point/area of interest. The linewidth of a post, trench, or any similar structure for instance, can be defined by its top CD, bottom CD, or their average depending on what is actually being measured or significant for the following steps [44]; that is, by D_1, D_2, or $(D_1+D_2)/2$ in Figure 34. Thanks to high depth of focus of the SEM, both CDs can be viewed simultaneously in the case of a post. However, if D_1 is an undercut and D_2 is the top CD, operator needs to tilt the sample in order to visualise the undercut border. When structures with vertical sidewalls are under investigation on the other hand, this definition problem vanishes since $D_1 = D_2$. In characterisation of NanoBits D_1 and D_2 are determined by where the signal intensity reaches the maximum and minimum, respectively (as shown in Figure 34(d)), and feature sizes are referred further in the text by their respective CDs or positions (surface/top or bottom) instead of averaging of the two CDs, i.e. $(D_1+D_2)/2$.

For the assessment of critical parameters in section 4.1, Zeiss Supra 40 VP and LEO 1550 VP field emission SEMs at DTU Danchip were used. Both instruments provide highly flexible sample stages (tilt angles: -4° to 70° and 0° to 90°, respectively). The resolution limit of Zeiss Supra 40VP is 1 nm at 15 keV and 1.9 nm at 1 keV while the limit is ≤10 nm for LEO 1550 VP.

4.3. Assessment of the fabricated structures

4.3.1. Comparison to design specifications

The comparison of the critical parameters is done for microfabricated structured since FIB-milling is rather used for creation of prototypical structures and optimisation purposes.

The freestanding pSi membranes (with NanoBits and hybrid structures) and templates were finalised with a ~90% yield. The remainders of the membranes had small cracks or were fractured partially. These deformations are attributed to stress build-up during the consecutive oxide growth, pSi and Si_xN_y depositions. Figure 35 shows arrays of side-tip, HAR and cross NanoBits positioned at the NEMbrane edges of difference microchips. The dimensions of the critical parts are given in Table 11. The measurements show that the end-product features agree quite well with the design numbers. Some parts, however, were observed to have larger features than initially designed; the enlargement is only nominal (<1.5%) for all elements, which is not considered to hinder the functionality of these elements.

Table 11. The measured dimensions of the critical NanoBit parts.

Parameter	Length [nm]	Width [nm]
Handle	7037±28	1020±28
Break-point	-	159±14
Tip-NEMbrane distance	4570±90	-
Tip (HAR)	4990±20	258±10 (at base)

The utmost important feature of the NanoBit is the tip. OM and SEM inspection of the microchips showed that the tips remained intact and did not acquire any damage during fabrication or during post-fabrication manipulation (see Figure 35). Figure 35 also shows bright regions around the NanoBits, which cannot be attributed to edge-blooming. Magnified images of the tip clarified that the bright area is created by the tip

structure itself, hinting the widening of the tips. Detailed investigation is done using cross-shaped NanoBits. The tilted view of the NanoBits verified that the tip has wedged sidewalls (enlarging from surface to bottom) rather than vertical. Figure 36(a-c) provide the side-view of the tips and end-effectors with tip diameters plotted in the following.

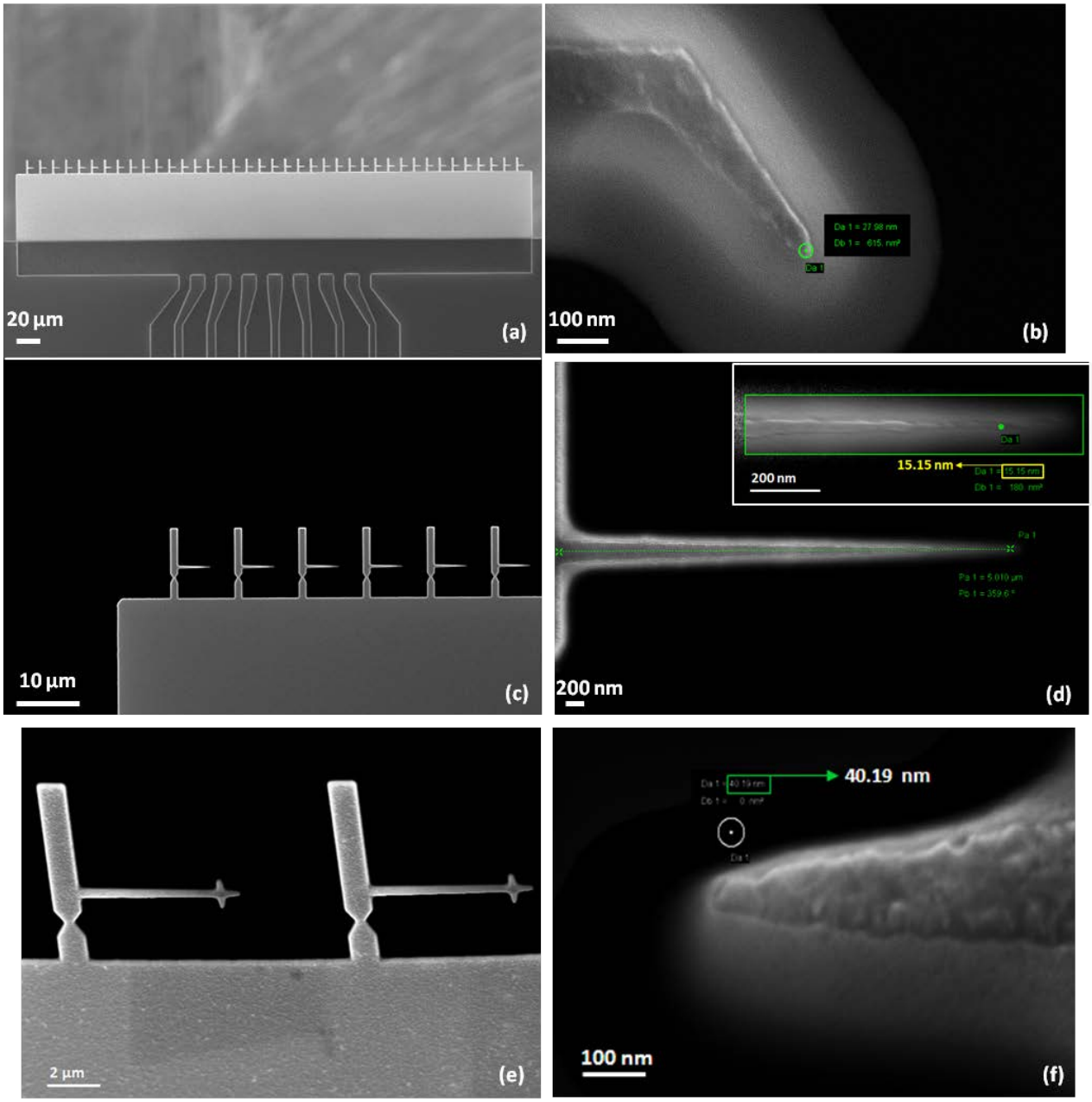

Figure 35 SEM micrographs of NanoBits. (a) Released pSi membrane with intact side-tipped NanoBits; (b) end-effector of a side-tip displayed in (a); (c) a group of released HAR NanoBits; (d) tip of one HAR NanoBit: length is preserved: 5 µm, Inset: tip-end diameter: 15 nm; (e) two cross-tipped NanoBits; (f) tip diameter at surface is 40 nm.

For tip diameter measurements, tools embedded to SEM software were used at high electron energies (5–8 keV). These measurements were then compared to cross-section intensity profiles across the measured area. Full diameter/width took into account borders where the intensity of the electron signal spiked for

both type of measurements and their average was taken as the actual diameter. The error bars in Figure 36(c) reflect the deviation from this average value.

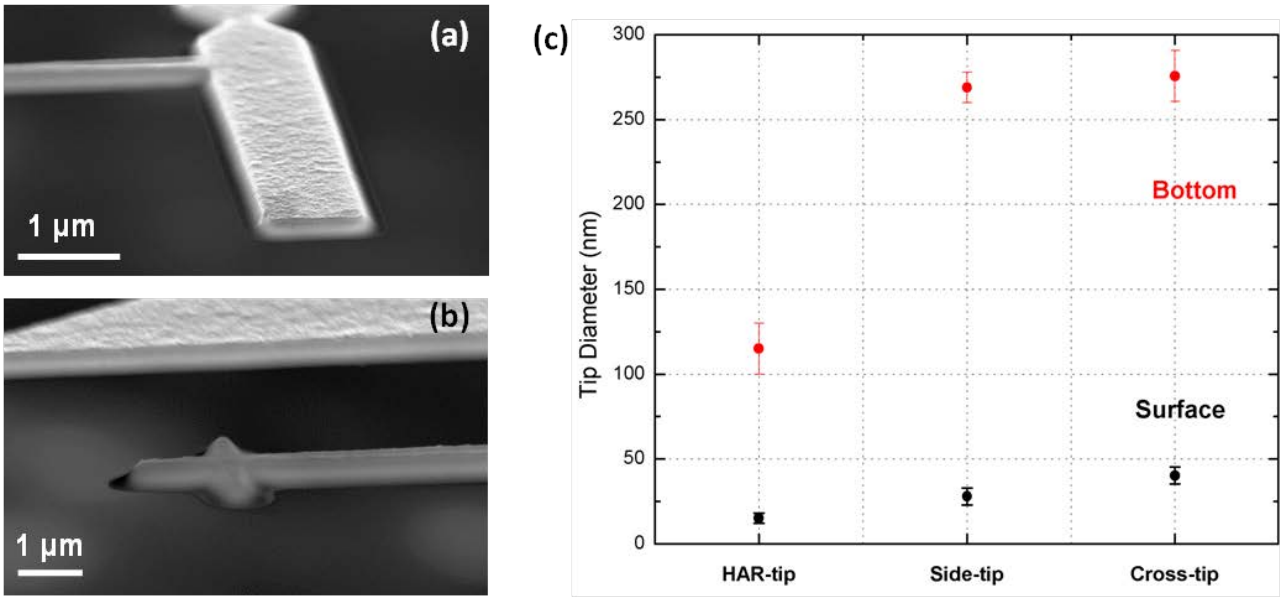

Figure 36 The sidewall profile of a cross-tip (a) handle and (b) end-effector. (c) Tip diameter at surface and bottom for three tip sorts. The width increase appears to be more significant for side- and cross-tips with HAR-tip diameter at bottom is only half of the other two.

The wedge profile complies with the initial expectations due to device layer thickness (200 nm). Likely, the NanoBits acquired this sidewall profile during the pattern transfer to pSi layer via RIE. More vertical sidewalls can be achieved through biasing the RIE process in favour of the physical etching, and possibly, decreasing the effect of chemical etching. To do this, one can simply increase the platen power, which should increase the directionality of the bombarding Ar ions. However, it should be noted that the density of the surface patterns and size of the openings play a prominent role in shaping the final sidewall angle, called "load effect". Therefore, the user should pursue the optimisation experiments with the identical structures. Unfortunately, such an approach requires definition of new set(s) of structures by EBL, i.e. commencement of a new, full-scale batch process. On the other hand, chemical- and/or physical-sharpening should prove cost-effective as well as time-efficient. Post-sharpening trials are discussed in Section 4.5.

4.3.2. Structural and mechanical testing

Freestanding NanoBits were tested to verify that they are structurally and mechanically acceptable. Acceptable structure denotes a high degree of correlation between the design and measurements of the outcome. Acceptable mechanical behaviour points out that a demonstration of successful manipulation and application of the NanoBits in a realistic manipulation scenario is the most relevant way for testing.

Structural testing

The advanced FIB milling strategies described in section 3.1 allow precise and prioritised transfer of the designed pattern to the silicon membranes, where the critical zones are milled in a way that results in the smallest possible amount of amorphisation and distortion, e.g. reduction of the effects of drift and

redeposition. With this state-of-the-art methodology the freestanding FIB-milled NanoBits are comparable to NanoBits made by EBL.

Structural properties of the NEMbranes and NanoBits were investigated by transmission electron microscope (TEM). In TEM, sample imaging is carried out via very highly energetic electrons (100–400 keV). The electrons penetrate the sample and interact with the matter. This interaction leads to scattering of electrons at different angles depending on the atomic structure of the substrate. The electrons that pass through and leave the material from the other side with various angles interfere with each other constructively or destructively. Resulting collective wave characteristic defines the diffraction pattern, which includes the information about the interacted sample. Thus, the diffraction patterns of materials allow interpretation of the atomic structure of the sample under investigation [50].

FIB milling of NanoBits produces a set of changes in the manufactured samples such as amorphisation of the irradiated areas. The Figure 37(a-b) shows the TEM image of the single crystal silicon NEMbrane and the corresponding diffraction pattern. The regular distribution of the bright spots (positive intensity of electron wave due to constructive interference) indicates the crystalline structure of the NEMbrane. Figure 37(c-d), the images of the very tip of a NanoBit and its diffraction pattern are given. The bright white disk of the diffraction pattern implies that the NanoBit tip is entirely amorphisised and possesses no significant ordered nanostructure.

EBL-defined NanoBits, on the other hand, were observed to retain their polycrystalline nanostructure: Figure 38(a-b) shows the NanoBit tip base (conjunction area of the very tip and handle) as an example, and the diffraction pattern obtained from the tip of the pSi NanoBit. Bright circles forming around the central spot indicate that the substrate has a somewhat crystalline nanostructure.

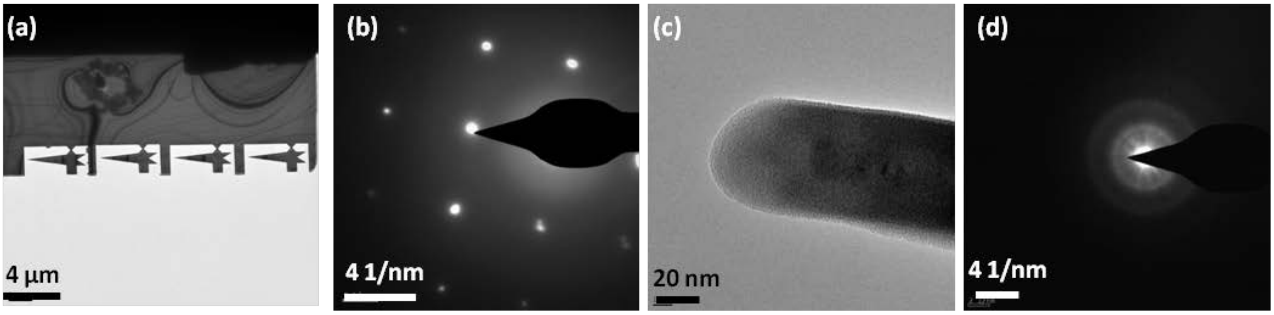

Figure 37. TEM images of FIB-fabricated NanoBits: (a) overview of a batch milled in a NEMbrane and (b) its diffraction pattern, proving the single crystal structure of NEMbrane; (c) image of the very tip shows the round shape after FIB milling; (d) selective area diffraction pattern of the very tip reveals completely amorphous structure.

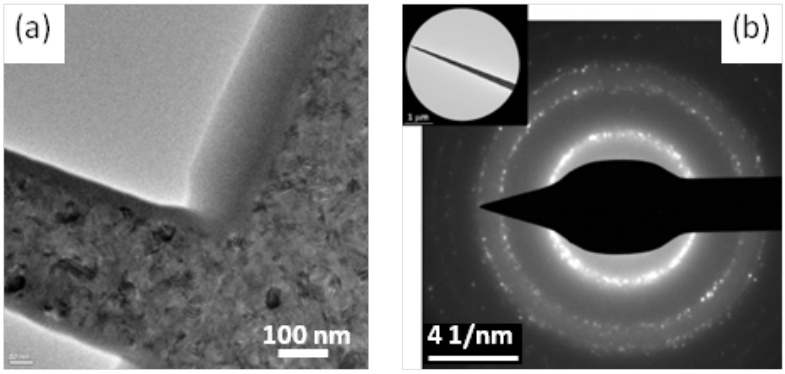

Figure 38 TEM observation of (a) microstructure of the pSi NanoBit, and diffraction pattern of the pSi tip (shown as inset).

Mechanical testing

Mechanical testing was done at OFFIS, where NanoBits were broken off and transferred to a cartridge by a pair of microtweezer, picked up by the AFM probe in a FIB-SEM dual beam system, and used for scanning high aspect ratio samples in forward and reverse directions in contact mode.

The first qualitative purpose was to force the NanoBit to contact the surficial structures and thereby test the bond between AFM probe and NanoBit. During these early experiments, the NanoBits were observed to fall off after a few scans, yet later SEM inspections showed no damage done to the NanoBits.

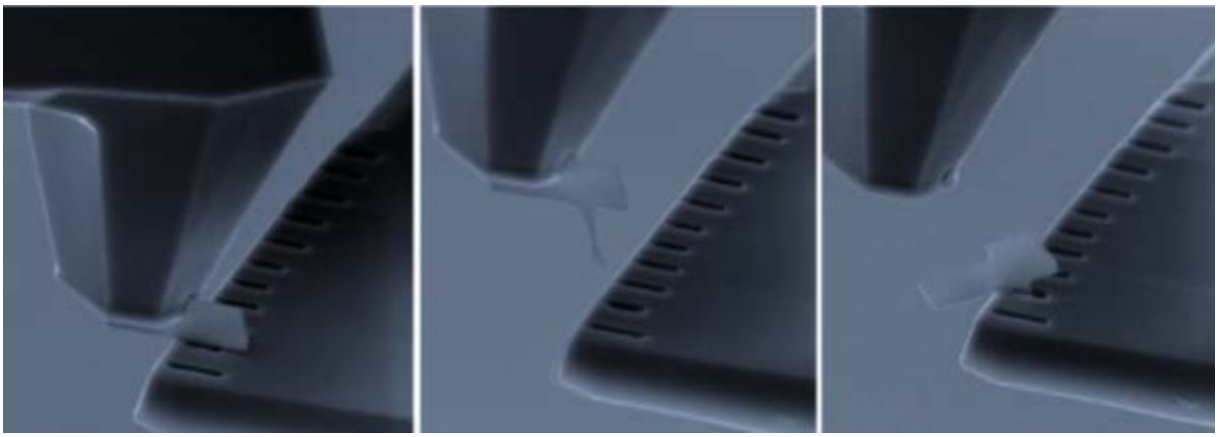

Figure 39 Picking up of a NanoBit from the cartridge cavity it was placed and placing back. (Left) The NanoBit is secured into the AFM probe slit. (Middle) NanoBit is picked up. (Right) NanoBit placed back into the cavity. During numerous trials, no damage was observed on the NanoBit.

Secondly, the cartridges played a crucial role in verifying the mechanical integrity of the NanoBits. A NanoBit inserted in a cartridge cavity (the cartridge cavities were opened at the freestanding end of a cantilever) was picked up by the AFM probe. During the pick-up cantilever deflection was measured and from the Hooke's Law, the force required to free the NanoBit from the cartridge was estimated. The Hooke's Law is given as

$$F = kx \tag{11}$$

where *k* is spring constant, *x* is displacement, and *F* is the applied force. With cantilever *k* = 7.4 N/m [51], a total of 50 µm deflection was observed, resulting in a force on the order of µN in vacuum conditions. It should be noted that during SEM observations, NanoBit and the cavity/slit bond becomes stronger due to electron beam-induced deposition (EBID) [52]. As a result, frictional and cohesive forces, as well, are suspected to act on the bodies along with van der Waals forces.

4.4. Focused ion beam vs. electron beam lithography

Development of smart milling strategies allowed achieving very small NanoBit tip diameters. While standard raster millings resulted in tip diameters in the range of hundred nanometers (140–400 nm), circular (or radial) and large-area-first (or proximity-to-edges) type of scans gave tip diameters <50 nm. The

sharpest tips were attained by using circular scan, where the critical points of connector, break-point and the very tip were introduced as input to the stream file; final tip diameters were <25 nm. Figure 40 shows the milling strategies, resultant NanoBits and the final tip diameters.

Apart from the very tip, the overall structure of the NanoBit is very significant. That is, the strategies producing the sharpest tips cannot be always be used. For instance, although the "circular scan with 3 points" gives almost the sharpest tip, the geometry of the NanoBit body is not very well defined: the tip should preferably have a tapered structure with straight edges. Similarly, the NanoBit realised by "circular scan with 1 point" is the sharpest tip but redeposited material is apparent on the handle and break-point; in this regard, "circular with backscan" provides a more appropriate NanoBit in overall quality.

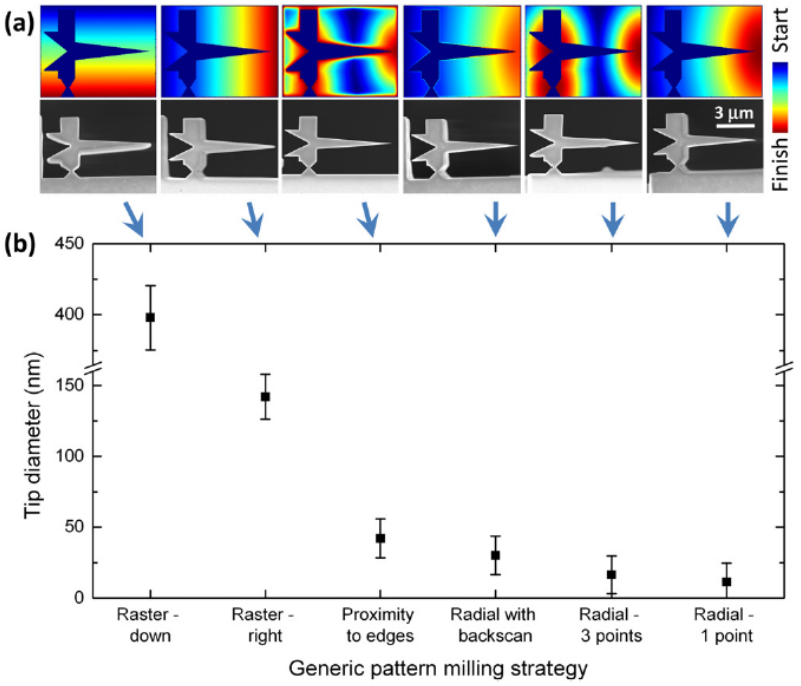

Figure 40 (a) Different single-pass milling strategies and SEM images of obtained structures. Colour coding corresponds to milling sequence: from dark blue to dark red. (b) Tip diameters achieved by the milling strategies. Measurements are made by SEM.

NanoBits defined by EBL can be argued to possess sharper tips and better-shaped critical points. However, this argument is restricted to the topside (surficial) dimension; along the thickness direction towards bottom, the NanoBits widen and fine dimensions degrade (see Figure 36). Since all three dimensions are essential for the performance of an SPM tip, FIB-milled NanoBits can be claimed to be better fitting for the purposes of AFM imaging.

NanoBits realised by EBL had high aspect ratios, AR = 20 (tip length divided by tip-base width considering the surface dimensions), as designed initially, which is highly suitable for deep trench topographies. With FIB milling, ultra high aspect ratios (AR = 45) were later achieved after iterative optimisations of the smart milling strategies (see Figure 41).

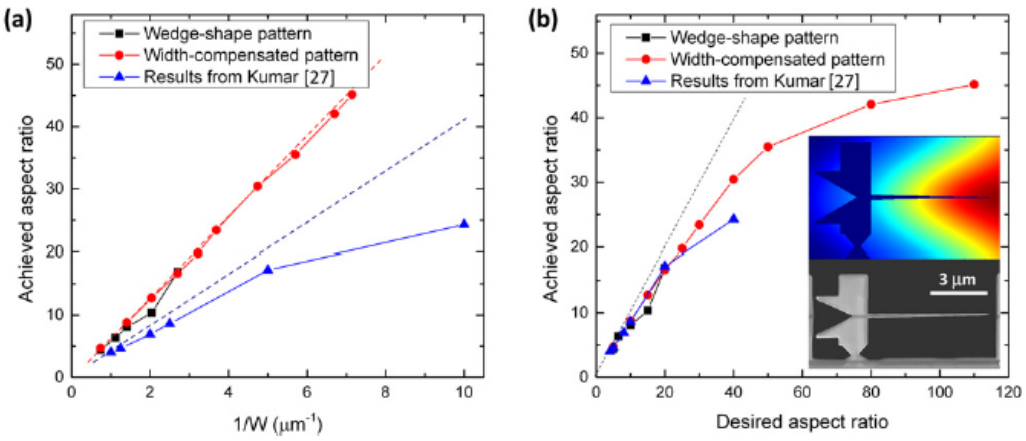

Figure 41 Obtained aspect ratios versus (a) the reciprocal width at the needle base and (b) the desired aspect ratio, comparing a straightforward wedge pattern and the width-compensated pattern, to the results of Kumar *et al.* [17] using electron beam lithography. The inset shows the used FIB milling strategy, with blue being milled first and red being milled last, with the corresponding SEM image of the finished NanoBits.

4.5. Sharpening

Here different approaches as post-processing sharpening methods for pSi NanoBits fabricated by EBL are described.

As there is no pSi-selective wet chemistry available, physical means of etching were pursued. These are

- ion beam etching (IBE),
- reactive ion etching (RIE), and
- focused ion beam (FIB) milling.

In the first two experiments, microchips of NanoBit arrays were turned upside down in order to etch the wider bottom part whilst protecting the finer top surface and tip. Figure 42 shows the top-view of the side-tipped and high aspect ratio (HAR)-tipped NanoBits. During FIB milling, NanoBits were sharpened by milling from the side.

4.5.1. Ion beam etching

IBE/IBSD Ionfab 300 of Oxford Instruments Plasma Technology is a powerful machine allowing highly physical etching. Etching is carried out by sputtering of target material via energetic Ar ions. For experimentation, single chips of side-tipped and HAR-tipped NanoBit arrays were used. Chips were turned upside down, glued to a carrier wafer by Crystalbond™[1], and introduced into the chamber. With the aim to thin the NanoBits by roughly 50 nm, Si etching was performed for 3 min with 400 V Ar^+ accelerating voltage and 1200 W RF plasma power. SEM images taken later showed no trace of effective etching (see Figure 43(a-b)). A longer (5 min) etching process followed with the same parameters, yet no obvious sharpening was observed. Mandatory Crystalbond™ usage might hinder exploitation of the full capability of the IBE:

[1] A thermoplastic polymer used as a temporary adhesive. (http://www.crystalbond.com/)

(having turned the chip upside down) only 200-nm-thick pSi NEMbrane may easily be covered by reflowed adhesive, which in return, could prevent Ar^+ ions to make physical contact with the target membrane.

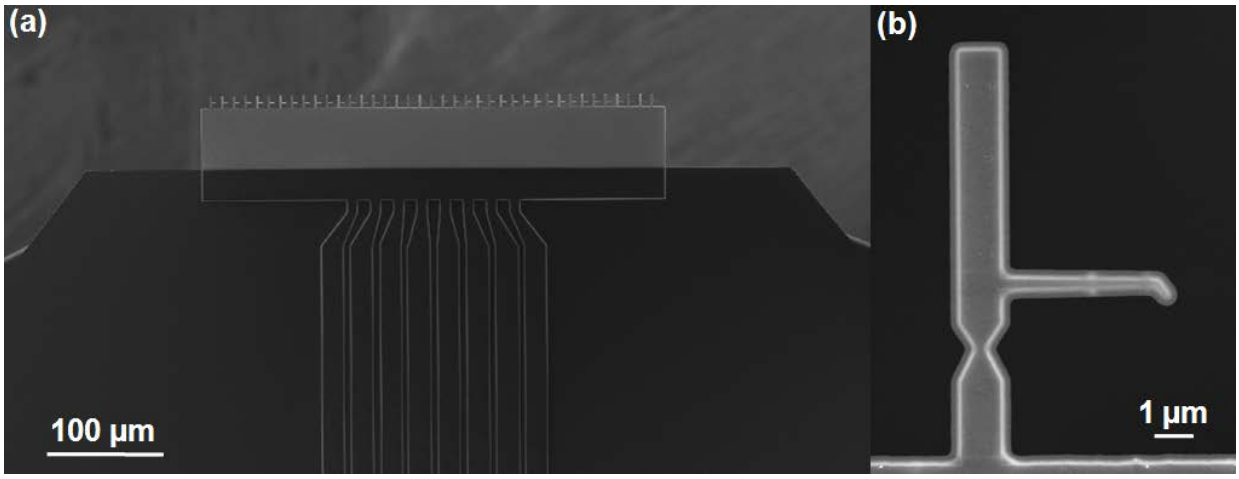

Figure 42 Released NanoBits: (a) an array of side-tipped NanoBits extending at the edge of a membrane; (b) magnified image of a single NanoBit: blurry contour around the NanoBit denotes widening of features from top to bottom (skirt-like), due to non-vertical etching. Illustrated side-tips on average had 28 nm tip diameter on top and larger than 400 nm at their bottom.

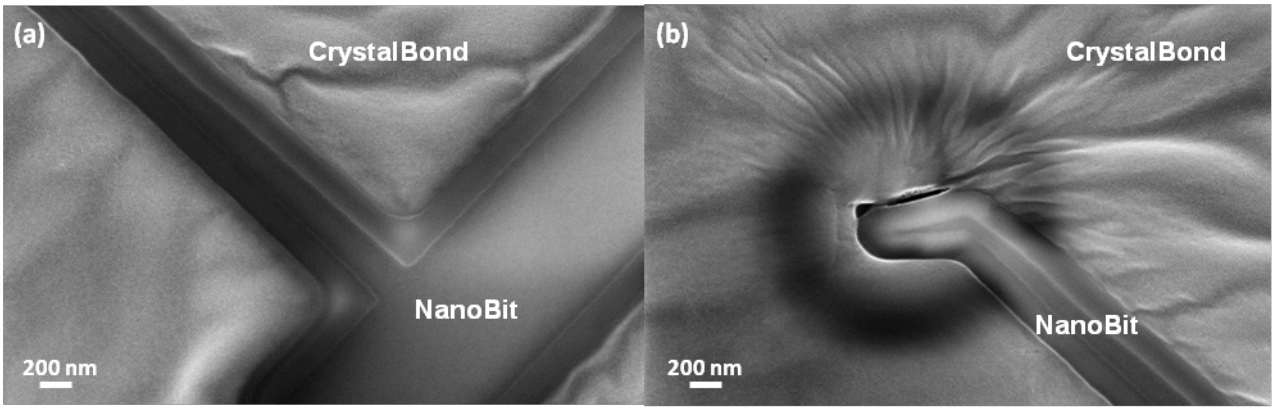

Figure 43 Reverted NanoBits glued to a carrier wafer via adhesive. Segmental NanoBit profiles shown after 3 min IBE: (a) intersection region of the NanoBit handle and the tip-base; (b) further along the tip with angled side-tip visible. Widened bottom part of the NanoBit remains unetched, suggesting that the adhesive material block the ion beam.

4.5.2. Reactive ion etching

Similar to IBE, two chips of HAR and side-tip NanoBits were extracted from the source wafer for sharpening trial. RIE2 (part of the STS Cluster System C004) was used for thinning. Targeting to etch 80–90 nm, the process was set to last 15 s under 80 mTorr pressure, 30 W RF power, with SF_6 and O_2 as chamber gases at room temperature. Processed structures are illustrated in Figure 44. Resultantly, tip sharpness enhanced along with the considerable narrowing of the tip bottoms (see Figure 44(c)). Measurement that was done on a HAR NanoBit revealed 14 nm of tip diameter (see Figure 44(f)). More importantly, there was no clear sign of the former wedged profile of the sidewalls (compare Figure 43 and Figure 44).

Longer exposures are assumed to result in even narrower and, in overall, sharper probing tips. However, close attention to and careful handling of the microchips are highly recommended, since (i) the level of gas concentrations in the process chamber affects the etching process directly, and (ii) ever-thinning NanoBits will become more vulnerable to damages/contact. Nevertheless, thinning and narrowing of tips would eventually result in NanoBits with higher aspect ratios that are more compatible with nanoscaled topographies. A clear advantage is the speed and batch compatibility of the process, allowing full wafers of NanoBits to be sharpened in a few minutes.

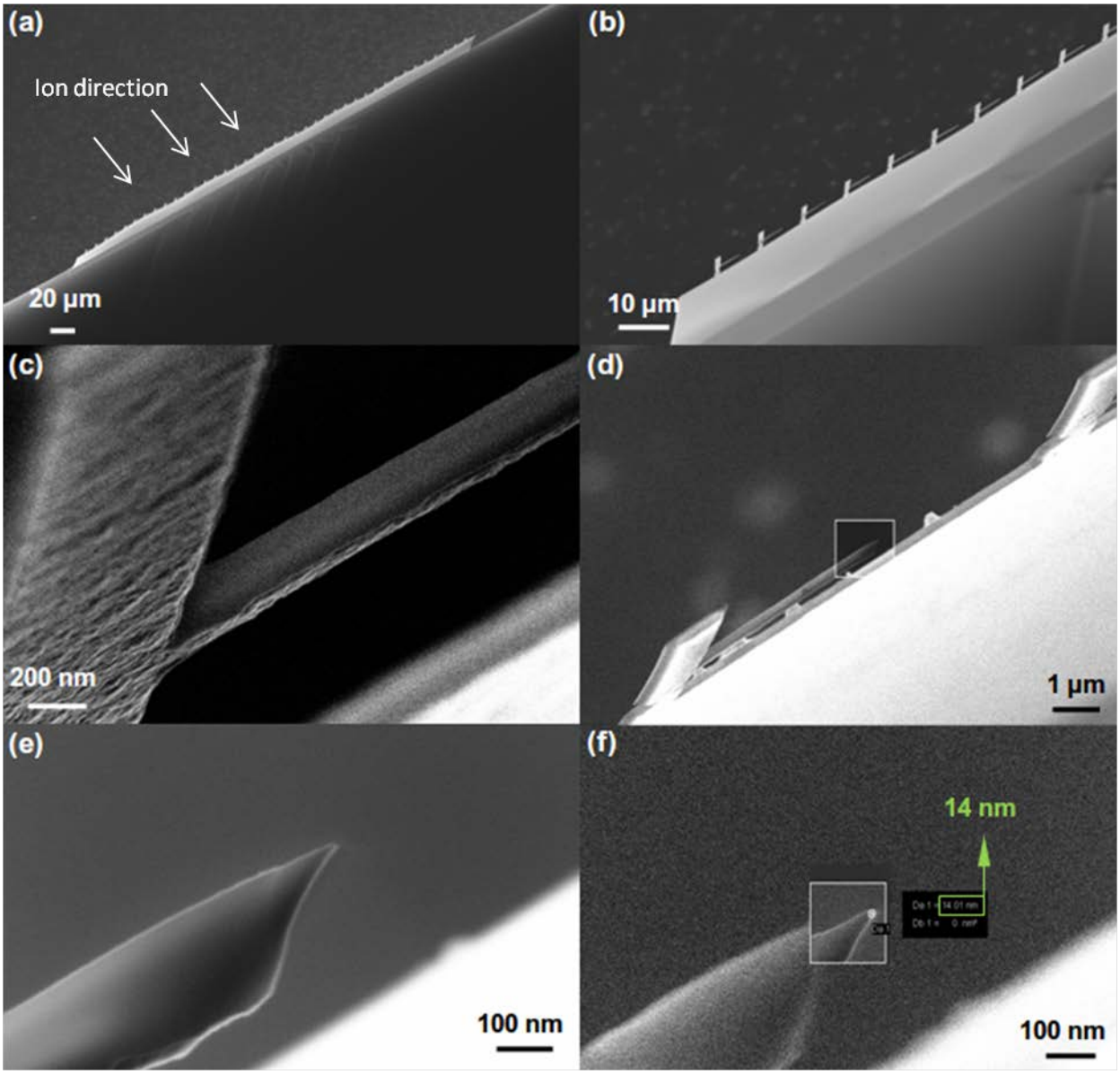

Figure 44 SEM investigation of a NanoBits array after 15 s exposure to reactive ion etching: (a) pSi membrane with the NanoBits; (b) magnified left-end of the membrane; (c) tip base-handle intersection of a NanoBits; in contrast to its previous profile, no sign of bottom-widening was spotted; *(d)* de-magnified image of the same NanoBits in (c) with the tip in focus; *(e–f)* focused tip magnified: the structure obviously does not possess any widening/blurry "skirt", and now has a sharper tip: 14 nm tip diameter. The specimen was positioned in right angle to the moving stage. Tilt angle: 22° towards the top surface of the membrane/NanoBits. Ions targeted the backside of the membrane.

4.5.3. Focused ion beam milling

Sharpening of the tips by FIB was investigated on hybrid NanoBits. Tip diameters ~40 nm and AR >10 can be achieved relatively quickly and easily (see Figure 45). To sharpen the structures, the smallest available beam diameter of 7 nm was applied for 5 min. Smaller diameters, however, proved difficult to obtain because substrate material tends to melt and shrink under the impact of Ga^+ ions. Compared to "smart milling" strategies used in FIB-fabrication of NanoBits, certain drawbacks emerge in the current picture, such as the necessity of manual pattern drawing, lessened control over the process, and the very tip's tendency to bending.

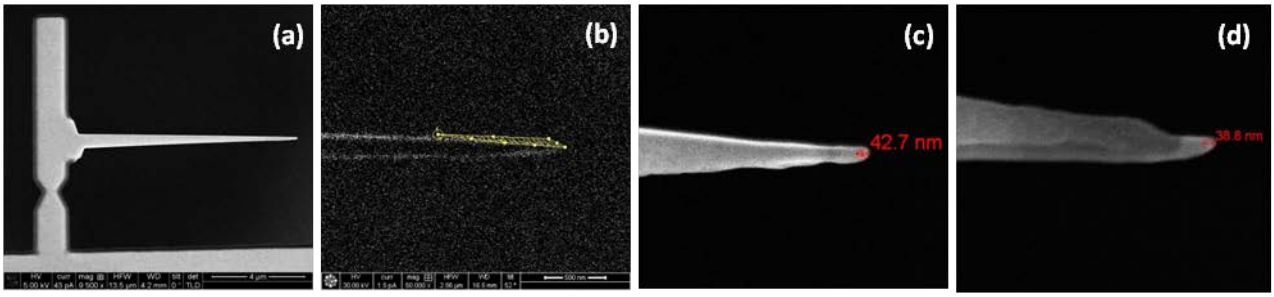

Figure 45 Sharpening of a hybrid NanoBit: (a) final shape of the NanoBit, (b) observation and milling by the scanning ion beam, (c) top-view of the tip, (d) 52° side-view of the tip.

4.6. Discussion and conclusions

From manipulation point of view, NanoBits stand as mechanically stable, easily accessible (e.g. by a microgripper) and collectable (well-defined break-point). In terms of processing, however, performing EBL in the beginning imposes considerable risks especially in terms of (i) resolution degradation during later treatments, and (ii) damaging/losing chips due to poor Si_xN_y quality. Instead, re-organising the fabrication flow to carry out EBL at an as late stage as possible should increase the chances of obtaining finely shaped structures. By this way, one would neither have to pay minute attention to whole process nor would jeopardise distorting the critical NanoBit dimensions realised through a costly EBL procedure.

The choice of 200-nm-thick pSi NEMbrane is based on the discussions made with OFFIS, following the early manipulation experimentation done to note and test the critical NanoBit elements. During this experiment Si NanoBits with 300 nm thickness had been used, and observed to be thick relative to the slit milled on plateau cantilever, which was obtained from NanoWorld (slit width at the surface ~250 nm). Then, the NanoBit had been *in situ* thinned down via exposure to FIB; expectedly, thicknesses below 250 nm worked as desired. Nevertheless, once thinned below 200 nm, NanoBits failed to preserve their structural integrity – bending, warping of the structures were monitored. Therefore, despite ≥200-nm-thickness necessity, such thickness imposes limitations with respect to the modern-day applications as very sharp tips will be difficult to achieve without post-process sharpening of the fabricated tips. While this is a fast and reliable process, it does impose another level of complexity. The use of single crystal silicon (scSi) instead of pSi is expected to provide stiffer structures and is possible with minimal adjustments of the process sequence; it is, however, difficult to obtain/buy single crystal SOI (silicon on insulator) wafers with a uniform thickness of the device layer in the range of 100 nm. The wafers are expensive and manufacturers are reluctant to

provide less than rather large batches. Fabrication of pSi is cheap, reliable and simple; thus, the objective to settle a simple process that can be run in a standard cleanroom is better met with pSi, which has almost as good mechanical properties.

Among the sharpening methods, wet anisotropic etch is not an option for pSi devices since the crystal structure simply is not globally anisotropic. In the use of single-crystalline Si (scSi), however, KOH etch could result in atomic sharpness owing to the high selectivity between <100> and <111>. As a physical etch alternative, IBE is not a suitable sharpening method (at the chip level) since it requires using Crystalbond™, which may render the physical etch improbable once it covers the whole target structure(s). This could be addressed by making an alternative fixation system, which unfortunately was not possible during the course of this study. On the other hand, RIE is a promising approach. With optimised etch timing, NanoBits with higher aspect ratios and sharper tips can be attained. A big advantage of the process is its batch-compatibility. In a similar fashion, FIB milling can prove useful in sharpening of the tips, although with a smaller throughput. Tip diameters ∼40 nm were observed as relatively easy to obtain; however, further processing drives the very tip to deform and bend. The small throughput of the method and the difficulty in automation makes this approach less relevant.

5 Out-of-plane Bending

The intervention of a microgripper increases the complexity of the procedure significantly, as was mentioned earlier. In this chapter the possibility of bending the NanoBits out of their lateral plane by inducing stress in the NEMbranes is considered. Ideally, the out-of-plane-bent NanoBits are assumed to allow the AFM cantilever itself to pick up the NanoBits, and thus to eliminate the need for microgrippers. The main aim is to bend the NanoBits by 90°, allowing a deflection window of ±10°, and to investigate the degree of level of control. 90°±10°-bent NanoBits can be fitted into the FIB-milled slit(s) on the plateau AFM probe.

Bending, folding and curving of thin, planar structures (i.e. membranes/NEMbranes) are used in numerous scenarios within micro- and nanofabrication [53]. Residual stress [30], capillary forces [29], magnetic forces [54], or stress formation due to chemical reaction [55] can be used to achieve a finite curvature, and thus create three-dimensional shapes, sometimes referred to as nano-origami [53]. To bend the nanobits, NanoBit-like structures and NEMbranes two methods were employed: out-of-plane bending by focused ion beam irradiation and by stress build-up in bilayer systems.

5.1. Stress-induced bending of structures

Stress is a physical quantity that expresses the internal forces that neighbouring particles of a continuous material exert on each other, and is defined as the force (*F*) applied per unit area (*A*)of a particle, or in macroscopic scale, a surface.

$$\sigma = \frac{F}{A} \tag{12}$$

Stress can be caused by various external and internal means. Among external agents, gravity, electromagnetic forces, pressure, friction and changes in the temperature can be counted. Internal factors include the changes in the microstructure of the material, such as phase change, polarisation, grain boundaries, defect annihilation/creation, and so forth. If the force acting on the surface applies an extending load, the stress is called tensile; however, if the force acts in the opposite direction inducing compression, the stress is compressive. Figure 46 provides a representation of stress.

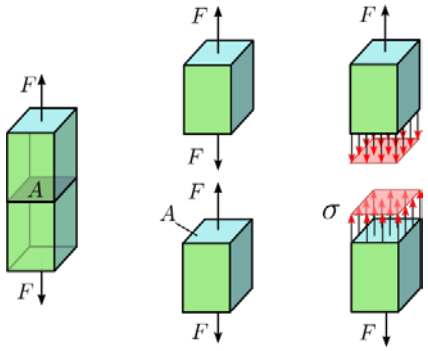

Figure 46 Stress is the total force exerted on a surface. The extension force applied to the surface normal creates tensile stress.

As an object is pulled or pushed in one direction, the distance between the material molecules increases or decreases, and therefore the object elongates or shrinks under the applied force, respectively. The induced change in dimensions proportional to initial dimensions is called strain, ε, and the rate of change of object dimensions is determined by the material property called modulus of elasticity or Young's modulus, E.

$$\sigma_i = E\varepsilon_i \tag{13}$$

Eqn. 13 is the linear elasticity theory, giving the total stress in closed form for isotropic materials, where the index i denotes the axis component. Deformation of the shape of a structure in one direction entails deformations in the other two directions as well. Figure 47 shows the deformation of a square-shaped body in the x-axis where the position $u_x(x)$ shifts to $u_x(x+\Delta x)$. The material elongates by $\Delta L_x = u_x(x+\Delta x) - u_x(x)$, and therefore the strain in x-axis is

$$\varepsilon_x = \frac{u_x(x+\Delta x)-u_x(x)}{\Delta x} = -\nu\varepsilon_y, \tag{14}$$

where ν is the Poisson's ratio and signifies the proportion of strain in the transverse direction (y-axis) to the strain in the axial direction (x-axis), thus relating the deformations in axes by

$$\nu = -\frac{\varepsilon_y}{\varepsilon_x}. \tag{15}$$

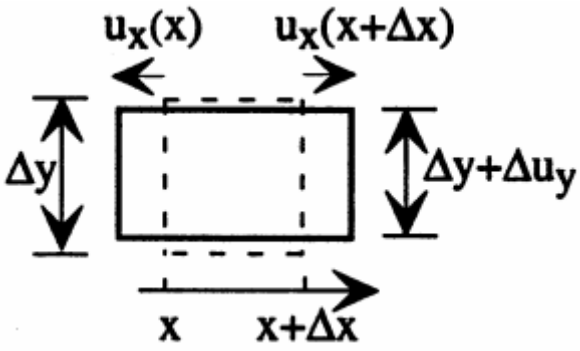

Figure 47 As a load is applied to the square object (inscribed by the dashed line), the object undergoes deformation (solid line).

Then, for a 3-dimensional object, the deformed dimensions can be written as

$$\Delta x \rightarrow \Delta x(1+\varepsilon_x),$$

$$\Delta y \rightarrow \Delta y(1 - \nu\varepsilon_x),$$

$$\Delta z \rightarrow \Delta z(1 - \nu\varepsilon_x), \tag{16}$$

And combining Eqn. 16 with Eqn. 13 by symmetry, the strains can be written as

$$\varepsilon_x = \frac{1}{E}\left[\sigma_x - \nu\left(\sigma_y + \sigma_z\right)\right],$$

$$\varepsilon_y = \frac{1}{E}\left[\sigma_y - \nu(\sigma_z + \sigma_x)\right],$$

$$\varepsilon_z = \frac{1}{E}\left[\sigma_z - \nu\left(\sigma_x + \sigma_y\right)\right]. \tag{17}$$

In the special case of creating stress by thin film deposition onto a substrate, the stresses are adopted as in-plane; that is, $\sigma_z = 0$. Because in the isotropic materials the in-plane stresses are equal in all directions ($\sigma_x = \sigma_y = \sigma$, hence $\varepsilon_x = \varepsilon_y = \varepsilon$), the equalities in Eqn. 17 can be reduced to

$$\varepsilon = \frac{\sigma}{E}(1 - \nu), \tag{18}$$

or

$$\sigma = \left(\frac{E}{1-\nu}\right)\varepsilon, \tag{19}$$

where the factor $E/(1-\nu)$is called the biaxial modulus and will be denoted by E' further in the text. For isotropic materials, E and ν are sufficient to describe the elastic behaviour of a system under stress [30]. Anisotropic materials, however, as the naming suggests, do not respond to acting forces equally in different crystal orientations. In a broader and more general view, the elasticity modulus of the material is defined by the elastic stiffness constants, c_{ij}, or the elastic compliance constants, s_{ij}, which, in the generalised Hooke's law of elasticity are

$$\sigma_i = c_{ij}\varepsilon_j, \qquad \varepsilon_i = s_{ij}\sigma_j. \tag{20}$$

Note that the components in Eqn. 20 are tensors, and opens form of the stress, compliance, and strain tensors for the anisotropic materials can be given as [30, 56]

$$\begin{pmatrix} \varepsilon_{11} \\ \varepsilon_{22} \\ \varepsilon_{33} \\ 2\varepsilon_{23} \\ 2\varepsilon_{13} \\ 2\varepsilon_{12} \end{pmatrix} = \begin{pmatrix} s_{11} & s_{12} & s_{12} & 0 & 0 & 0 \\ s_{12} & s_{11} & s_{12} & 0 & 0 & 0 \\ s_{12} & s_{12} & s_{11} & 0 & 0 & 0 \\ 0 & 0 & 0 & s_{44} & 0 & 0 \\ 0 & 0 & 0 & 0 & s_{44} & 0 \\ 0 & 0 & 0 & 0 & 0 & s_{44} \end{pmatrix} \begin{pmatrix} \sigma_{11} \\ \sigma_{22} \\ \sigma_{33} \\ \sigma_{23} \\ \sigma_{13} \\ \sigma_{12} \end{pmatrix}. \tag{21}$$

The tensor notation for the stiffness constants is the inverse of Eqn. 21. For instance, biaxial modulus of elasticity for Si in (001) direction is given as $E'(001) = 1/(s_{11}+s_{12})$, and in (111) it is $E'(111) = 6/(4s_{11}+8s_{12}+s_{44})$. The calculations of the stiffness and compliance constants for Si are published in [57-58], the resultant biaxial moduli of Si were found as $E'(001)$ = 180.3 GPa and E'(111) = 229.1 GPa [56].

Since a complete analysis of stress types and evolution is beyond the scope of this study, in the following the text is concentrated onto the theory and evaluation of the one of the most common methods used to induce stress: thin film deposition.

When a stressed metal film is brought in contact with a stress-free substrate, the bending occurs resulting in curving of the total body by a finite curvature. The first attempt to formulate the curvature due to residual stress in a thin film deposited on a thick substrate was made by G. G. Stoney [59]. To assess the problem, a film with an isotropic effective force f acting on it is assumed, where f is in the units of force/length. This effective force strains the film membrane to match the size of the substrate (see Figure 48). As the thin film contacts the substrate and weld together, the stress (or the force) relaxes. During this relaxation, the substrate undergoes deformation and bends.

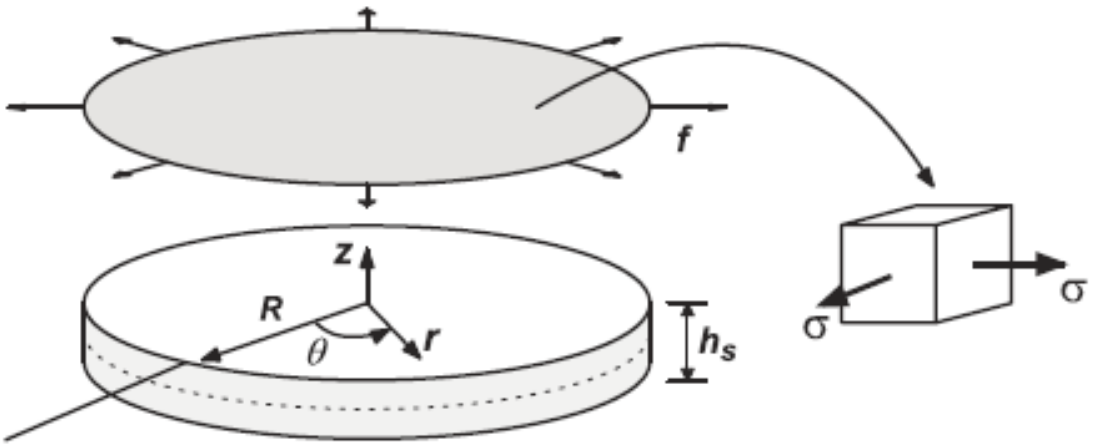

Figure 48 The thin film under force *f* is put in contact with the substrate with thickness h_s. The stress components in the film are assumed identical owing to isotropy of the material [30].

The analysis of the above problem assumes the following:

(i) the normal stress component $\sigma_{zz} = 0$,
(ii) displacement of all components are very small, and linear theory of elasticity can be used,
(iii) the film material properties do not influence the overall elastic stiffness,
(iv) the deformation is symmetric: $\varepsilon_{r\vartheta} = 0$,
(v) the curvature of the system, κ (inverse of radius of curvature, ρ), is uniform, and
(vi) the in-plane strain is uniform and isotropic: $\varepsilon_{rr}(r,0) = \varepsilon_{\vartheta\vartheta}(r,0) = \varepsilon_0$.

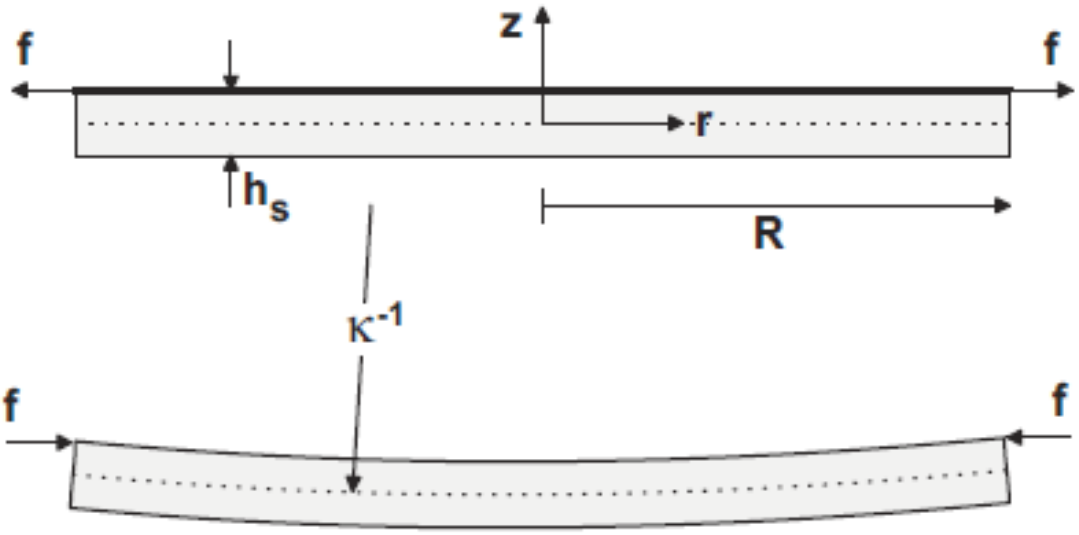

Figure 49 The sketch of the bilayer system as the film and substrate are in contact (top) and bent structure as a result of stress relaxation (bottom) [30].

As a result of translational invariance and symmetry of the system, the deformed shape of the midplane at $h_s/2$ is spherical, provided that the deformation is small and material is isotropic. Then, the strain energy density at any point of the substrate can be expressed as

$$U(r,z) = \frac{\mu_s}{1-\nu_s}\left(\varepsilon_{rr}^2 + \varepsilon_{\vartheta\vartheta}^2 + 2\nu_s\varepsilon_{rr}\varepsilon_{\vartheta\vartheta}\right), \tag{22}$$

where $\mu_s = ½E_s/(1+\nu_s)$ is the shear modulus, and the elastic strains in Eqn. 22 can be expressed separately as functions of radial and out-of-plane displacement, $u(r)$ and $w(r)$, respectively:

$$\varepsilon_{rr}(r,z) = \dot{u}(r) - z\ddot{w}(r), \qquad \varepsilon_{\vartheta\vartheta}(r,z) = \frac{u(r)}{r} - \frac{z\dot{w}(r)}{r}. \tag{23}$$

For small deflections and uncoupled radial and out-of-plane deformations, the minimisation of potential energy dictates the displacement of the midplane as

$$u(r) = \varepsilon_0 r, \qquad w(r) = \frac{1}{2}\kappa r^2. \tag{24}$$

As the stress (or force f) relaxed and the bilayer system deformed, the in-plane stresses become $\varepsilon_{rr} = \varepsilon_{\vartheta\vartheta} = \varepsilon_0 - \kappa z$, where ε_0 is the extensional strain of the midplane and κz denotes the strain component due to bending at any point z of the structure. The total strain energy density is then $U(r,z) = E_s'(\varepsilon_0 - \kappa z)$, and the total potential energy can be derived by integration $U(r,z)$ along the radial axis and thickness of the system:

$$V(\varepsilon_0,\kappa) = 2\pi\int_0^R\int_{-\frac{h_s}{2}}^{\frac{h_s}{2}} U(r,z)rdrdz + 2\pi f u_r\left(R,\frac{h_s}{2}\right)R$$

$$= \pi R^2 E_s' h_s\left(\varepsilon_0^2 + \tfrac{1}{12}\kappa^2 h_s^2\right) + 2\pi R^2 f\left(\varepsilon_0 - \tfrac{1}{2}\kappa h_s\right). \tag{25}$$

Equilibrium midplane deformation is attained when the conditions $\partial V/\partial \varepsilon_0 = 0$ and $\partial V/\partial \kappa = 0$ are met. Then it follows from Eqn. 25 that

$$\varepsilon_0 = -\frac{f}{E_s' h_s}, \tag{26}$$

and

$$\kappa = \frac{6f}{E_s' h_s^2}. \tag{27}$$

If the film stress is tensile, the sign of f is positive and the curvature of the substrate surface is concave, or if the film is under compressive stress, f has a negative value and the curvature is convex. Denoting the film thickness with h_f, the stress in the film can be expressed as $\sigma = f/h_f$, and combining with Eqn. 27, the curvature as a function of film stress, or vice versa, can be formulated by

$$\kappa = \frac{6\sigma h_f}{E_s' h_s^2}, \qquad \text{or} \qquad \sigma = \frac{E_s' h_s^2}{6\rho h_f}. \tag{28}$$

Eqn. 28 is the infamous Stoney equation, has become a cornerstone since it relates the stress in the thin film to the resultant curvature of the system. Over the years, Stoney equation has been continually analysed and modified [30, 60-63] since, above all, it neglects the film material properties as well as the film thickness. Tolerating a maximum error of 10%, Eqn. 28 is applicable only for film thicknesses below one tenth of the substrate thickness: $t_f \leq 0.1 t_s$ [61].

Aiming to characterise the degree of bending of the NanoBit (NEMbranes) and for the sake of controllability of this degree, it is crucial to integrate the film thickness, its comparable thickness to the NEMbrane thickness and its properties into Eqn. 28. Taking into account the non-negligible film thickness and film properties, L. B. Freund [64] published a modified version of Stoney's equation. In this case, the strain energy density of the system is defined by considering the strain energy densities of both substrate and the film:

$$U(r,z) = \begin{cases} E_s'(\varepsilon_0 - \kappa z)^2 & for \quad -\frac{1}{2}h_s < z < \frac{1}{2}h_s, \\ E_f'(\varepsilon_0 - \kappa z + \varepsilon_m)^2 & for \quad \frac{1}{2}h_s < z < \frac{1}{2}h_s + h_f, \end{cases} \tag{29}$$

Where ε_m is the elastic mismatch strain in the film and defined by $\varepsilon_m = \sigma/E_f'$. The total potential energy then becomes

$$V(\varepsilon_0, \kappa) = 2\pi \int_0^R \int_{-\frac{1}{2}h_s}^{\frac{1}{2}h_s + h_f} U(r,z) r dr dz. \tag{30}$$

Meeting the condition $\partial V/\partial \kappa = 0$ as above, the curvature is found to be

$$\kappa = \left(1 + \frac{h_f}{h_s}\right) \frac{6\varepsilon_m h_f E_f'}{h_s^2 E_s'} \left[1 + 4\frac{h_f E_f'}{h_s E_s'} + 6\frac{h_f^2 E_f'}{h_s^2 E_s'} + 4\frac{h_f^3 E_f'}{h_s^3 E_s'} + \frac{h_f^4 {E_f'}^2}{h_s^4 {E_s'}^2}\right]^{-1}. \tag{31}$$

At this point, it is reasonable to distinguish the stress types based on the terms and notations used further in the text, specific to the stress formed by thin film deposition. The total stress is a combination of external stress (σ_{ext}), intrinsic stress (σ_{int}) and thermal stress (σ_{th}). In the case of film deposition via electron beam

evaporation of metal films, an electron beam melts a solid metal block by irradiation. Highly energetic metal atoms and molecules then leave the molt and deposit on the substrate, which is located virtually normal to the molten metal with surfaces facing each other. Following this type of deposition, σ_{ext}, such as gravitation and electromagnetic fields, is assumed to be negligible. σ_{int} is categorised as the stress forming during the film deposition due to internal changes and interactions in the metal film, and is sometimes called growth stress. σ_{th} denotes the stress that forms, vanishes, increases, or decreases upon any change in the temperature. The physical mechanisms creating a substrate curvature were hitherto analysed mechanically based on mechanical extension strain, ε_m. Below, the thermal strain induced by changes in the thermal conditions is differentiated from ε_m and is denoted by ε_{th}. When a substrate is at a different temperature than the deposition temperature, this difference induces σ_{th}, which causes (or contributes) to bending of the substrate as a result of different thermal expansion coefficients (TECs) of film and substrate materials. Thermal stress induced by straining of the substrate is given by

$$\sigma_{th} = E_f' \varepsilon_{th} = E_f' (\alpha_f - \alpha_s)(T_i - T_f), \tag{32}$$

where E_f' is the biaxial modulus of film, α_f and α_s are TECs of film and substrate, respectively, T_i is the substrate (initial) temperature during deposition, and T_f is the (final) room temperature (RT). Assuming that the metal film has a larger TEC than that of the substrate ($\alpha_f > \alpha_s$) and deposition takes place at a temperature higher than the RT ($T_i > T_f$), a positive thermal (i.e. tensile) stress is created upon cooling of the substrate. Tensile stress formation is common to almost all metal films [31]. As the σth relaxes, owing to $\alpha_f > \alpha_s$, the film retracts more strongly than the substrate, and thus bending occurs. TECs of commonly used metals are given in Table 12 at a presumed deposition temperature of 40°C.

Table 12 Themal properties of some of the common metals [31].

Material	Melting temperature (T_m) [K]	T/T_m	TEC (α) $\times 10^{-6}$ [K^{-1}]
Al	933	0.34	23.9
Sb	903	0.35	9
Cr	2148	0.15	6.2
Cu	1356	0.23	16.5
Au	1336	0.23	16.2
Fe	1807	0.17	11.7
Pb	598	0.53	29.3
Ni	1726	0.18	13.3
W	3683	0.08	4.3

TEC is a material property and is a function of temperature. Therefore, when calculating the thermal stress, the full function needs to be adopted; or, in the case of either small variation of α and/or T, the average values can be used for simplicity. TECs of various materials used as film or substrate in thin film applications are tabulated in [30]. In Table 13, TECs of the materials of interest (Ni and Si) that were used in bending experiments for different temperatures are given.

Table 13 Thermal expansion coefficients of nickel and silicon for 300–1473 K.

T [K]	$\alpha_{Ni} \times 10^{-6}$ [K^{-1}]	$\alpha_{Si} \times 10^{-6}$ [K^{-1}]
300	12.89	2.63
400	14.17	3.27
500	15.35	3.61
600	16.96	3.81
700	16.48	3.94
863	17.36	4.12
973	18.27	4.29
1073	19.15	
1100		4.38
1173	20.10	
1200		4.46
1273	21.07	
1300		4.56
1373	22.11	
1473	23.19	

In Table 12 the proportion T/T_m is given. According to [31, 65], this ratio determines the proportional magnitude of the σ_{int} and σ_{th} acting on the substrate. It is found that film materials with high melting temperature, or low T/T_m (≤0.25-0.3), are dominated by the intrinsic stresses. Metals with low T_m, or high T/T_m (exceeding 0.25-0.3), diffusion processes are claimed to be in effect, promoting recovery and recrystallization of the internal structure of the film, which eventually reduces the total internal stress. Figure 50 shows variation of the total internal stress as a function of T/T_m, where a linear increase of σ_{th} is assumed; however, including higher order T-dependent terms in α_f, this increase can show variation.

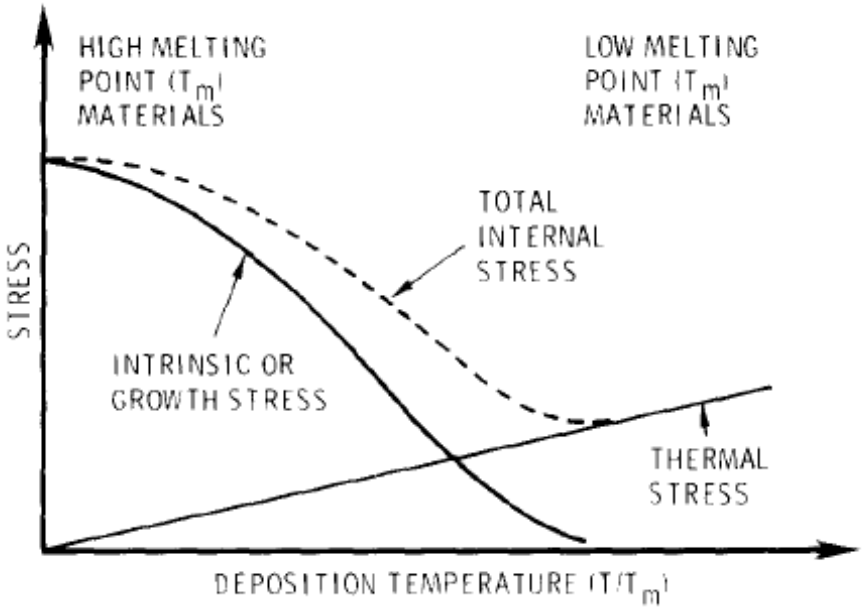

Figure 50 Schematic representation of the stresses in a deposited film for varying T/T_m [31].

5.2 Out-of-plane bending by FIB irradiation

FIB milling leads to several material changes, which can potentially lead to stress and deformation effects [66-67], including loss of material, redeposition and amorphisation. Material loss has been shown to create a characteristic bending of thin structures (<90 nm), because the material loss leads to a tensile stress on the exposed surface and thus bending towards the beam [68-69]. For 100 nm membranes, however, the ions deposited on the substrate surface can produce compressive stress and bend the membrane in the opposite direction under the same conditions [68].

The structures were fabricated from 100 nm and 200 nm silicon-rich low-stress silicon nitride (SiN_x) DuraSiN membranes for TEM. The membranes were covered with a 10 nm Au layer to avoid electrical charging during FIB milling. The definition of in-plane shapes such as Si_xN_y cantilevers and NanoBits was carried out with a FEI Helios NanoLab FIB/SEM system using a 30 kV 100 pA Ga ion beam using the smart milling strategies detailed above.

Figure 51 shows low-stress Si_xN_y membranes with a thickness of 100 nm and 200 nm that have been exposed to doses in the range of 5–850 pC/µm^2 at a current of 70 pA. For both thicknesses the onset of bending occurred abruptly at a certain dose, leading to a rapid but consistent transition to the stable 90° angle.

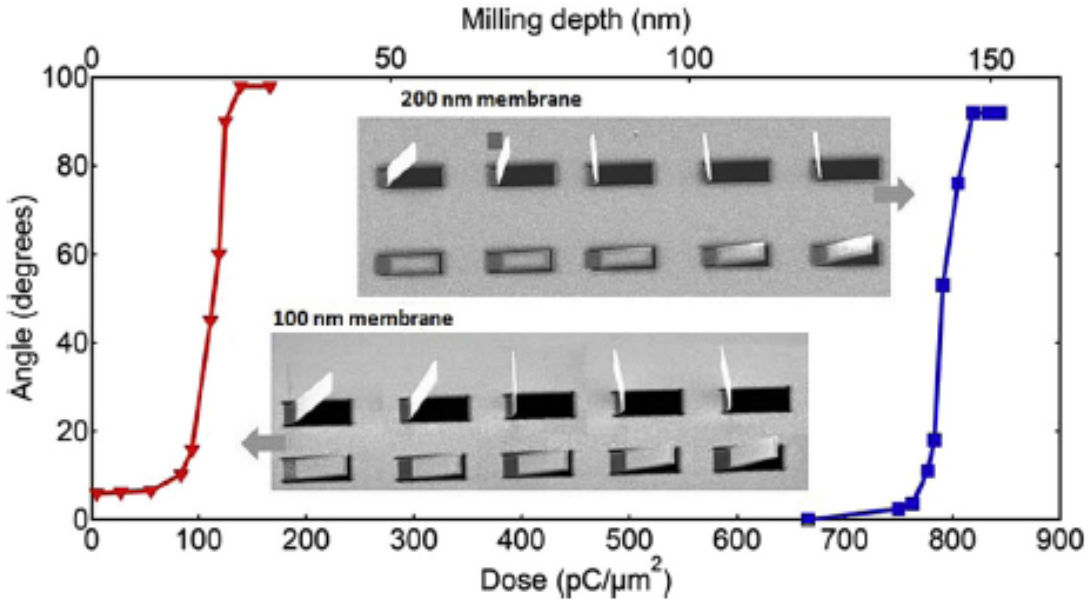

Figure 51 Bending to a roughly 90° angle for 100 nm (red triangles) and 200 nm (blue squares) Si_xN_y low-stress NEMbranes. The exposed region at the base of the stripe is 1 µm x 2 µm. Tilt angle: 52°.

The milling depth is calculated considering the sputter yield for Si_xN_y, estimated to be 0.18 µm^3/nC. The difference in dose required for the onset is roughly corresponding to the extra dose required to mill 100 nm of excess material from the 200 nm membrane, compared to the 100 nm membrane. At high doses the angles tend to overshoot, resulting in angles between 90° and 100°. Bending of thin cantilevers starts as soon as residual thickness is less than 80–90 nm. This value is comparable to the size of ion penetration depth in the target (Figure 52). For 30 kV Ga ions impinging on a Si_xN_y target, the penetration depth was

~45 nm, which depends on the composition of Si_xN_y. SRIM calculations [70] revealed that the composition of the Si_xN_y NEMbrane was quite similar to stoichiometric nitride, Si_3N_4.

A number of mechanisms can explain formation of stress in the thin NEMbrane:

(i) local heating of the NEMbrane surface due to FIB exposure can lead the hotter molecules to diffuse to the colder bottom, which may result in local swelling of the NEMbrane bottom;
(ii) sputtering of atoms from the surface gives rise to material loss and depletion of substance at the surface can cause the material to shrink;
(iii) the defects generated by FIB milling can enhance the rate of migration and diffusion of atoms/molecules;
(iv) a thin layer of (hot) metallic film (Ga) forming on top of SixNy can lead to creation of a bimorph structure.

All of these effects lead to stress formation: tensile on top and compressive on the bottom surface, thus bending cantilever upwards. Such observed bending is controllable by the value of FIB exposure dose.

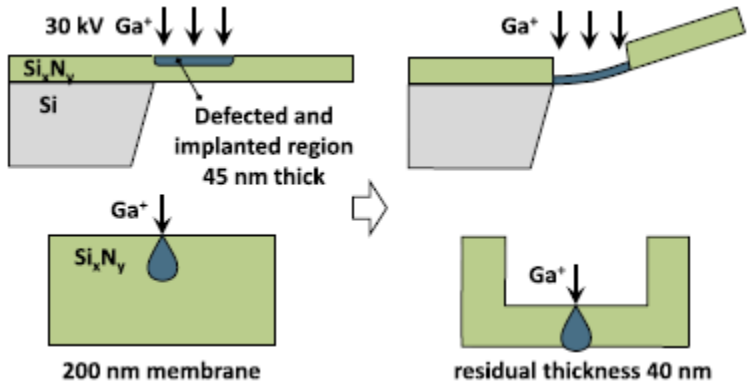

Figure 52 Bending mechanism of the FIB-irradiated cantilevers in the beginning of irradiation (left) and during bending (right). Ion interaction volume inside the material is shown comparing to the membrane thickness.

In rare cases, with 100 nm Si_xN_y NEMbranes, downward bending of the irradiated structures was also observed. This can be explained by formation of a compressive stress around the substrate surface. This compressive stress most likely stems from Ga ion implantation in the top layer as was reported in [68], which leads to the conclusion that upward OOP bending is driven mainly by the material ablation and thinning of the substrate material (<90 nm) whereas the downward bending is observed possibly when the compressive stress created by the implanted Ga ions dominate the mechanical behaviour of the NEMbrane.

Realistic NanoBits were realised by FIB milling the NanoBit structure on Si_xN_y NEMbranes. With the gained experience, the bending was achieved through exposing the structure base, where the NanoBit was left attached to the milling frame. These NanoBits may directly be assembled by specially fabricated AFM probes: a plateau probe with a slit opened on the surface can be used for 90°-bent NanoBit while an AFM probe with a side-slit can pick up the NanoBit that bent <90°. Since the slits on the AFM probe were also milled by FIB, any probe with an appropriate slit shape and position to match the target NanoBit can be realised (see Figure 53).

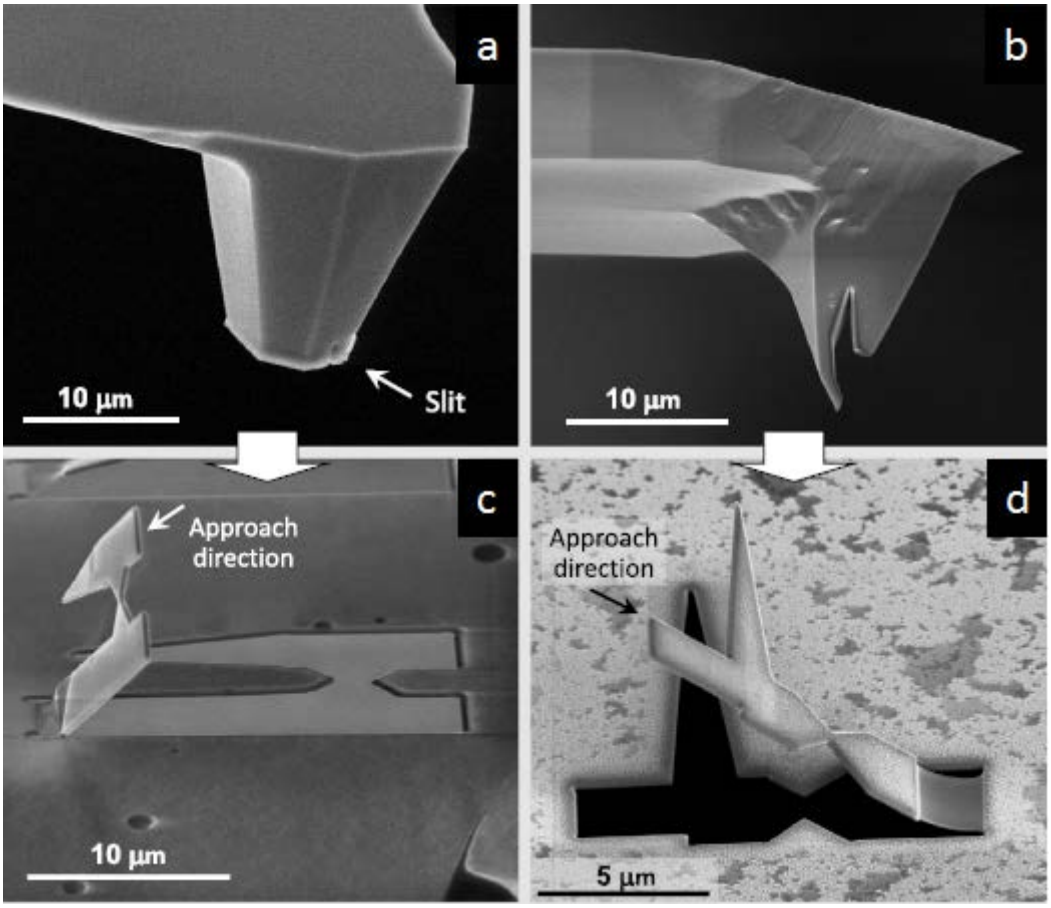

Figure 53 With specially produced AFM probes (a-b), NanoBits that are bent at different angles (c-d) can be picked up directly. The slits on the AFM probes are milled by FIB also, which presents a high flexibility in fabricating a target-specific probe.

5.3 Out-of-plane bending by bilayer stress

Bending of the bimorph structures is explained in terms of the relaxation of stress that the deposited metal film imposes on the system, with the total stress being a combination of external, intrinsic and thermal stresses [71]. When the system is not under influence of an external force, only the intrinsic and thermal stresses play a role in the curving of the bimorph structure. There are several factors that induce intrinsic stress, yet the exact mechanism or the total influence of these factors is still not entirely understood. A few that are discussed in literature are: lattice mismatch between the two layers [30, 71], defect formation/annihilation [30], grain boundaries [30], doping [71], atomic peening [71], and gas entrapment in metal layer [71-72]. Thermal stress is created due to different TECs of the metal and substrate materials, leading to variations in stress with the changing temperature. Due to the complexity of the stress-inducing mechanism, and its dependence on exact processing conditions [30, 72], issues such as the predictability and controllability of the bending curvature are of major concern.

To induce bending, 25–125 nm Ni films were electron-beam evaporated onto the NanoBit cantilevers in the Wordentec QCL 800 thin film vacuum deposition system. Since the exact deposition conditions are known to affect the film quality, and thus influence the intrinsic stress, all evaporation experiments took place in an environment controlled as tightly as possible, with 5±1 Å/s deposition rate and $2.6\pm0.4\times10^{-6}$ mbar

chamber pressure at RT. Figure 54(a-d) shows three NanoBit NEMbranes (200 nm pSi) deposited with 50 nm, 75 nm and 100 nm Ni.

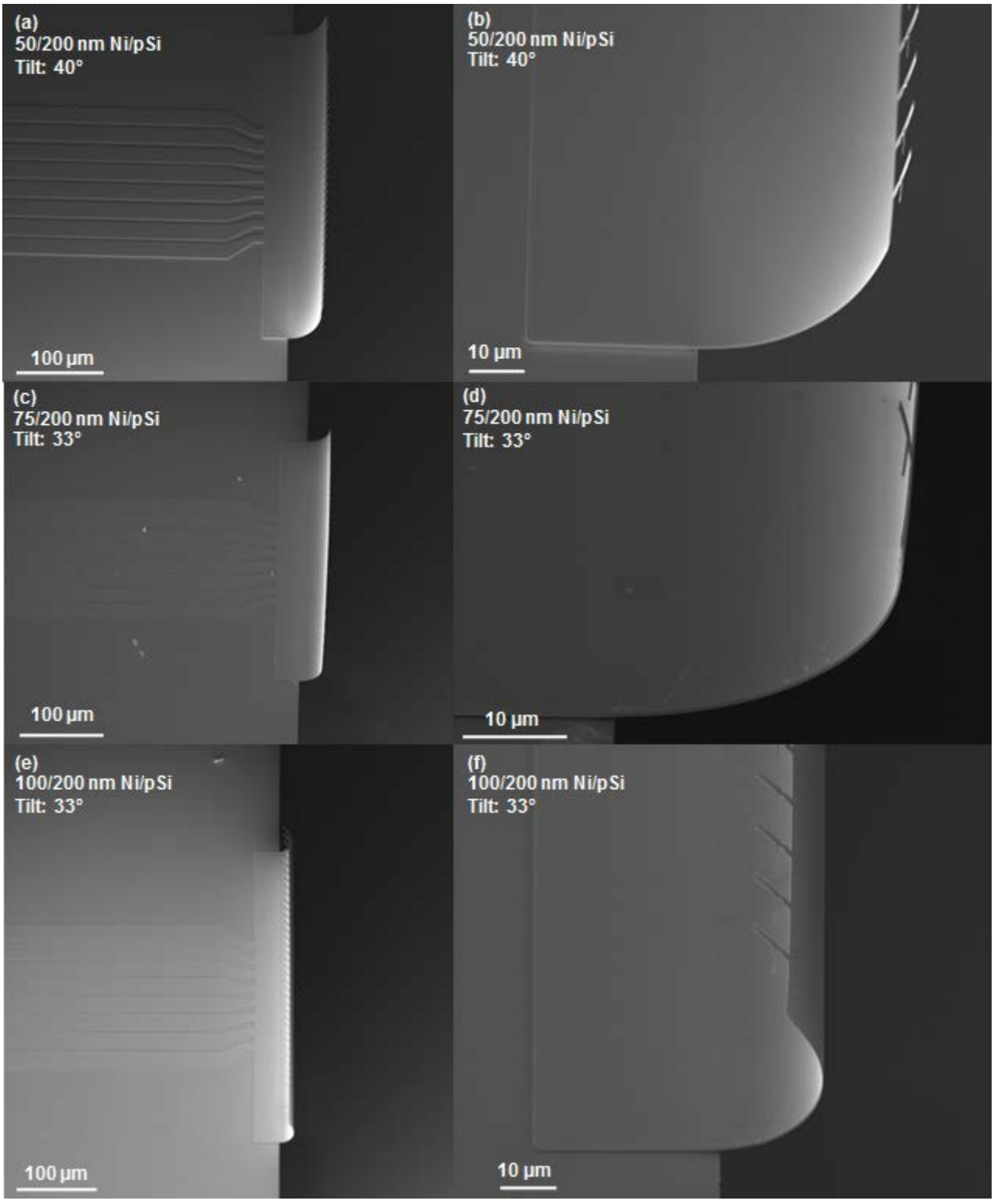

Figure 54 SEM micrographs of OOP-bent Ni/pSi bimorph structures: 50 nm (a-b), 75 nm (c-d), and 100 nm (e-f) Ni evaporated onto 200 nm pSi NanoBit NEMbranes.

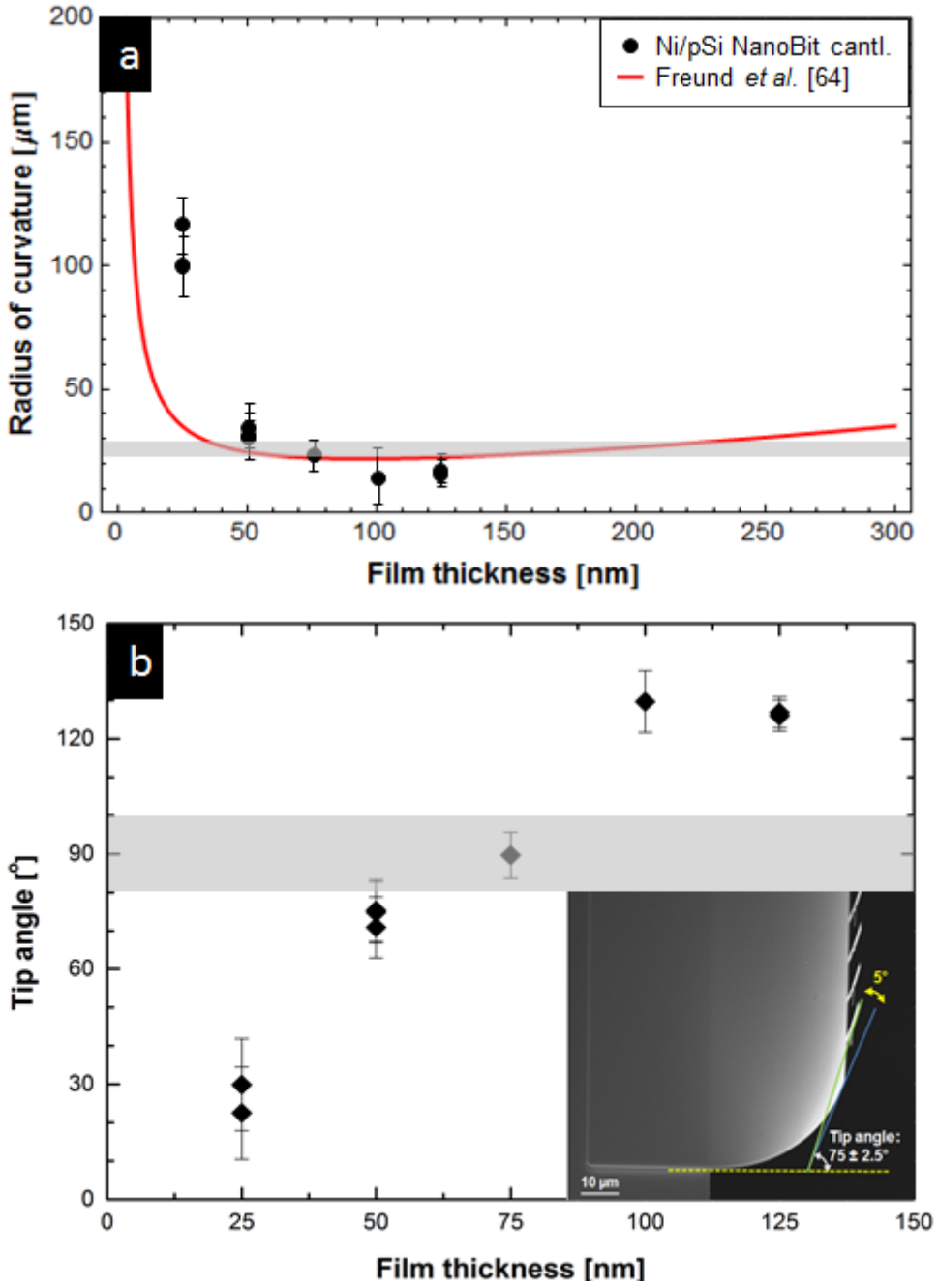

Figure 55 (a) The points show experimental data from Ni deposited on pSi NEMbranes. The red curve shows the theoretical radius of curvature estimation as a function of metal film thickness. (b) Corresponding measured tip angles of the NanoBit NEMbranes. (Inset) SEM micrograph of a bilayer NanoBit membrane bent by 75°: dashed yellow line shows the NEMbrane flat whereas solid green and blue lines indicate how the angle is measured. In all measurements the angle with respect to the microchip plane could be determined well within ±2.5°. Transparent grey boxes in *a* and *b* illustrate the acceptable bending window for the NanoBits.

In Figure 55(a) the curvature radii of the cantilevers measured from SEM images are plotted against the estimation by Eqn. 31. For modelling, E_f = 200 GPa, E_s = 170 GPa, ν_f = 0.28, and ν_s = 0.22 [30, 73] were taken for Ni and pSi, respectively. The increase of film thickness resulted in lower radii of curvatures, ρ; i.e. higher curvatures, κ. The lowest ρ measured was 18.5 μm. Beyond 100 nm, the bending showed an increased ρ. The corresponding tip angles were plotted in Figure 55(b). While the thinnest film (25 nm) resulted in a

mean tip angle of 26.2°, 50 nm and 75 nm Ni films produced NanoBit NEMbranes that bent close to desired degrees: ∼74° with 50/200 nm and ∼90° with 75/200 nm Ni/pSi. 100 nm and 125 nm Ni resulted in tip angles >120°, which are clearly above the desired angle window of 90°±10°.

Freund *et al.*'s extended Stoney formula [64] was also used with a different set of samples based on DuraSiN Si_xN_y membranes (DTF-1523 and DTF-2523) for TEM. The main motives for utilising a silicon nitride sample were: (i) it is a mechanically strong and reliable material, which is crucial if to be used as a NanoBit material, (ii) since a pSi NEMbrane was not available at the time as well as would take time and be costly to fabricate, Si_xN_y NEMbranes presented as reliable samples for characterising the effects of geometry of the cantilevers regarding bending, and (iii) a new substrate material would allow the investigation of the applicability of Eqn. 31 for different materials.

Arrays of cantilevers with dimensions ranging from 5 μm x 5 μm to 15 μm x 15 μm, were milled by FIB into 100 nm and 200 nm Si_xN_y membranes. 50 nm and 75 nm Ni were evaporated onto the pre-patterned membranes. The resultant Ni/Si_xN_y bilayers were investigated in SEM for radius of curvature and tip angle measurements. The bilayers are pictured in Figure 56(a-d), evaluated concerning the effects of size, film and substrate thicknesses in Figure 56(e-f), and compared to the theoretical prediction given by Eqn. 31 in Figure 56(g-h). For Si_xN_y E_s = 230 GPa and ν_s = 0.24 were used [74].

The silicon nitride NEMbrane chips were studied by SEM. In four of these test chips, the 100 nm Si_xN_y sample deposited with 75 nm Ni fractured in the center, with broken pieces rolled up toward the NEMbrane edges (see Figure 56(c)). The rest of the membranes remained intact. In all arrays, the cantilevers were successfully freed from the host membrane during the FIB milling stage, and bent upwards as expected. In the following the results are discussed with regards to metal film thickness, substrate thickness, and the cantilever geometry (see Figure 56(e-f)).

In terms of the Ni film thickness, a comparison was made between 50/200 and 75/200 nm. With the increasing metal thickness, the bending degree of the cantilevers increased as expected. The difference, however, is not substantial: halving of the radius of curvature ρ is followed by doubling of the tip angles, with the longest cantilever reaching 28° from 15.4°.

Thinning of the nitride substrate from 200 nm to 100 nm invoked a pronounced decrease in ρ: halving the substrate thickness reduced the radii of curvatures roughly by a factor of 4.5. Subsequent tip angle measurements revealed that the shortest cantilevers tripled their tip angles, from 9° to 28°, while the improvement was six-fold for the longest, from 15° to 87°.

In each array of cantilevers, the increase in cantilever length entailed increases both in ρ and the tip angle. As the cantilever length increased from 5 μm to 15 μm, the resultant ρ and tip angles roughly doubled for 50/200 and 75/200 nm samples; the 50/100 nm cantilevers showed an increase in ρ by a smaller factor of 1.5 while the tip angle were observed to triple.

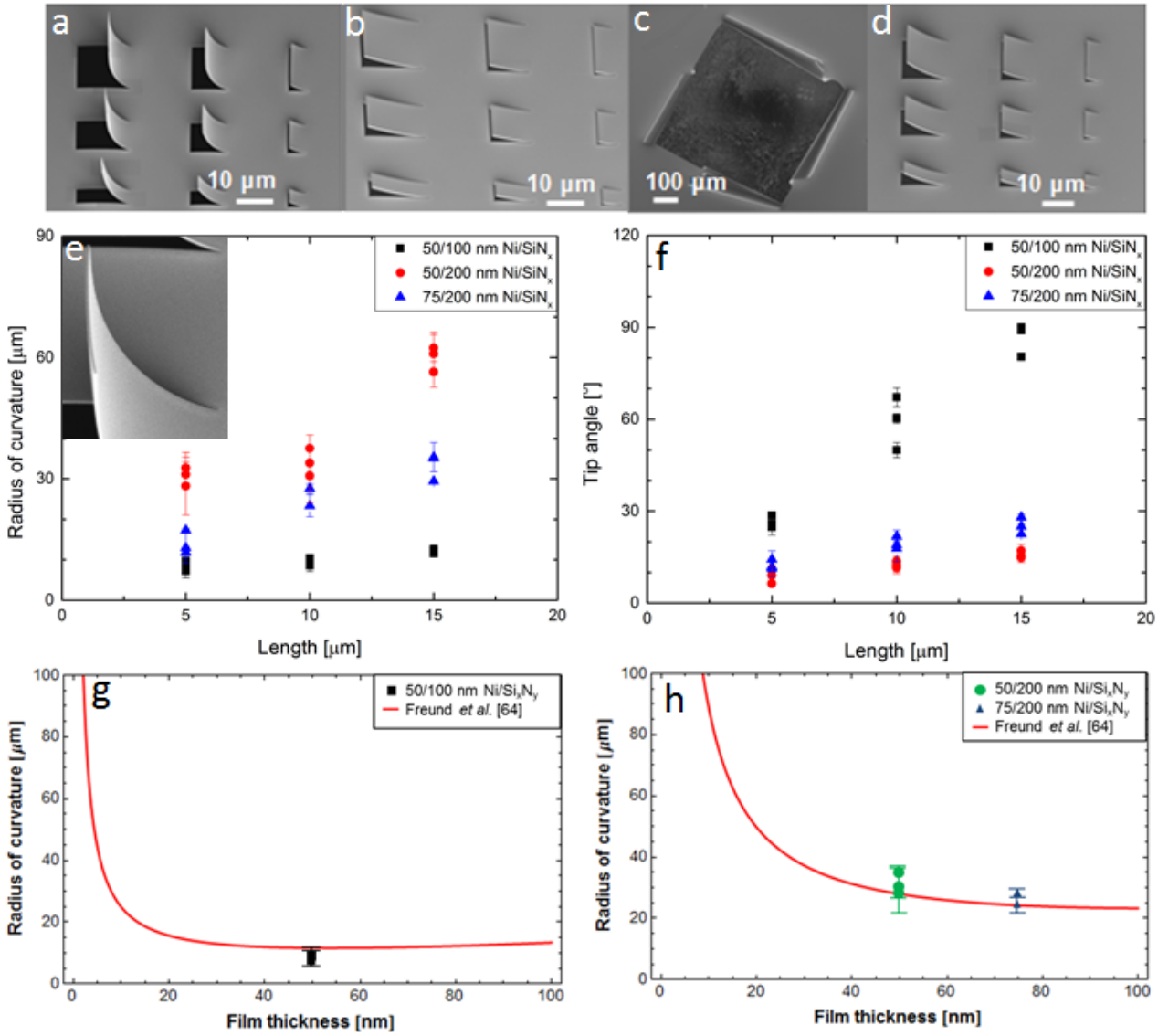

Figure 56 Cantilevers with various dimensions defined by FIB milling of 100 and 200 nm Si_xN_y membranes. 50 nm and 75 nm Ni e-beam evaporated onto NEMbranes of both thicknesses. (a-d) From left to right: SEM micrographs of 50/100, 50/200, 75/100, and 75/200 nm Ni/Si_xN_y samples. The NEMbrane in *c* (75/100 nm) ruptured after metal deposition due to high residual stress. *(e)* Radius of curvature tendencies of the cantilevers (on samples shown in *a*, *b*, *d*) as a function of their length. In each sample, cantilevers that have the same length differ in width. The radius of curvature is seen to scale roughly with length. (Inset) The cantilever corners bend both in long (longitudinal) and short (latitudinal) axes, which may contribute to the mechanical stability and rigidity of the cantilevers. *(f)* Tip angle plotted against the cantilever length shows that the angle is increasing roughly proportional with the length. Although doubling the film thickness makes a nominal change (comparing red circles to blue triangles), halving the substrate thickness results in considerably higher tip angles (comparing black squares to red and blue data points). *(g-h)* The model proposed by Freund *et al.* (Eqn. 31) provides sufficiently accurate radius of curvature estimations. The data extracted from 100 nm and 200 nm samples for 10-μm-long cantilevers are plotted in *g* and *h*, respectively.

For the 100 nm Si_xN_y NEMbrane, the estimated average radius of curvature (11.1 μm) is very close to the measured average (9.5±0.9 μm). For the 200 nm NEMbranes, the model's radius of curvature average for 50- and 75-nm-thick films was found to shift by averagely 7.4% from the measured average of the cantilevers.

According to the Eqn. 31, a certain thickness is required to achieve significant bending. Furthermore, the bending for the NanoBit membranes below 50 nm (Figure 55(a)) is even smaller than predicted by the model. While such behaviour can be understood in the known tendency for thin films in early stage growth to form clusters and islands and generally be of poorer quality [75], the total thickness of the NanoBits should be made as small as possible to maintain a sharp and well-defined tip. One possible route to solving this problem is effects and procedures resulting in a sharpening of the NanoBits described in [28]. Other could include the method in section 4.5. Additionally, strategies for avoiding film breakup could as well include wetting/adhesion layers like Cr or Ti.

The stress in the Ni film, driving the bending, depends on many different factors. The origin of intrinsic stress in evaporated films is a complex issue and a comprehensive review is beyond the scope of this study; the reader is encouraged to refer to [30, 71-72] for further information. Based on the experimental data, however, following observations were made, which are important when designing out-of-plane structures:

According to Klokholm and Berry [65], the intrinsic stresses in evaporated films can be divided into a part that originates from interfacial effects and depends on the two materials in contact, and a growth contribution, which is a result of shrinkage, annealing and rearrangement of disordered metal as it is buried under advancing layers. Thermal stress is the part of the stress which can be directly related to the mismatch of TECs. The thermal stress can either be caused *in situ* by the film being deposited at an elevated (or just different) temperature than the temperature at which the system will be operated, e.g. RT, or *ex situ* by heating the fabricated bimorph structure to change the curvature dynamically.

As was pointed out earlier, the internal stress and the microstructure of the metal films that satisfy the condition $T/T_m > 0.25–0.3$, such as Ni (T_m = 1726 K), will be dominated by growth stress. The structure of an evaporated film is known to be highly dependent on the deposition rate [30-31]. To confirm the relation between deposition rate and stress for the NEMbrane structures, the stress derived from the curvature of the NanoBit NEMbranes was compared to the stress induced in wafers using the same deposition process. A number of blank wafers were Ni-deposited at various deposition rates. The stress for each wafer was measured by a Veeco Dektak surface profiler. The measurement data is then compared to the average residual film stress, given as a function of radius of curvature [76]

$$\overline{\sigma_f} = \frac{-\left(E_s h_s^3 + E_f h_f^3\right)}{6 h_f (h_s + h_f)\rho}. \tag{33}$$

The intrinsic stress measurements for individual wafers, $\sigma_{0,w}$, and the residual stress of NanoBit NEMbranes, $\sigma_{0,N}$, calculated by Eqn. 33 are plotted in Figure 57. The tensile stress in the metal layer clearly increases with the deposition rate for both membranes and wafers. The strong dependence of the stress on the deposition rate supports the notion that the intrinsic stress is determined by growth-related processes, which implies that accurate control of the growth parameters is vital to obtain reproducible results.

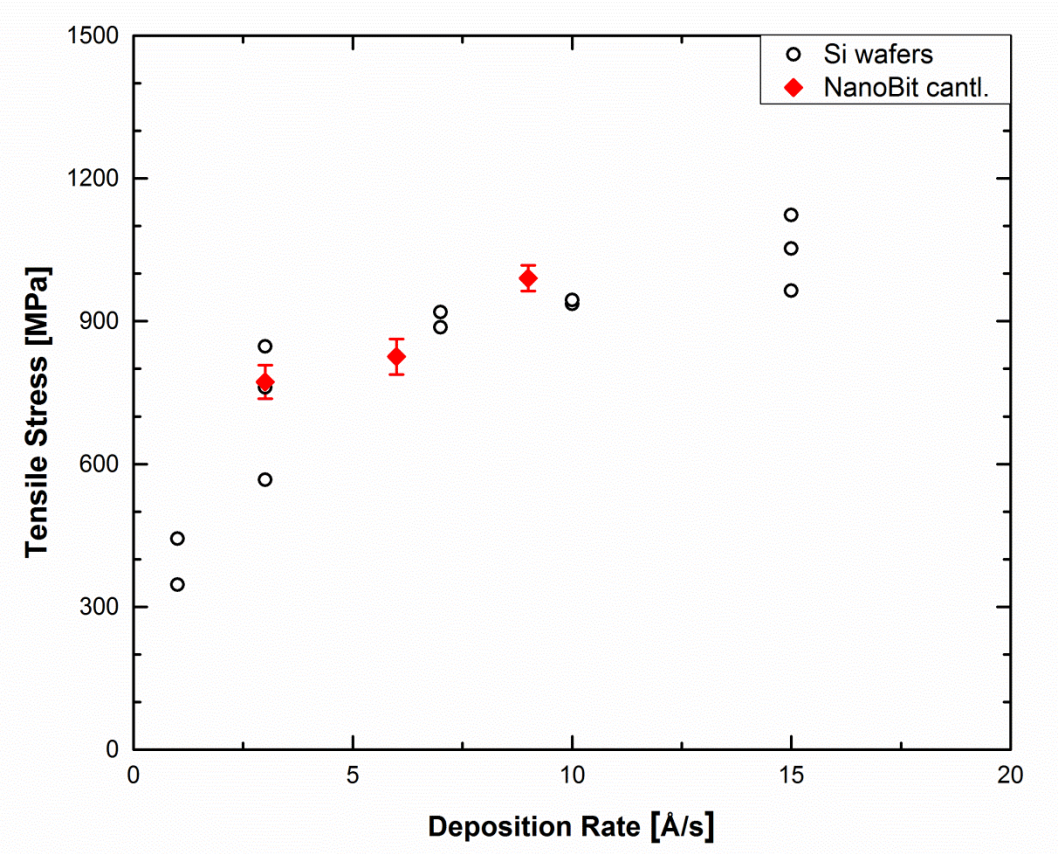

Figure 57 Total residual stress in the bilayer for various deposition rates. The tensile stress created by Ni evaporation is proportional to the metal deposition rate, showing a considerable increase until 5 Å/s (from ~400 MPa to 850 MPa) whereas the contribution of higher rates is relatively small (from ~850 MPa to 1100 MPa). Stress calculations from the curvature radii of NanoBit NEMbranes (red diamonds) showed a fine correlation with the intrinsic stress measured on the Si wafers (black rings).

In situ thermal stress concerns a contribution to the residual stress by elevated temperature during deposition. This could be caused by (i) direct heat transfer from the hot metal being deposited on the substrate, by (ii) the evaporation chamber temperature being elevated during deposition or by (iii) deliberate substrate heating. While substrate heating is a known issue for evaporation processes [31, 72], temperature changes of several hundred degrees to contribute largely to bending is unlikely. In [77] the temperature changes reported are up to tens of degrees.

Deposition onto thin NEMbranes could lead to a slower heat transport away from the deposited area, and therefore a higher surface temperature during deposition. This would contribute to a positive increase of tensile stress with deposition rate, as the heat flux will obviously depend on the amount of hot metal impinging on the surface. However, the good agreement between the two experimental data may suggest that the effect of the thermal stress is not very high in bending of the thin NEMbrane structures due to presumably elevated temperatures during deposition. The reason is that, even a low heat transfer rate could be assumed for the NEMbrane structures due to their thinness and isolation from the main chip body, Si wafers were in good thermal contact with the deposition chamber, indicating that the chances of reaching considerably different elevated temperatures for the wafers and NEMbranes are slim.

On the other hand, one observation does suggest thermal stress to play a role. If the stress in the freestanding membranes is solely due to growth stress with the NEMbranes being essentially at room temperature, the membranes should start to bend immediately while the metal is being deposited. Even if the bending is moderate initially due to the small thickness of early stage film (see Figure 55(a)), the bending of NEMbranes *in situ* should result in uneven metal layer, as well as deposition on the edge facing upwards, towards the direction of the incoming metal. Close inspection of SEM images revealed that the film thickness is very homogeneous even on the 90°-bent structures, and no visible metal film coverage is observed on the back (for >90°-bent structures). In Figure 61, 100/200 nm Ni/pSi NanoBit NEMbrane is shown bent by ~130°. The magnified image of the NanoBit backside clearly shows that no Ni is present on the main body of the NanoBit. A layer with Ni is, nonetheless, present at the edges. This layer could be a mixture Ni and pSi formed due to diffusion of Ni atoms into the very thin (presumably ≤50 nm) pSi wedge while evaporation (cf. Figure 35 and Figure 36).

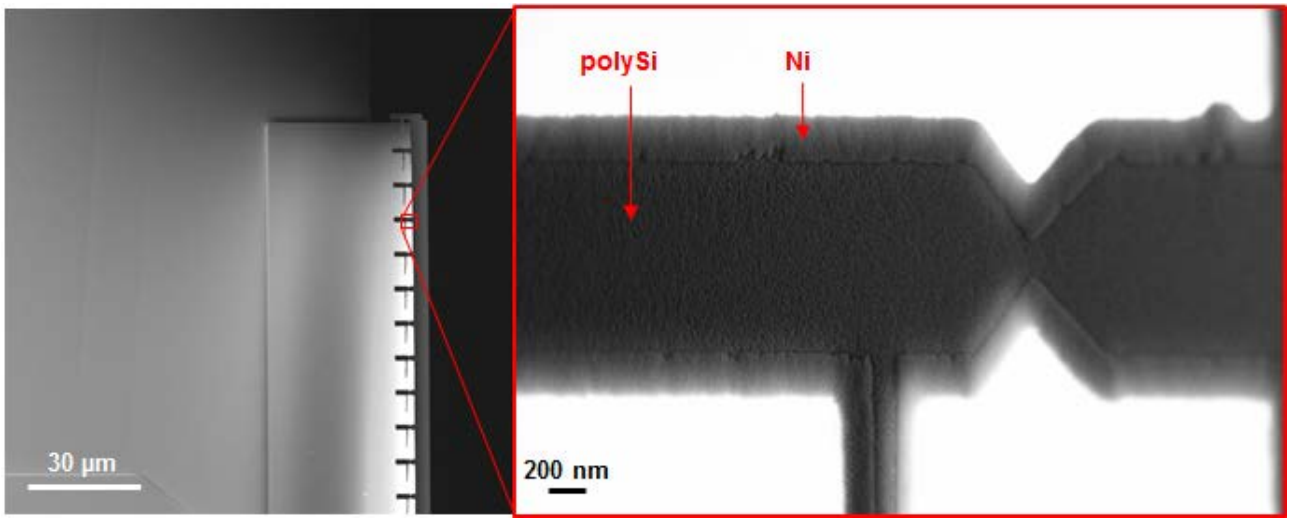

Figure 58 (Left) 100/200 nm Ni/pSi sample bent by ≃130°. The magnified image of a NanoBit backside signifies that no Ni is present on the backside of the NanoBit handle. A second layer apparent at the edges may be a mixture of Ni and pSi, which may have formed as a result of diffusion of hot impinging Ni atoms.

Therefore, if thermal stress contributes it would be in the form of elevation of the substrate temperature not by direct heat transfer from the metal, but by a general temperature rise in the chamber during deposition. This supports the hypothesis that the samples might be reaching a higher temperature during metallisation, contributing to the residual stress. In the literature, polymer/photoresist damaging cases have been reported with the possible cause being the heating of the substrate due to metal deposition [78-80].

While the data presented here does not allow any definite conclusion to be made regarding the possible role of thermal heating in defining the bending of the structures, the thickness and heat conductivity of the supporting structures are regarded as possible contributors to the stress.

5.4 Thermal actuation in bilayer structures

In the following the possibility of using a moderate variation of the temperature to fine-adjust the bending angle is considered. This would ultimately widen the acceptable process window.

Thermal actuation is a straightforward method to create thermal stress with changing temperature in the multimorph systems owing to difference between the TECs of the different materials. Because the thermal stress is directly proportional to temperature change, thermal actuation stands out as a viable option for controllably manipulating the bending. TEC of Ni is higher than Si and Si_xN_y. Therefore, any increment in the temperature will result in metal expanding more than the substrate material, creating a positive thermal stress, and thereby bending the bimorph towards the substrate (downward) while decreasing the temperature would create the exact opposite effect, bending the bimorph towards the metal film (upward). Given that the user confines his/her experiment to the elastic region of materials in question, thermal actuation is controllable, reversible and reproducible, allowing the user to finely adjust the curvature into the window of interest (90°±10° here).

50/200, 75/200 and 100/200 nm Ni/pSi NanoBit microchips were heated and cooled using a Linkam microscope stage with quartz window, which allowed real-time observation of the bilayer bending, and in a closed N_2 environment to prevent the metal oxidation. 100 sccm N_2 flow rate and 15°C/min temperature ramp rate were constant during all experiments. Thermal cycles were performed between RT and 590°C, and the membrane cantilevers were monitored from top, which offers limited capability in terms of exact tip angle. The NanoBits themselves, however, proved to be highly distinctive optical markers which deliver the necessary information on their position. Posing as self-markers, NanoBits and their angle can easily be detected by the user or by a robotics-software. Main, reproducibly observed characteristics of the Ni/pSi bimorph structures are listed below. (In the list, the directions “forward/downward” denotes bending towards the substrate; “backward/upward” denotes bending towards the metal film. $T\uparrow$ and $T\downarrow$ denote “annealing/temperature increase” and “cooling/temperature decrease”, respectively.)

Regardless of t_f,

- Bending is reversible for $T \leq 150$°C; i.e. the NEMbrane resumes its original position when cooled down to the initial T.
- At $T = 170$°C, while annealing, bending reverses its direction from forward to backward. This opposite movement lasts until $T = 275$°C. Cooling the sample from a point in this temperature window to RT results in ρ’s smaller than the initial, meaning the final tip angle is larger than it was in the beginning.
- While $T\uparrow$and $T \geq 275$°C, the NEMbrane resumes its forward bending, becoming flat (tip angle: 0°) as $T \simeq 300$°C. When $T\downarrow$ to RT, the cantilever bends upwards but to a small angle.
- When flat, NEMbrane is periodically buckled if no imperfection is present. Buckling points lie in the longer NEMbrane direction, being prominently visible near the chip edge (fixed-end of the NEMbrane cantilever), where the stress is higher, and hardly noticeable toward the free-end near NanoBits.
- The NEMbrane stays effectively flat for 300–400°C. Within this interval, NEMbrane corners *flutter*, bending upward and downwards, and curved NEMbrane topography constantly transforms with the buckled regions increasing/decreasing in size.
- The NanoBit membranes are entirely bent down when $T = 510$°C.

- As T↑, the microchips undergo re-colouration at
    - o T = 370°C: light brown,
    - o T = 430°C: dark brown,
    - o T = 480°C: purple/dark blue,
    - o T = 515°C: light blue,
    - o T = 545°C: greyish blue.

75/200 nm sample, in contrast to other microchips, flattened at T = 300°C (instead of 300°C) and started to bend down at T = 480°C (instead of 440°C). The reason for both incidences is very likely the broken region at NEMbrane center, visible in Figure 59 (bottom row): an additional buckling within this segment renders the membrane mechanically more stable while flat and less prone to bending.

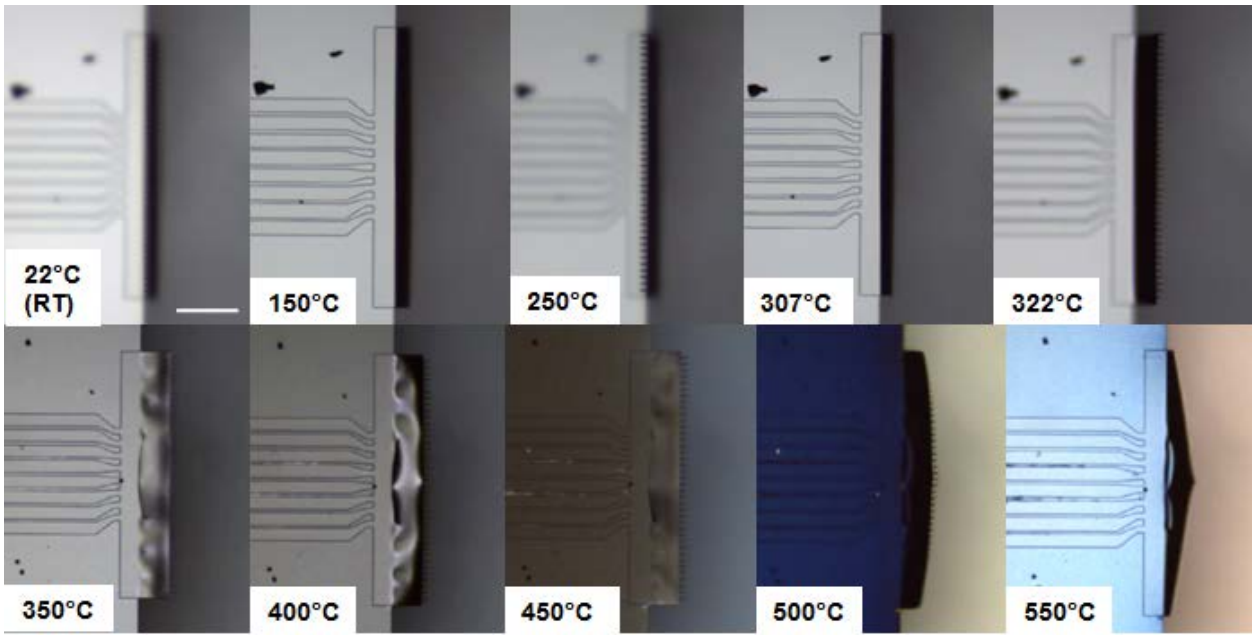

Figure 59 Thermal actuation is a viable postprocessing tool to align the NanoBits into the tip angle window of interest. The deflection of NanoBit membrane cantilevers were investigated for RT-590°C using optical microscopy. Top row: 100/200 nm Ni/pSi. Initially NanoBits are bent by ≃130° and are seen as blurry dent at the free end of the cantilever; camera focus was optimised to see NanoBits. Upon annealing, the cantilever extends and NanoBits disappear into the dark region, closing in to the right angle. Above 170°C the bending direction reverses: at 250°C, NanoBits are clearly visible on the left-hand-side. Bending direction resumes forward by 270°C, and above 320°C they are easily noticeable on the right-hand-side approaching the NEMbrane flat. Bottom row: 75/200 nm Ni/pSi. By 330°C the NEMbrane flattens. At this stage, buckling occurs due to highly anisotropic stresses as the NiSi forms. Mechanical resistance increased in the buckled structure, together with the continuous formation of NiSi phase, renders the membrane resilient to bending for ~110°C. The surface colouration begins around 370°C and lasts until 570°C. NiSi is stable until 700°C; therefore, the change in chemistry is attributed to the near-surface regions transitioning from Ni_2Si to NiSi. NanoBits proved to behave as self-markers as they can be distinguished both by the user and software. Scale bar: 100 μm.

The expected tendency of linear elastic progression was observed in all samples until 150°C. Below this point, the bending is reversible and reproducible. A tip angle modification of ≥±10° was observed.

The reversal of bending during annealing, starting at 170°C and lasting more than 100°C, was unexpected and counter-intuitive. The reduced ρ of the membrane when cooled down to RT (stronger backward bending) points to increased stress in the system. Repeatedly encountering the same phenomenon with

the other samples, which have thinner/thicker films, and observing an irreversible behaviour in numerous runs signifies that the membrane is moving plastically, hinting the alteration of the chemical composition. The recent studies by [81-84] report the formation of a Ni-rich silicide, Ni_2Si, at 200–300°C due to diffusion of Ni atoms that would generate a compressive stress as the Ni_2Si forms. The findings above suggest that this new phase might be forming already at 170°C, and/or the reorientation of the atoms and grains may be playing a role. At 275°C, Ni_2Si formation finalises and compressive stress relaxes as the sample is further annealed.

Before the NanoBit NEMbrane becomes flat, it progresses unevenly at the center and corners. Seeing that it is already buckled when flat at 330°C, it is understood that the buckling begins at T < 330°C. This could mean Ni atoms in Ni_2Si continue to diffuse into Si, starting to form NiSi. NiSi forms about 310–350 °C [83, 85-86] and have tensile stress [82] as opposed to Ni_2Si. So, approaching the NEMbrane flat ($T \simeq 330$°C), it is plausible to suspect that NiSi layer begins to form, incrementing the tensile stress in the system (likely, it is now trimorph), hence driving the bending in the forward direction. A further clue to NiSi is the buckling of the membrane, because "orthorhombic structure NiSi shows some very peculiar characteristics": [87] (i) TEC of NiSi is largely anisotropic, so that it can undergo contraction under increasing temperature, and (ii) the stress in the layer is highly localised, which can be four times higher than the average stress. In the light of (i) and (ii), due to the stress changes from compressive to tensile across grains, especially at elevated temperatures when the grain evolution is much favoured, Lavoie *et al.* [87] expect strong deformation of the texture. As noted before, locally buckled membrane must pose mechanically more stable also, further resisting to bending for an extended range of temperature (~ 110°C).

Colouration of the chip surface is noticeable around T = 370°C turning to a dull yellow, and continues until T = 545°C when the chip assumes a grey-blue colour. NiSi is a stable phase: Si-rich silicide, $NiSi_2$, nucleation commences only after exceeding 700°C [83, 88]. While annealing, however, with Ni known to be the active diffusing element in all phases [83], it is plausible to assume that Ni atoms continue diffusing from the metal-rich layer into NiSi/Si, until whole Ni_2Si is consumed. In this regard, surface colouration may be attributed to the phase transformation reaching device surface. Above 545°C, colour change terminated, which may accordingly imply the completion of NiSi formation.

5.5. Discussion and conclusions

Out-of-plane bending of NanoBits from their lateral plane to ~90° would allow riddance of the intermediary tools like microgripper and cartridge, hence NanoBits could be picked up directly by the AFM probe, which in turn would accelerate the assembly process. FIB irradiation of NanoBit-like Si_xN_y cantilevers showed that as the substrate thins down to 80–90 nm, the bending starts. Control of the dose results in controllable bending angle; bending angle was observed to overshoot the right angle (>90°) at higher doses. Actual NanoBits were shown to bend close to 90° and to a certain window (30°–60°) of tip angle. These NanoBits can be assembled by the AFM probe with a specially designed slit approaching from the respective direction.

Despite promising bending results obtained by FIB exposure, it requires serial treatment of the structures. Second method used to bend the NanoBits was the residual stress built up in bimorph structures, which can result in bending of whole NanoBit library to a desired level. 200-nm-thick freestanding NanoBit

NEMbranes were deposited 25–125 nm Ni; radii of curvatures and tip angles of the bent structures were measured, and compared to the theoretical models in the literature.

Tip angles varied from ∼25° to ∼130°. 75 nm Ni deposition on 200 nm pSi resulted in 90° bending of the NEMbranes, aligning NanoBits vertically. The models showed high correlation with the experimental results, but failed in estimating the bending degree especially for low metal thicknesses (<50 nm). This discrepancy can be attributed to the island formations of the film during the initial stages of deposition, because all examined models assume uniform films for all thicknesses. Analyses and experiments with different materials showed that the main driving force for the bilayer bending is the intrinsic stress built up in the system. Building stress, however, should be simultaneously bending the NEMbrane during deposition, which should show itself in uneven metal film deposition on the topside as well as a deposited layer on the back. SEM inspections provided no signs of the either. That is, the growth stresses may be playing the prominent role in bending of the bilayer structure while the thermal stresses contribute to further bending in the form temperature elevation of the substrate and/or the deposition chamber.

Stress formation in the films is complex issue and bending was observed as not easily controllable. Although the desired degree of bending cannot be attained after the metal deposition, it was demonstrated that the tip angle can be fine-tuned by thermal actuation. Up to 150°C, the bending is reversible and the NanoBits' angle can be modified within ±10°. At higher temperatures reversal of stress from tensile to compressive, buckling, and changing of surface colour were observed, pointing to silicidation of the structure starting at 170°C and continuing until 590°C, the highest temperature the measurements were done.

6 Manipulation

The manipulation of the NanoBits concern their assembly into a plateau AFM probe and usage as AFM tips. In this chapter, the manual assembly process is presented with highlighting the important points, and then the automated assembly is briefly discussed including the final cartridge design for a safer handling. The scan performances of the assembled NanoBits were tested on quartz samples and were compared to commercially available AFM tips. Durability tests of the NanoBits were conducted on resist substrate for 30 hours. Eventually, the alignment issues encountered during the assembly of NanoBits were assessed.

6.1. Setup and preparation

The manipulation experiments of NanoBits were done at OFFIS and led by Malte Bartenwerfer. The mobile microrobotic equipment used in Tescan Lyra FIB-SEM dual beam system, NanoLab (a closed-loop nanorobotic assembly system), consists of two piezoelectric actuator units: one unit for the supply and positioning of the AFM cantilevers and the other unit for nanometer-precise handling and mounting of NanoBits. One advantage of these mobile microrobots is the easy integration of various tools: from a simple sharply etched tip to a microgripper or an AFM cantilever, many tools for micro- or nanohandling tasks can be integrated [89].

In the NanoLab setup the microgripper-based manipulation scenario including the cartridge concept was pursued. The gripper-based nanomanipulation/assembly approach had already been proven as well suited for offering high flexibility and prototyping of NanoBits devices [17, 28, 69, 89-90].

6.2. Assembly

6.2.1. Manual assembly of NanoBits

The FIB-milled NanoBits were assembled in two steps. The first step was the transfer of NanoBits from source reservoir to a temporary cartridge, where they would be kept until usage (see Figure 61). The second step was the insertion of NanoBit into plateau cantilever, as it is shown in Figure 62. For experimental implementation of this procedure, a NanoBit reservoir manufactured by FIB, thermally actuated microtweezers and an AFM plateau (tipless) cantilever with several slits milled on the surface were prepared [90]. Figure 60 shows these three items.

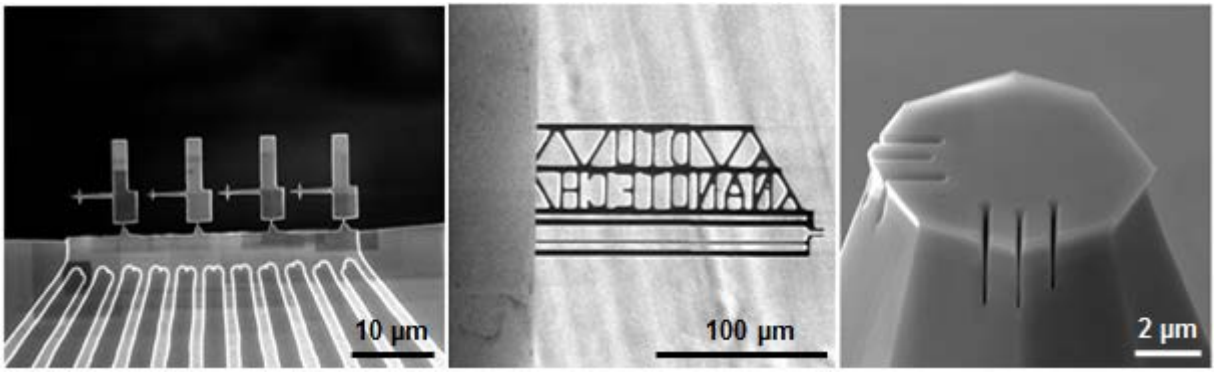

Figure 60 The overview of reservoir with four NanoBits in it; thermally actuated microtweezers that were used to grip NanoBit; plateau cantilever that was used to place NanoBit into the slit.

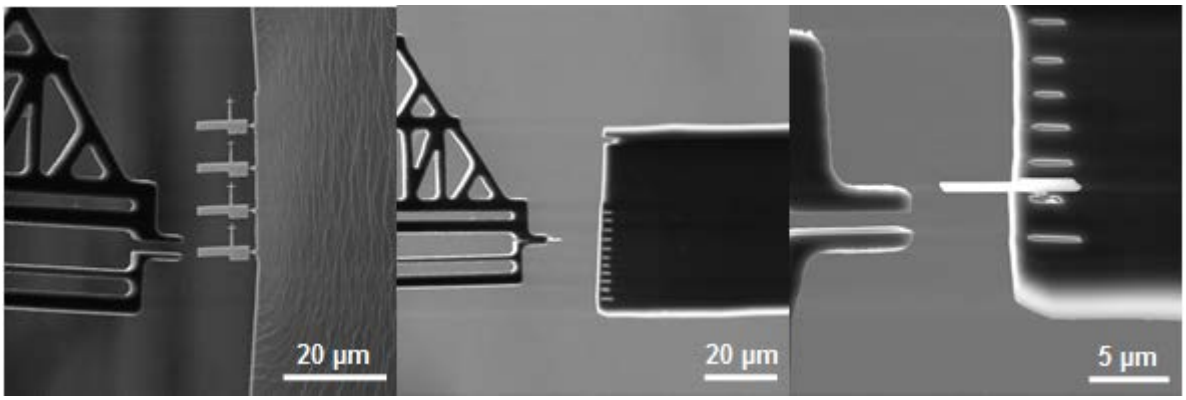

Figure 61 The 1st step: NanoBit's transfer to cartridge.

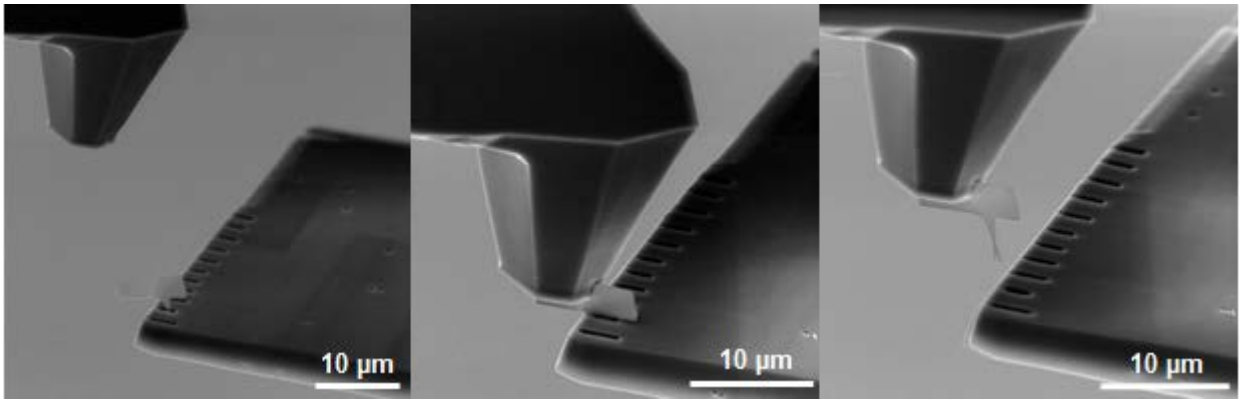

Figure 62 The 2nd step: picking up NanoBit from the cartridge by AFM cantilever [90].

During the experiments a few points proved essential for a successful NanoBit assembly into cantilever:

All-around observation of the ongoing process was highly beneficial in understanding the actual position of the micromanipulators. The view provided by SEM and FIB detectors was crucial for operations of positioning of NanoBit into the gripper end-effectors for a reliable fixation, insertion of NanoBit into the cartridge slit, fastening of NanoBit into the plateau cantilever, and other manipulations of objects relative to each other.

FIB polishing of gripper end-effectors affected the manipulation in many ways: (i) FIB machining resulted in etching of the gripper jaws from angle, giving the jaws slanted (10–20^{o}) sidewalls. Alternative of this operation is the tilting of the gripper itself (cf. Figure 7). (ii) The polished jaws gained a smoother surface, which turned out to be significant in increasing the contact area with the NanoBit, hence provided a better gripping. (iii) With native SiO_2 layer removed, the stiction between the hydrophobic end-effector surfaces and NanoBit should have reduced.

Tilting gripper by 10–20^{o} along its long axis was observed to yield an increased performance, compared to its FIB-milled sidewalls alternative, in turning the NanoBit from in-plane to out-of-plane (downwards). The experiments revealed that a completely tilted gripper provides much more predictable and reliable results.

The slanted-jaw approach increases only the probability of the NanoBit to turn into the determined direction compared to its in-plane orientation. In some cases, turning did not occur and the NanoBit remained between the two closed jaws. In very few cases, a turning in the counter-direction was also observed. Using the tilted gripper approach however, turning occurred in all trials in the desired direction.

Originally, the tilted gripper bore the disadvantage of being in close proximity to the wafer surface, where NanoBits had been manufactured formerly [17]. As the microfabrication presented here created chips (instead of a full wafer) that carry freestanding NanoBit arrays protruding over the edge, this constraint was eliminated, and therefore, the assembly of NanoBit cartridges can rely on the tilted gripper approach.

Narrow cartridge cavities required long and careful manual operations both of the gripper and AFM probe. The most prominent reason was the stiction of NanoBit to the cavity sidewalls as soon as it was tried to be inserted. Secondly, aligning of the NanoBit tip into a 350-nm-wide cavity without causing any sort of damage was challenging, because the operator needs the location of the NanoBit in 3D. Insertion into both the cartridge and AFM probe was successful, however, required a certain level of expertise on the operator's side. Wider and more secure (with some room for NanoBit's motion) cavities should allow much faster and reliable assembly steps.

6.2.2. Automatic assembly of NanoBits

This subsection presents the mechanical components involved in the NanoBits' transfer processes. The final design of the cartridge cavities, microgripper-based assembly strategy with preliminary results of the automation process, and a feasible strategy for mounting NanoBits inside an AFM environment are presented.

Final design for cartridges and cantilever

The purpose of the cartridge is to store the NanoBits and act as a carrier to make them accessible for the AFM cantilever. For this reason, they have to fulfil particular demands:

i) During the insertion process of the NanoBit, the tip of the NanoBit should not touch surfaces, since it has to be protected from any damage.

ii) After the insertion, the NanoBit has to rest in the cartridge stable enough, allowing the gripper to retract.

iii) The NanoBit should be well aligned with the entire cartridge structure.

iv) During the pick-up process by the cantilever, where a certain force is applied to the NanoBit, the tip should not touch any surface. The design, meeting these demands, is shown in Figure 63: Trenches give the inserted NanoBit a distinct orientation and footing during the pick-up process. The bigger aperture in the middle prevents the NanoBit's tip from touching any surface during the insertion while the conical opening on the backside does the same during the pick-up process, during which a certain force is applied to the NanoBit in potentially unpredictable directions.

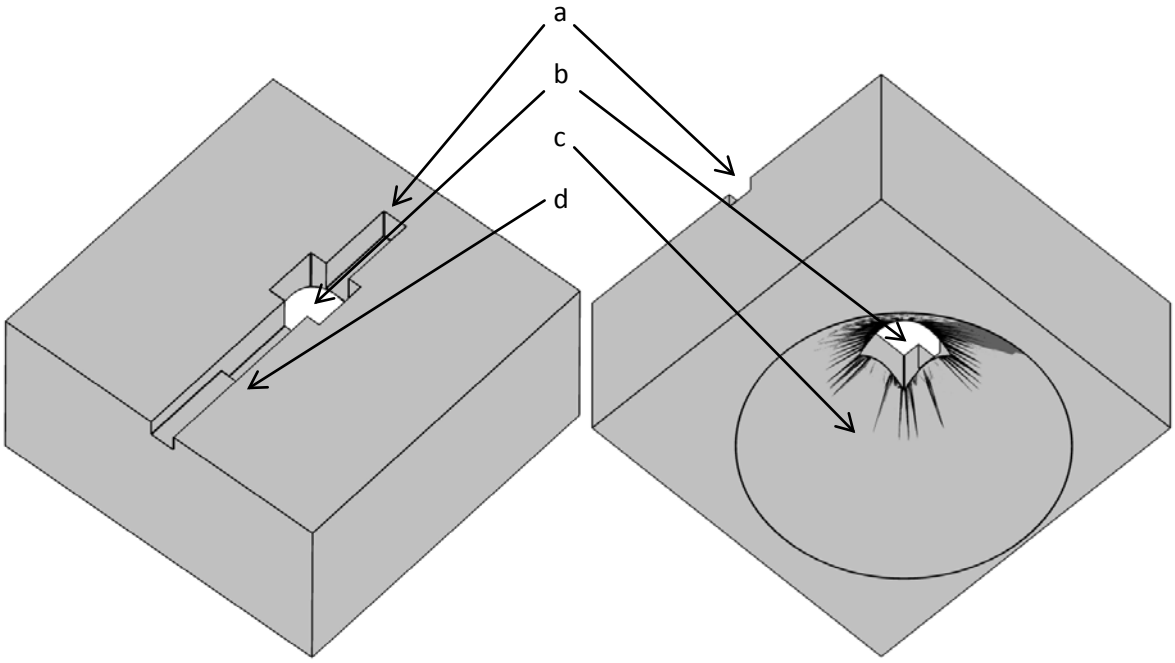

Figure 63 Technical drawings of the cartridge design in top and bottom view. The trench (a) keeps the NanoBit well aligned with the entire structure. The big aperture in the middle (b) and the conical opening (c) on the bottom prevent the tip of the NanoBit from any contact with the surfaces, even during the pick-up process. An additional step (d) in the trench eases the detachment of the NanoBit from the gripper during retraction. [Image reproduced with permission from Malte Bartenwerfer.]

The shape of the cavity was realized by FIB milling. A Si cantilever with 4 µm thickness was used as template. Trenches, aperture and the opening were created by a two-stage milling procedure from top and bottom. The final result is shown in Figure 64. The trenches are 5.5-µm-long and 350-nm-wide. The aperture has 1±0.1 µm length and width.

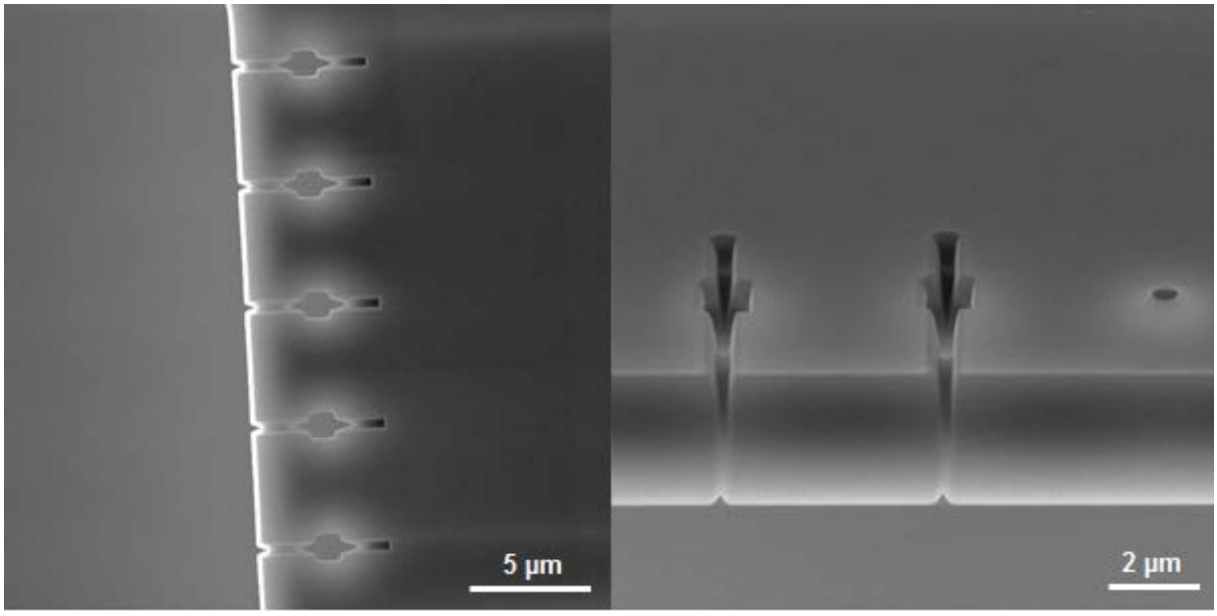

Figure 64 NanoBits cartridge produced by FIB milling. The trench, central aperture and conical opening (causing tapered borders of the aperture) are clearly visible.

Strategy for cartridge assembly

The automation of the cartridge assembly was developed by the OFFIS staff [91]. Here only brief information is provided.

As the starting point, the gripper and NanoBit have to be aligned in the *x*- and *y*-planes. In the handling setup, the precise location can only be determined using the visual feedback from SEM. The robots' internal sensors cannot guarantee the movement with sufficient precision due to temperature drift caused by the thermal gripper as well as the electrostatic charging of NanoBits. Thus, image-based visual servoing is used for closed-loop positioning, but this approach is still affected by distortions caused by the gripper and NanoBits. Performing *z*-alignment is possible via both template matching and shadow-based approach [91].

The actual automation sequence consists of the following steps:

1) The system is set to the initial position, where gripper and NanoBits are visible, and within reach Figure 65. The gripper needs to be positioned above the NanoBit.
2) A single image is acquired by SEM. Template matching for gripper and NanoBits is performed and provides the positions and amount of gripper and NanoBits.
3) The gripper is placed in *x,y*-plane close to the NanoBit. An additional image covering only the region of interest (the gripper and the particular NanoBit) is acquired (see Figure 65(c)) to improve the accuracy of the positioning.
4) A template-based position detection based on the image acquired in step (3) is performed.
5) The microgripper is set in *x,y*-plane directly above the NanoBit based on the new position detection.
6) There are two possible routes for height alignment:

a. The gripper moves down while oscillating in *y*-direction. As the gripper descends to the same height as the NanoBit, the oscillation causes a small movement of the NanoBit, which is detected by template matching (see Figure 65(c)).

b. As the gripper is lowered, the mean greyscale value of the NanoBit handle is simultaneously measured. When the gripper end-effectors are positioned around the handle, the region of interest (ROI) is *shadowed* since the electrons emitted from the surface are captured by the gripper end-effectors and thus the greyscale value of the ROI drops. Below a certain greyscale threshold, the microgripper grabs and dislocates the NanoBit for later cartridge mounting (see Figure 65(d)).

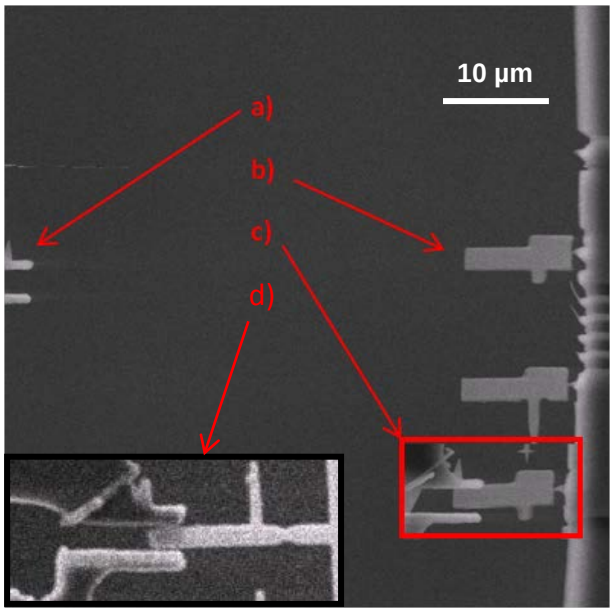

Figure 65 The automated gripping sequence. The gripper (a) and the target NanoBit (b) should be located in the same frame. Then, for the height alignment, either bending of the NanoBit due to lateral oscillation of the gripper (c), or the shadowing of the NanoBit handle (d) is performed. [Image reproduced with permission from Malte Bartenwerfer.]

Strategy for mounting NanoBits

The general idea of mounting remains the same as in the case of FIB-milled NanoBits in section 6.2.1. The shadow-based approach, on the other hand, proved promising while insertion of NanoBits into the dedicated slots of the reservoir. The NanoBit is brought on top of the targeted slot; the gripper is lowered until the NanoBit is fully inserted; as the mean greyscale value of the ROI drops noticeably, the gripper end-effectors are opened to release the NanoBit; then, the gripper retracts [91].

An evaluation of the bonding force was performed by pushing the NanoBit imaged in Figure 66 onto the surface of cartridge structure. Under visual observation by SEM, the displacement of the cartridge cantilever and the approximate corresponding force were measured using Eqn. 11: a force in the order of tens of µN's applied, yet no displacement of the NanoBit in the cantilever was observed. Since the contact mode AFM operates typically in the range of 10^{-7} to 10^{-6} N [92], $\geq 10^{-5}$ N of adhesive forces holding the NanoBit in the slit should be sufficiently large to keep the NanoBit stable while scanning a surface.

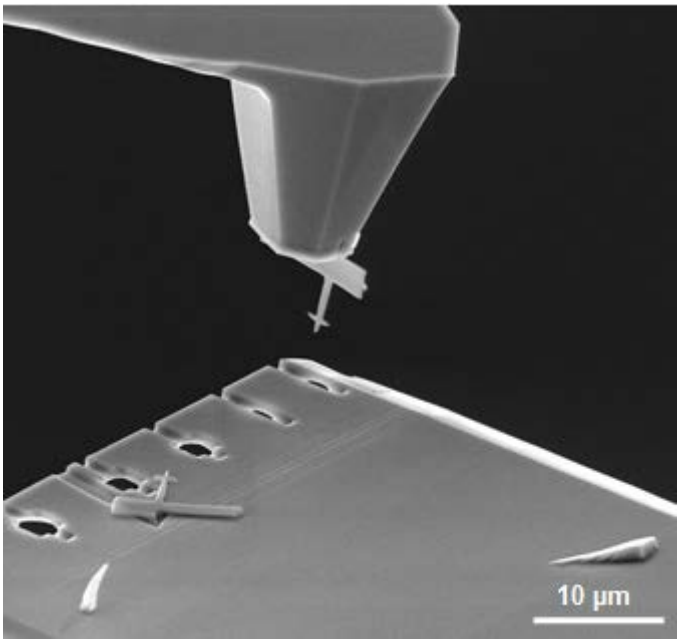

Figure 66 A mounted NanoBit was used to estimate its bond strength with the plateau-slit: while pushing the assembled tip against the cartridge cantilever surface the displacement of the cantilever were monitored. By using the Hooke's law (Eqn. 11), the force required to modify the shape or the position of the NanoBit was calculated as in the order or ≥10^{-5} N.

Strategy for automated mounting in AFM conditions

The strategy for the automated mounting of NanoBits within the AFM environment is divided in two steps:

1) Using the optical microscope of the AFM: the cartridge has to be positioned close to the target scan area.
2) The AFM scans a marker on the cartridge; using the input coordinates and dimensions of the cartridge and NanoBits, the probe finds the desired NanoBit with respect to the marker position.

This approach inside the AFM environment relies mainly on a smart design for the cartridge and particular alignment of structures in it. Figure 67 shows a sketch of the first prototypic cartridge design: for the coarse positioning, which is performed by the motorized AFM stage using the image-based visual servoing of the optical microscope, a 10 µm x 10 µm square (Figure 67(a)) is used. The square is larger than the plateau of the tipless cantilever; thus, its position can be found accurately by a simple AFM scan using the plateau cantilever. The square can be produced by FIB: ~100 nm depth is sufficient for AFM to detect it; since AFM modifies the structure of the milled area, an optical microscope could also determine its position with ease. In order to increase the accuracy of the AFM positioning, additional fine positioning markers are engaged (Figure 67(b)). These markers are fine needles, fine enough to fit into the slit of the plateau cantilever, which in turn should allow performing very fine positioning.

These needles have to be as close as possible to the trenches of the cartridge to prevent damaging of the NanoBits during the AFM scan (Figure 67(c)). Both markers and the cavities should be in a maximum range of 100 µm, which is the working range of the AFM scanner, in order to avoid repositioning steps required by the AFM motorised stage.

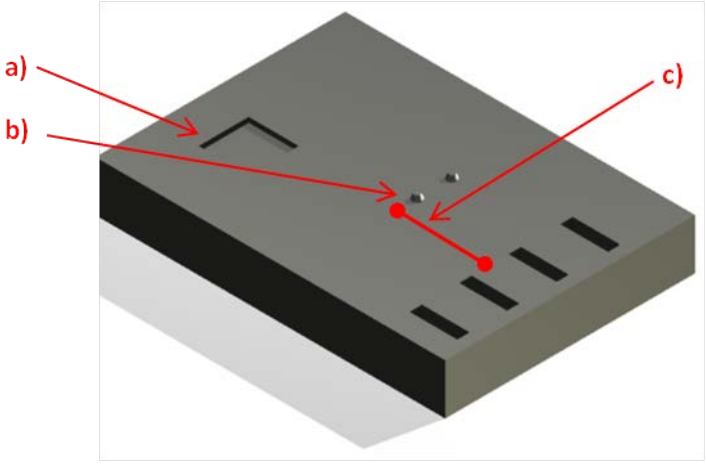

Figure 67 Sketch of the cartridge design for the AFM-based mounting of NanoBits. A square (a) is used for coarse and tiny pins (b) for the fine positioning of the cartridge relative to the AFM probe. The distance (c) to the cavities should be small for a rapid operation. [Image reproduced with permission from Malte Bartenwerfer.]

6.3. Scanning

AFM scan trials of NanoBits were done OFFIS using a JPK AFM and at DTU Danchip, DTU using the Veeco NanoMan (Dimension 3100). The experiments at OFFIS were partly supervised by Florian Krohs.

The mounting of the NanoBits onto AFM probes was carried out by (i) picking up of NanoBits via a microtweezer, (ii) their placement into the dedicated slots in the cartridge, and finally (iii) mechanical insertion into the FIB-opened slits on the AFM probe in Tescan Lyra FIB-SEM using the NanoLab. Two types of AFM probes were utilised: specially fabricated plateau and standard conical probes. The assembled AFM probes were then transferred to AFM for imaging. The test samples used for characterisation were actual optical gratings made of fused silica, manufactured by IOF Fraunhofer.

Figure 68 shows an assembled NanoBit (AR = 5) and its scan performance in contact mode. A chirped grating with 0.9-µm-deep trenches was used in this case. NanoBit was able to reach the bottoms of trenches that had ≥200 nm width, proving that it can be used for AR ≥ 4.5 structures. Comparison of this NanoBit to a commercial standard conical probe was performed using an almost identical sample (trench depth: 1 µm). While the conical probe could reach a depth of 350 nm, NanoBit was again able to scan the bottom of ≥200-nm-wide trenches (see Figure 69). The observed deviation of the scan profile when switched from trace (forward scanning) to retrace (backward scanning) may indicate movement of the NanoBit in the AFM probe slit. The differentiation is most explicitly observed for the wide trenches that the NanoBit can probe the bottoms of. If the NanoBit is not well fastened to the probe slit, it is possible that the capillary forces due to the water layer present on the structure surface may be exerting an attractive force as the NanoBit approaches to the trench sidewalls, which in turn may move the NanoBit in the scanning direction.

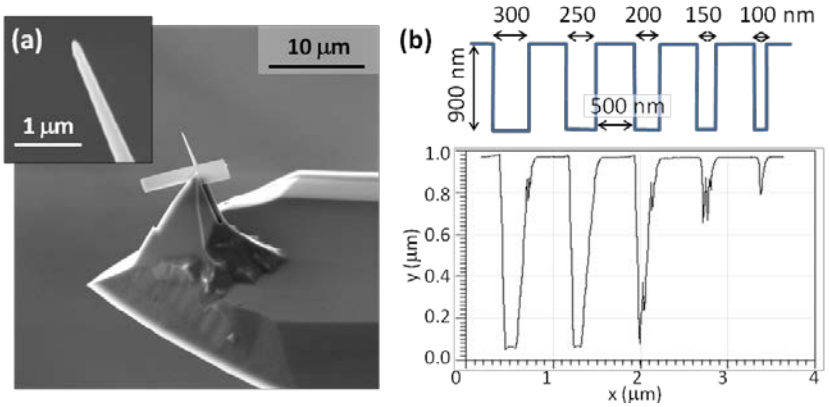

Figure 68 (a) NanoBit probe made by FIB milling and assembled by nanorobotic system. (b) AFM scan performed on a 0.9-µm-deep chirped grating by JPK AFM.

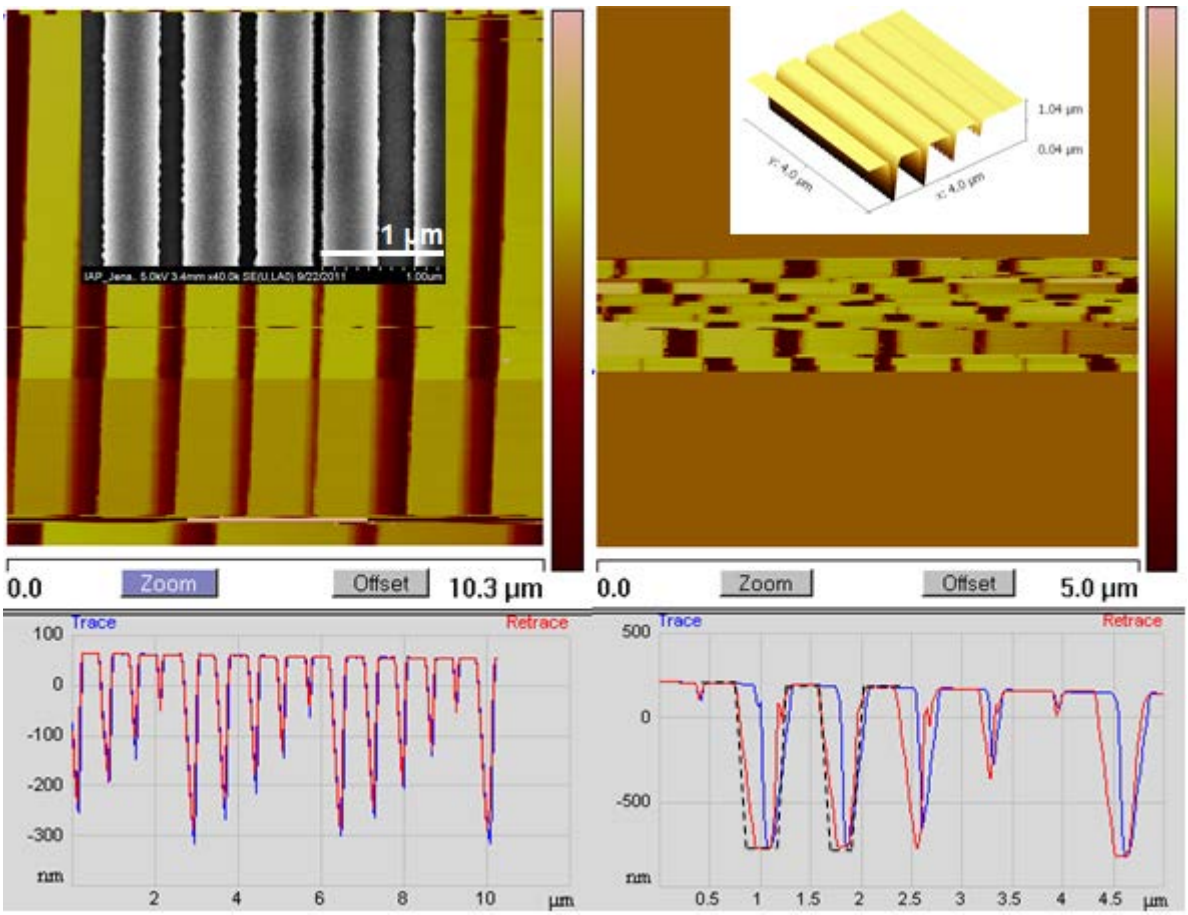

Figure 69 AFM imaging of the above sample with Veeco NanoMan: (left) standard tip cannot reach the trench bottom whereas (right) the NanoBit can the reach the bottom of 200-nm-wide trench but fails for the narrower trenches. The dashed black line shows the anticipated scan profile. The differentiation between the trace and retrace profile may indicate an unstable NanoBit. Note the difference in the scales of the scan profiles.

One important feature of the AFM tips is their durability. An AFM tip, ideally, should not show degradation or get noticeably blunt after a few scans. An easily blunting tip may provide erroneous data (compromising the reliability) and may require changing on a frequent basis (time- and cost-ineffective). Although the durability of the NanoBits was not a major concern in the beginning (the NanoBits can easily be replaced

with another), long imaging tests were run to characterise the structural integrity. The experiments were carried out at NanoWorld. The imaging quality of the NanoBits was tested on different substrates (fused silica, resist) for various durations. First, a SiO_2 grating with a period of 2 µm was imaged 30 consecutive times. The line (2D) and surface (3D) scan profiles given in Figure 70 clarify that the NanoBit did not undergo any obvious blunting. Another promising result is that it remained intact in the slit without dropping or with no apparent change its orientation.

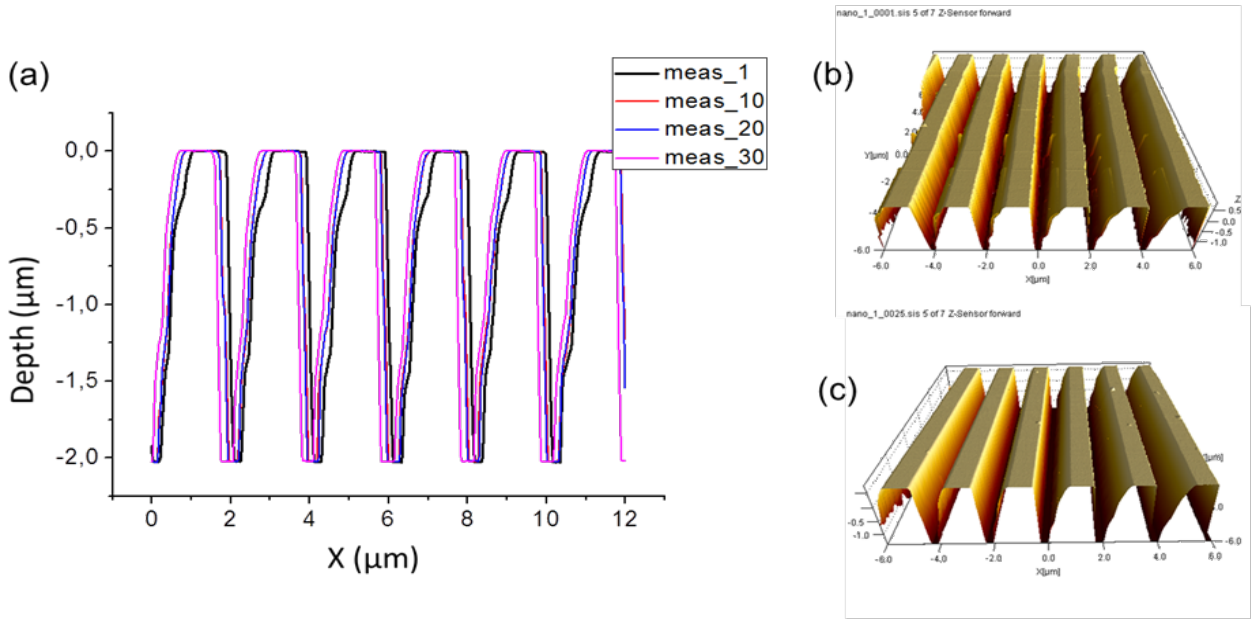

Figure 70 2-µm-period grating: (a) the substrate image profile after every 10 scans; (b) 3D picture of the 1st scan; (c) 3D picture of the 30th scan.

The second durability run used a resist with 300-nm-deep trenches. The NanoBit was used for 100 scans lasting 30 hours of AFM scanning. Comparison of the first and the hundredth line profiles indicate no performance reduction in the NanoBit, as shown in Figure 71. As a matter of fact, during the last scan, NanoBit even appears as reoriented itself slightly, fitting better to the substrate topography: trench sidewalls seem more vertical than the first scan.

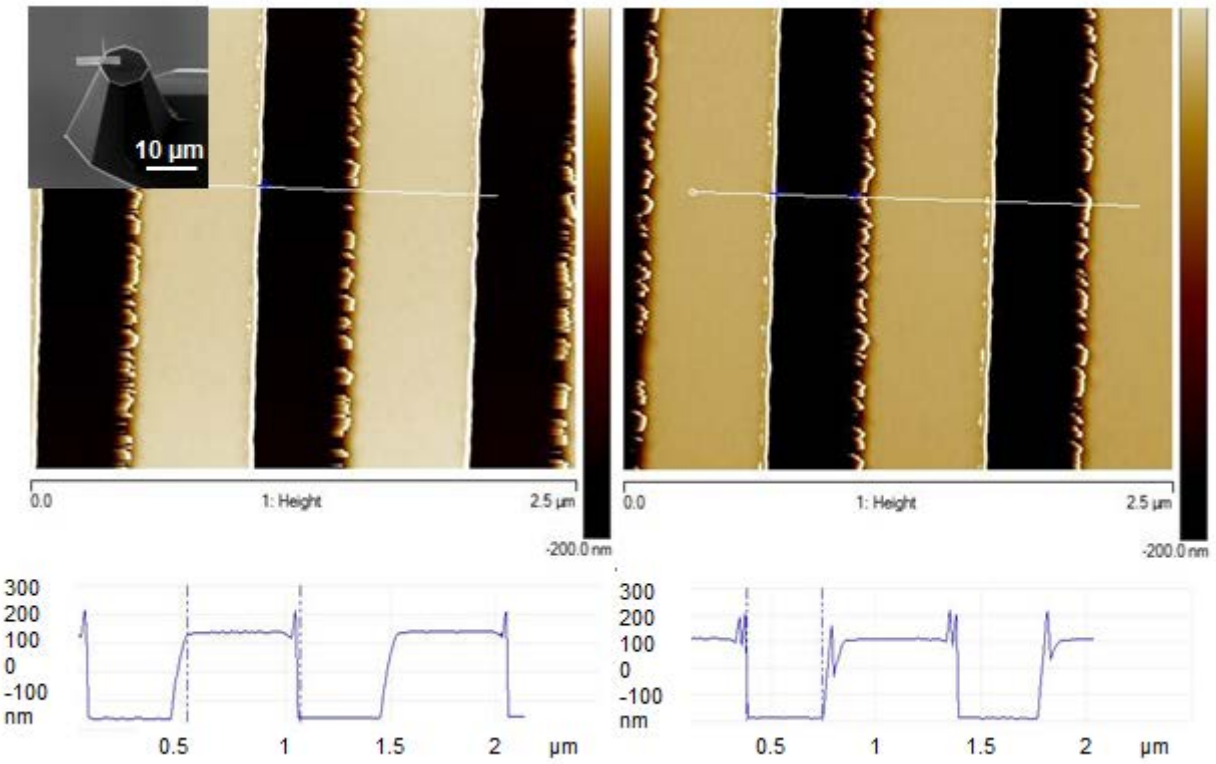

Figure 71 NanoBit durability and performance test on resist with 0.3-µm-deep trenches. 100 scans performed lasting 30 hours. 1st scan profile (left) is preserved during the 100th scan (right). The inset shows the NanoBit used.

The performance of the NanoBit and the data it provides depend very much on the level of misalignment into the probe slit. In the above cases, NanoBits were rather well aligned in general, thus delivering reliable data and showing a stable performance. The perfect alignment requires fulfilment of two angular criteria: a tip (or NanoBit in the slit)

- should be positioned with a certain angle to the cantilever plane in longitudinal direction ($\alpha > 0°$), and
- should be standing perfectly perpendicular to the cantilever plane in latitudinal direction ($\beta = 0°$).

These angles along with exemplary assembled NanoBits are provided in Figure 72. The angle α is determined by the type and brand of the AFMs, and commonly $7° < \alpha < 12°$. For instance, while the AFM used at OFFIS manufactured by JPK requires $\alpha = 7°$, Veeco NanoMan requires $\alpha = 12°$ for the scanning to be oriented perfectly perpendicular to the substrate surface. The microrobot actuator of NanoLab that the AFM probe fixated on is tilted by this specific angle before the NanoBit is collected. Therefore, it is important to acknowledge the specific AFM to be used for imaging before mounting the NanoBit. On the other hand, β needs to be zero regardless of the AFM setup. This is more challenging from the assembly and usage point of view because the slits on the AFM probe are milled by FIB. FIB milling results in Gaussian profile of the slit due to Gaussian intensity profile of the incident beam. This fact imposes two possible risks: (i) since the slit is wider at the surface, it is possible for NanoBit to deflect during scanning if it is not bonded strongly enough at the slit bottom (or if the slit is relatively shallow), and (ii) if the slit bottom or the channel along its depth is not symmetric, the NanoBit may sit in a tilted position rather than straight

up. To eliminate these risks, the slits need milling sufficiently deep with preferably flat bottoms or straight sidewalls such that the NanoBit could be fastened strongly enough.

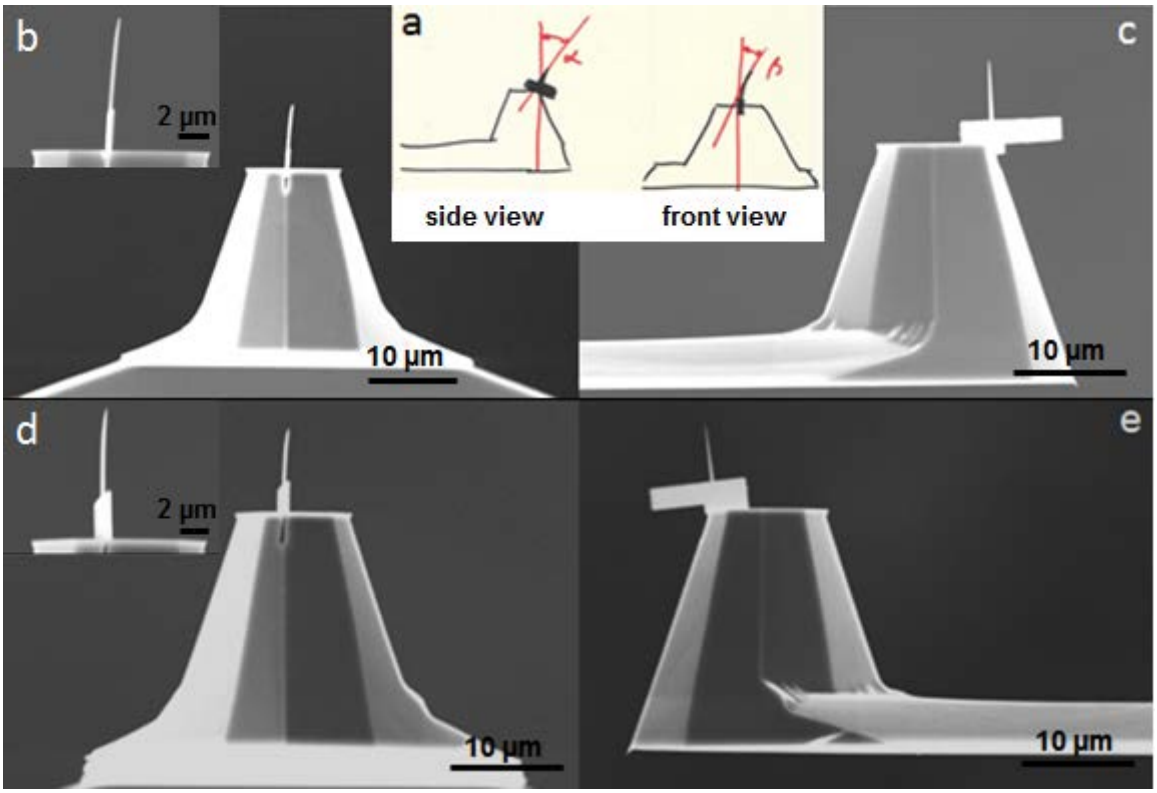

Figure 72 Reliable AFM imaging requires perfect alignment of the scanning probe (tip). Tilting of the tip may occur in (a) longitudinal or latitudinal directions. Misalignment in both directions (b-c) provides poor or erroneous data. The alignment requires α = 7–12° and β = 0 (d-e).

The scan profile attained by a misaligned HAR NanoBit and a commercial AFM tip (M1) [93], purchased from Nanotools, are shown in Figure 73. The uneven topography of the quartz grating was well imaged by M1 tip. However, the NanoBit was obvious to be tilted either during assembly or, more likely, during the scanning. Although the NanoBit was also able to reach the trench bottom, it lacked in providing a satisfactory data because of tilting (compare Figure 73(a-b)). In Figure 73(c), the exemplary scan profiles are sketched based on the quality of alignment and the tips.

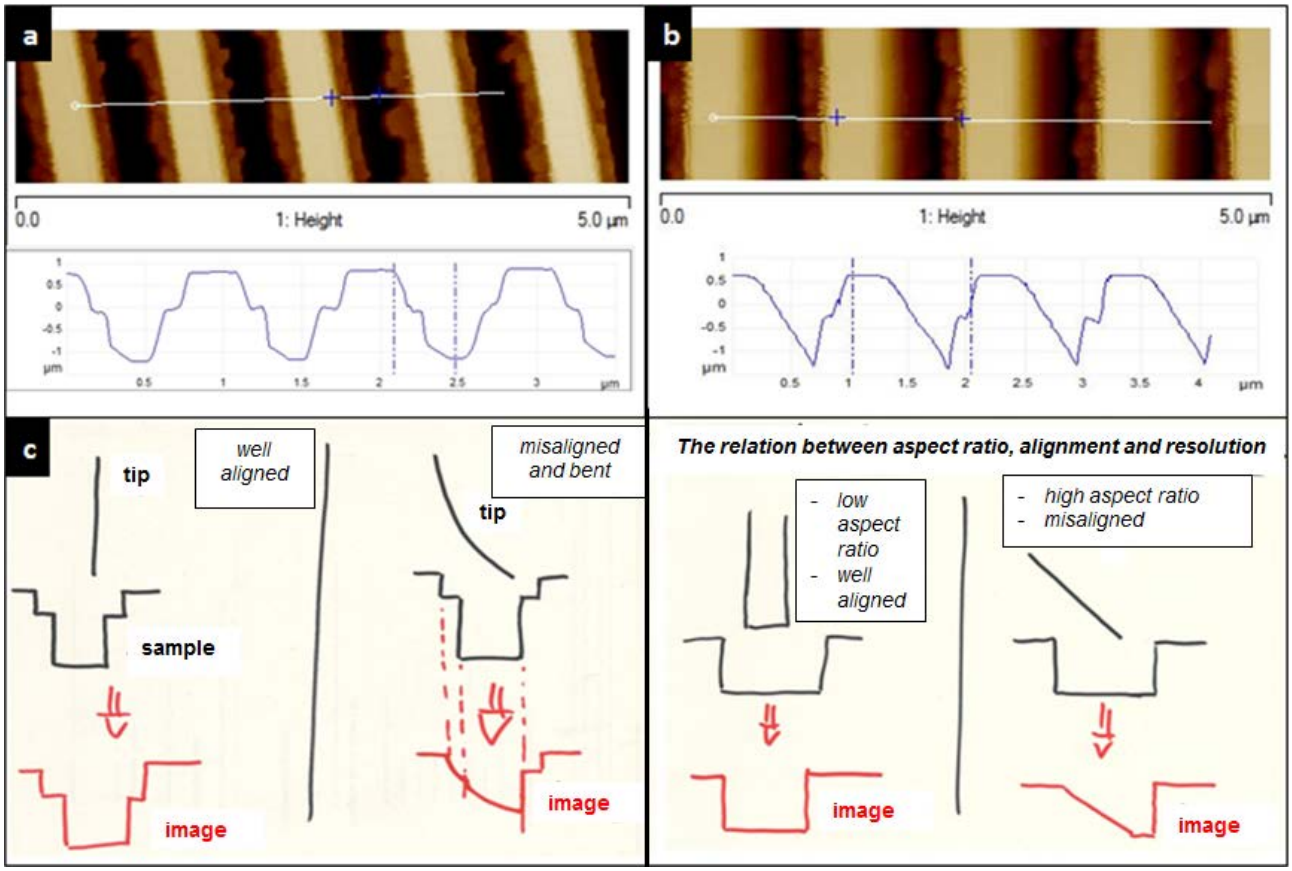

Figure 73 A quartz grating with 2-µm-deep trenches measured by (a) a commercial AFM tip (Nanotool M1) and (b) a NanoBit. Scan data obtained by NanoBit clearly indicates that it is misaligned during assembly.

The obtained AFM scan image reflects the interaction between the AFM tip and the sample under investigation. When the sample surface features are laterally large and short AFM tips can provide sufficiently accurate results. However, as the region of interest has structures with higher AR than that of the AFM tip, the tip cannot penetrate the well bottom or cannot image the sidewalls appropriately, and the resultant profile is the geometrical image of the tip. This imaging artefact is called *tip convolution* or *tip imaging*. Figure 74(a-b) shows the images produced by two tips with different morphologies and aspect ratios. HAR tips help imaging deep trenches and tall structures while greatly reducing the imprecision of the linewidths, but still cannot provide the exact sidewall angle due to its tapered shape. Therefore, one can expect to deduce only the maximum post width and/or minimum trench width. The pitch and the step height measurements remain unaffected whereas the linewidth values are offset by the width of the scanning probe [46, 92].

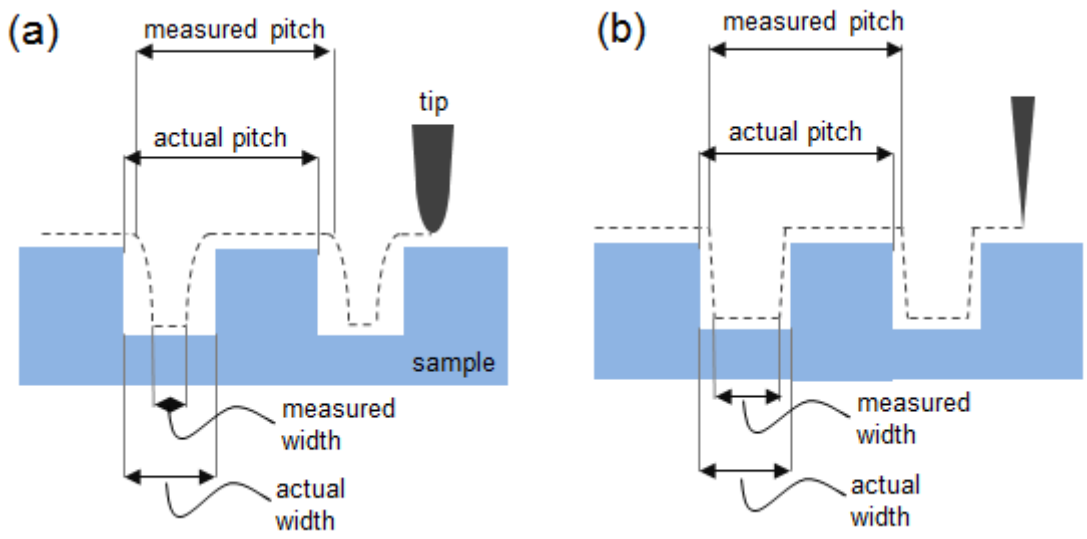

Figure 74 The AFM scans of the sample with step topography. The scan profiles reflect the scanning probe geometries of (a) conical and (b) HAR tips. The measured and actual widths of the trenches and posts differ for different tips whereas the pitch and step height remains the same given that the tip reaches the trench bottom.

To restore the actual sample topography, the errors imposed by the geometrical shape of the tip can be removed, which is called *deconvolution*. As can be seen in Figure 74(a-b), the scan image of the substrate represents the inverted shape of the scanning probe tip. Deconvolution takes into account the tip shape and removes the geometrical artefact caused by this shape. While the well-known tip shapes can be processed readily, more challenging and uncommon tips can be characterised by specially manufactured samples, called *probe-tip characterisers* [46]. The tip shape is then input to the algorithm used for deconvolution, and extracted from the raw image. A thorough study of image reconstruction was conducted by Villarrubia using the set theory, and the complex algorithm created for deconvolution is published to serve as a guide [94].

At the time of this work project, the sidewall scanning mode was not developed entirely; therefore CD-AFM measurements could not be carried out.

6.4. Discussion and conclusions

The fabricated NanoBits were assembled and their performances as AFM probes were tested. The assembly of the NanoBits was carried out in an FIB-SEM dual beam system, using a nanorobotic system, NanoLab. The NanoBits were successfully picked up by the microgripper and collected in a cartridge. During this process, the microgripper was observed to grab and turn the NanoBits as intended (facing downward) when tilted by 10°–20° whereas slanted gripper end-effector failed occasionally in proper pick-up of the tips. Initially designed cavities in the cartridge were 350-nm-wide and presented difficulties while insertion of the NanoBits, such as aligning of the tip and stiction of NanoBit to the cavity sidewalls. The later cavity design features 1 µm × 1 µm aperture on the topside and a conical opening on the back. By this way, the tips were easily accommodated in the cartridge and it was ensured that their possible movement in the

cavity would not damage any critical parts. From both cartridges the AFM probe picked up the NanoBit successfully.

By the time the NanoBits project terminated the development of the sidewall scanning mode (CD-AFM mode) was not finalised. Assembled HAR NanoBits were used for testing their performance by imaging optical gratings with DT topography. In most cases, the NanoBits showed better performance than the standard pyramid AFM probes. However, it was clear that the alignment of the tips while mounting to the AFM probe should be carried out with care. The tilt angle of the NanoBit with respect to probe cantilever plane should follow specific AFM requirements, and the NanoBit (or the very tip) should not be leaning towards one side. Scan trials clearly showed that the misaligned NanoBits perform poorly despite their well-defined structure and dimensions. On the other hand, long scan experiments proved that (i) the NanoBits did not get blunt even after 100 scans (continuous 30 h imaging), and (ii) stiction into the slit on the plateau tip was sufficiently strong since none of the tried NanoBits dropped either during or after the scanning.

7 Conclusion

During this PhD project, NanoBits (exchangeable scanning probe microscopy tips) were fabricated by lateral nanolithography: focused ion beam milling of freestanding NEMbranes and by microfabrication, where the NanoBits and hybrid structures were defined by electron beam lithography. These tips were successfully installed on a nanorobotic system for manipulation. Assembly of NanoBits was achieved by using a microgripper as an intermediary tool to pick up the NanoBits and place them into the dedicated cavities of a cartridge, which served as a NanoBit library. Mounting of NanoBits to an AFM probe was demonstrated and AFM scans performed. During imaging, the tips displayed comparably good and in some cases better performances, showing no noticeable degradation in profile or scan quality after long scanning tests.

In the following, obtained results are presented and discussed in more detail:

The design of the NanoBits considered topographically challenging application topographies like deep trench and critical dimensions. Therefore, tips suitable for imaging high-aspect ratio structures and sidewall profiles were designed. In the designing of NanoBits, realistic manipulation scenarios, material reliability, and requirements set by NanoBits project partners such as connector platform, aspect ratio, sharpness and so on, as well as early experiments with FIB-milled NanoBits played a prominent role. Actual NanoBits were designed to protrude from an edge of a freestanding NEMbrane to allow maximum degree of accessibility.

NanoBits were realised by two methods: FIB milling and microfabrication. FIB milling mainly aimed at fabrication of prototypical NanoBits to envision the critical parameters in terms of both design and the manipulation. To prevent the defect formation (e.g. blobs) and minimise the stage drift, previously developed smart milling strategies were used and further improved. Using these strategies, with FIB milling, a tip sharpness comparable to what can be achieved by EBL (≤30 nm) was aimed, and eventually, tip diameters in the order of 30 nm were regularly obtained whereas the smallest tip diameter achieved was <15 nm, with aspect ratios of 45 possible.

For the microfabrication of the tips process steps were kept as standard as possible, which included photolithography, dry and chemical etching, and deposition systems (LPCVD, electron-beam deposition of metal). NanoBits, however, were defined by high-end 100 keV JEOL JBX9500FSZ electron beam writer with a Schottky filament, which is not a common tool in the cleanrooms nor can it be claimed as cheap. Still,

when the writing time per NanoBit (>10,000/30 min) is taken into account, the cost of a NanoBit can be argued as small. As NanoBit material 200-nm-thick pSi was used since (i) single crystal-SOIs with thin (≤200 nm) device layers are neither perfectly uniform in their thickness nor are easy to purchase in small numbers, and (ii) pSi has almost as good mechanical properties as scSi. The end-products were realised extending from the NEMbrane edge with a yield of ∼90% with no visible deformations or damage. The remainder were observed to possess small cracks in the center or sides along the width where NEMbrane protrudes from the microchip. Scanning electron microscope investigation showed that the NanoBits had wedge sidewalls; that is, the feature sizes increased along the thickness of the NanoBit. Although this widening was relatively insignificant for NanoBit body parts (<1%), the very tip diameters of side-tips and cross-shaped tips increased from ∼30 nm to ∼275 nm while the increase for HAR (tapered) tips were smaller: from ∼15 nm to ∼120 nm. Measurements of the critical parameters were carried out by contrasting and averaging the results from software measurement tools and electron signal intensity profile along the cross-section of the specific location. The widening of the structure very likely occurred during the pattern transfer via RIE. Biasing of the process parameters towards the physical etch should provide more vertical sidewalls, even underetching of the pSi layer can be pursued granted that the operator pays careful attention to not sputter all masking material (lift-off metal) or to not etch whole pSi device layer.

Since pSi is not globally anisotropic, post-processing sharpening of the microfabricated NanoBits was tested by physical etching methods: reactive ion etching, ion beam etching, and FIB milling. RIE results were promising etching the widened tip bottom and therefore increasing the overall tip sharpness. IBE experiments were inconclusive since the chips needs to be glued to carried wafer by CrystalBond™ and NanoBits sink in the glue precluding any etch process. FIB milling also showed good result using the hybrid structures: tip diameters ∼40 nm were achieved; however, further sharpening leads to artefact formation and bending of the very tip. In terms of batch-processing, when carefully conducted, the first two methods could prove viable options whereas FIB is a serial process, and thus, is a low throughput method although it can provide sufficiently small tip diameters.

Out-of-plane bending of NanoBits from their lateral plane to ∼90° would allow riddance of the intermediary tools like microgripper and cartridge, hence NanoBits could be picked up directly by the AFM probe, which in turn would accelerate the assembly process. FIB irradiation of NanoBit-like Si_xN_y cantilevers showed that as the substrate thins down to 80–90 nm, the bending starts. Control of the dose results in controllable bending angle; bending angle was observed to overshoot the right angle (>90°) at higher doses. Actual NanoBits were shown to bend close to 90° and to a certain degree window (30°–60°). These NanoBits can be assembled by the AFM probe with a specially designed slit approaching from the respective direction.

Despite promising bending results obtained by FIB exposure, it requires serial treatment of the structures. Second method used to bend the NanoBits was the residual stress built up in bimorph structures, which can result in bending of whole NanoBit library to a desired level. 200-nm-thick freestanding NanoBit NEMbranes were deposited 25–125 nm Ni; radii of curvatures and tip angles of the bent structures were measured, and compared to the extended Stoney equation developed by L. B. Freund. Tip angles varied from ∼25° to ∼130°. 75 nm Ni deposition on 200 nm pSi resulted in 90° bending of the NEMbranes, aligning NanoBits vertically. The theoretical model showed high correlation with the experimental results, but failed in estimating the bending degree especially for low metal thicknesses (<50 nm). This discrepancy can be

attributed to the island formations of the film during the initial stages of deposition, because the theory assumes uniform films for all thicknesses. Analyses and experiments with different materials showed that the main driving force for the bilayer bending is the intrinsic stress built up in the system. Building stress, however, should be simultaneously bending the NEMbrane during deposition, which should show itself in uneven metal film deposition on the topside as well as a deposited layer on the back. SEM inspections provided no signs of the either. That is, the growth stresses may be playing the prominent role in bending of the bilayer structure while the thermal stresses contribute to further bending in the form temperature elevation of the substrate and/or the deposition chamber. Eventually, stress formation in the films is complex issue and bending was observed as not easily controllable. Although the desired degree of bending cannot be attained after the metal deposition, it was demonstrated that the tip angle can be fine-tuned by thermal actuation. Up to 150°C, the bending is reversible and the NanoBits' angle can be modified within ±10°. At higher temperatures reversal of stress from tensile to compressive, buckling, and changing of surface colour were observed, pointing to silicidation of the structure which may be starting already at 170°C.

The fabricated NanoBits were assembled and their performance as AFM probes tested at OFFIS. The assembly of the NanoBits was carried in a FIB-SEM dual beam system, using a nanorobotic system, NanoLab. The NanoBits were successfully picked up by the microgripper and collected in a cartridge. During this process, the microgripper was observed to grab and turn the NanoBits as intended (facing downward) when tilted by 10°–20° whereas slanted gripper end-effector failed occasionally in proper pick-up of the tips. Initially designed cavities in the cartridge were 350-nm-wide and presented difficulties while insertion of the NanoBits, such as aligning of the tip and stiction of NanoBit to the cavity sidewalls. Later design features 1 µm × 1 µm aperture on the topside and a conical opening on the back. By this way, the tips were easily accommodated in the cartridge and it was ensured that their possible movement in the cavity would not damage any critical parts. From both cartridges the AFM probe picked up the NanoBit successfully.

By the time this project terminated the sidewall scanning (CD-AFM mode) was not possible. Assembled HAR NanoBits were used for testing their performance by imaging optical gratings with DT topography. In most cases, the NanoBits showed better performance than the standard pyramid AFM probes. However, it was clear that the alignment of the tips while mounting to the AFM probe should be carried out with care. The tilt angle of the NanoBit with respect to probe cantilever plane should follow specific AFM requirements, and the NanoBit (or the very tip) should not be leaning towards one side. Scan trials clearly showed that the misaligned NanoBits perform poorly despite their well-defined structure and dimensions. On the other hand, long scan experiments proved that (i) the NanoBits did not get blunt even after 100 scans (continuous 30 h imaging), and (ii) stiction into the slit on the plateau tip was sufficiently strong since none of the tried NanoBits dropped either during or after the scanning.

Conclusively, NanoBits pose as promising candidates for exchangeable and replaceable scanning probe microscope tips. The SPM required to image challenging topographies like deep trenches, vias, sidewall or linewidth roughness are fabricated by means of vertical production. Lateral nanolithography can allow reduction of production costs as well as batch fabrication of these tips in great numbers. With focused ion beam milling and electron beam lithography-assisted microfabrication, tips that had approximate sharpness to and higher aspect ratios than the commercially available tips were fabricated. Low throughput of FIB milling can be compensated by microfabrication of the tips. In this work, the NanoBits were observed

to lose their fine feature sizes along the thickness, which can be circumvented by (i) using thinner device layers with improved mechanical properties (silicon carbide, silicon nitride, titanium, or even diamond-like-carbon), (ii) physical etching-biased pattern transfer, and (iii) final anisotropic etching of the structure (in the case of silicon use). Currently, the NanoBits can be assembled and mounted on an AFM probe repeatedly and reproducibly using a microgipper as the intermediary tool. Bending the NanoBits perpendicular to their fabricated lateral plane can eliminate the gripper from manipulation scenario. However, the stress-driven bending is a complex mechanism since it depends on many factors, and therefore, is difficult to control. NanoBit bent by various degrees, nevertheless, can be picked up by specially shaped AFM probes that have the appropriate slits. However, optimisation studies remain as a necessity for the bent NanoBits on the grounds of their critical parameters, such as break-point, tip position and tip orientation. The NanoBits proved to perform better than the standard pyramid AFM probes in terms of both imaging and durability given that they are properly aligned for the AFM they will be used in. The alignment issue can be overcome by milling deeper slits into the plateau cantilevers and performing electron beam-induced deposition to glue the NanoBit into the slit. Eventually, when production is further optimised and manipulation techniques finalised, NanoBits can offer an unprecedented freedom in adapting to ever-altering surface topographies providing fast exchangeability and reliable outcome owing to their low-cost production (per NanoBit) and versatile capabilities.

APPENDIX. Polysilicon NanoBits process flow

	Process steps	Process description	Sketch of the process
1.	Starting material	PolySi/SiO2/Si wafer, Thicknesses: pSi: 200 nm Buried oxide: 0.95 µm Handle Si: 525±25 µm Handle layer: 4" SSP Si <100>, p-type (boron), 1-20 Ω.cm # wafer: 5	
2.	e-beam resist coating	e-beam resist: ZEP520A Spinner: **SSE/Manual spinner** Resist type: positive Thickness: 180 nm RPM: 1500 Bake at 160 °C for 2 min # wafer: 1* **(Here, and where else single wafer is indicated, the wafer will used so as to test the feasibility of procedure. If the outcome reveals satisfactory, remaining wafers will follow same parameters/step(s).)*</br>	
3.	e-beam lithography	**JEOL e-beam writer** Energy: 100 kV Current: 0.8 nA Dose: 300–350 µC/cm2 # wafer: 1	

4.	Resist develop	Developer: ZED-N50 Time: 2 min Isopropanol: 30 s Blow-dry with N_2 gun Water # wafer: 1	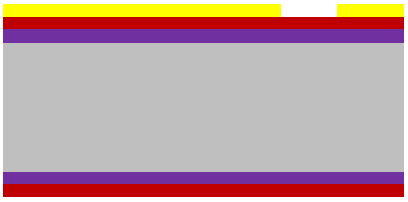
5.	Inspection	Optical microscope (OM), SEM and Dektak	
6.	Metal deposition	**Wordentec**: e-beam evaporation Metal: Cr Thickness: 20±2 nm Deposition rate: 5 Å/s # wafer: 1	
7.	Inspection	OM	
8.	Lift-off	S1165: iteratively until no visible metal particle remains Ultrasound: 5 W, 2 min Water rinse # wafer: 1	
9.	Inspection	OM *Do successive lift-offs if ZEP is not rinsed away.*	
10.	Photolithography resist coating	**HMDS** treatment Resist: positive AZ5214E **SSE Spinner** Resist thickness: 1.5 µm	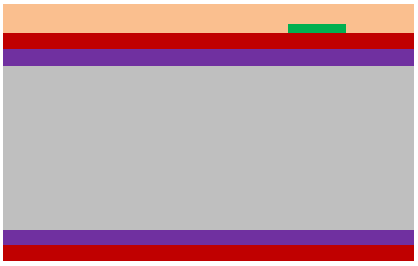

11. Photolithography	**EVG 6" Aligner** Top-side alignment Contact mode: Hard contact Alignment gap: 30 µm Exposure time: 3 s	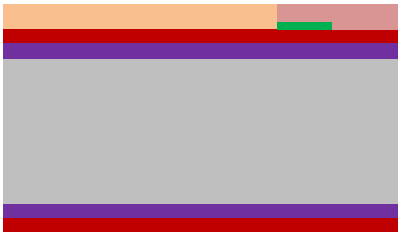
12. Resist development	Developer: AZ351B:DI-water (1:4) Time: 70 s Water rinse: >4 min Spin-dry	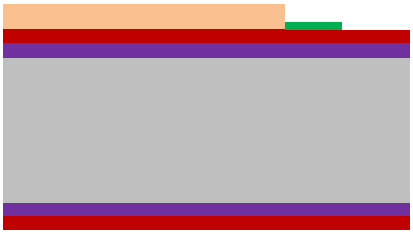
13. Directional pSi etching	**ICP Metal** O_2 clean: 10 min Recipe: pxsimicrotry3 Time: 3 min (switch on end-point detection (EPD)) Targeted thickness: 200+10 nm # wafer: 1	
14. Inspection	OM and SEM	
15. UV resist strip	**Acetone bath** Time: 40 min Bubbler: 4 min Spin-dry	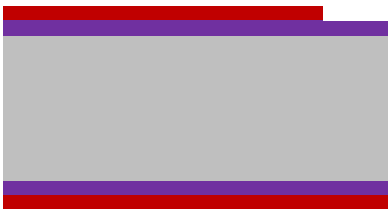
16. UV resist strip 2	**7-up mask clean** Time: 10 min @80°C Bubbler: 5 min	
17. Wet metal (Cr) etch	Time: 70 s Bubbler: 3 min Spin-dry	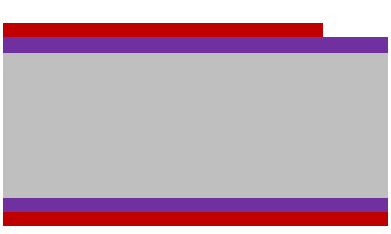
18. RCA clean	RCA clean without BHF	

19.	Inspection	OM (and Dektak)
20.	Cleaning	**RCA** without HF bath 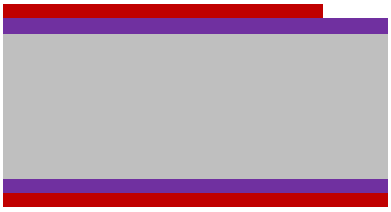
21.	Front-side protection	**SSE spinner** PR thickness: 2.2 µm 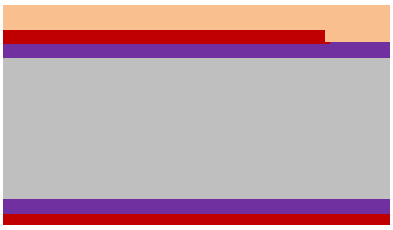
22.	Etch layers on the backside	**RIE 1** Recipe: bge-nitr Time: 20 min 
23.	UV resist strip	**Plasma asher** Time: 45 min O_2: 400 mL/min N_2: 70 mL/min Power: 1000 W 
24.	Total etching of backside oxide	**KOH bath** Rinse bath: 30 s BHF: 20 s
25.	Protective layer deposition	Material: Si-rich low-stress Si_xN_y Thickness: 200±10 nm **LPCVD** Recipe: SIRICH Time: 37 min Temperature: 835 C Pressure: 112 mTorr DCS flow: 93 sccm NH_3 flow: 13 sccm 
26.	UV resist coating	HMDS treatment Resist: positive AZ5214 Frontside: 1.5 µm Backside: 1.5 µm (proximity bake) 

27. Photolithography	**SSE aligner** Back-side alignment Contact mode: Hard contact Alignment gap: 30 µm Exposure time: 3 s	
28. UV resist development & directional nitride etch	Developer: AZ351B:DI-water (1:4) Time: 70 s Water rinse: >4 min Spin-dry **Plasma asher (descum)** Time: 10 s **Hot oven** Temperature: 120°C Time: ~10 min *(harden the resist)* **RIE2** Recipe: bge-nitr Time: 6 min Etch rate: 35–40 nm/min	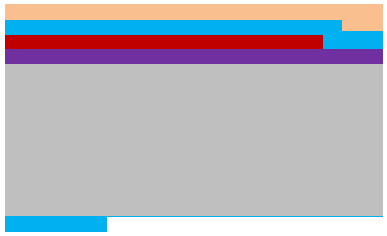
29. UV resist strip	**Plasma asher** Time: 50 min	
30. Chip release	**KOH bath** (28 wt%) Temperature: 80°C Etch rate: 1.25-1.35 µm/min Time: ~6.5 h *(check the process every 1 hour)*	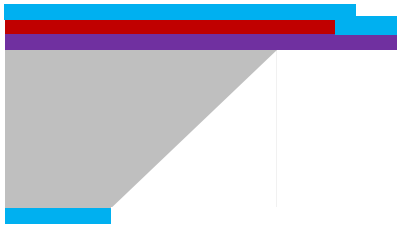
31. Inspection	OM *Check and make sure all devices/chips are defined*	

32. Silicon nitride wet etch	Phosphoric acid (H_3PO_4) Temperature: 180 °C Etch rate: ~6 nm/min Time: 80+10 min	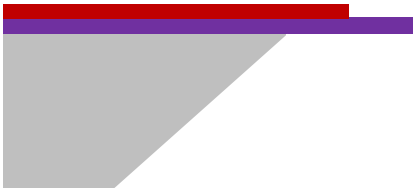
33. Isotropic oxide etch	BHF in KOH3 Targeted thickness: 1+ *µ*m Etch rate: ~75 nm/min Time: 15 min *(make sure all chips are released and intact)* # wafer: 1	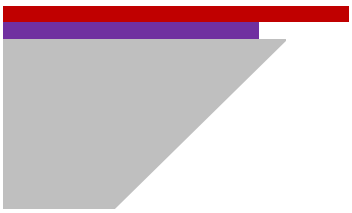
34. Inspection	OM and SEM *Structures need to be suspending. If not, further dip wafer into BHF for small time intervals (10-15 s).*	

References

1. Bhushan, B., H. Fuchs, and M. Tomitori, *Applied Scanning Probe Methods VIII – Scanning Probe Microscopy Techniques*. NanoScience and Technology. 2008, Heidelberg, Germany: Springer-Verlag.
2. International Technology Roadmap for Semiconductors (ITRS). 2005; Available from: http://www.itrs.net/Links/2005ITRS/Home2005.htm.
3. Binnig, G., C.F. Quate, and C. Gerber, *Atomic Force Microscope.* Physical Review Letters, 1986. **56**(9): p. 930-933.
4. Binnig, G., et al., *Surface Studies by Scanning Tunneling Microscopy.* Physical Review Letters, 1982. **49**(1): p. 57-61.
5. Danzebrink, H.U., et al., *Advances in Scanning Force Microscopy for Dimensional Metrology.* CIRP Annals - Manufacturing Technology, 2006. **55**(2): p. 841-878.
6. *Dekker Encyclopedia of Nanoscience and Nanotechnology - Six Volume Set (Print Version)*, J.A. Schwarz and C.I. Contescu, Editors. 2004, CRC Press.
7. Dixson, R., et al. *CD-AFM reference metrology at NIST and SEMATECH*. 2005.
8. Liu, H.-C., G.A. Dahlen, and J.R. Osborne, *Critical Dimension Atomic Force Microscopy for Sub-50-nm Microelectronics Technology Nodes*, in *Applied Scanning Probe Methods VIII*, B. Bhushan, H. Fuchs, and M. Tomitori, Editors. 2008, Springer Berlin Heidelberg. p. 31-75.
9. Dai, G., et al., *Development of a 3D-AFM for true 3D measurements of nanostructures.* Measurement Science and Technology, 2011. **22**(9): p. 094009.
10. International Technology Roadmap for Semiconductors (ITRS). 2013; Available from: http://www.itrs.net/Links/2013ITRS/Home2013.htm.
11. NANOSENSORS™. *NanoSensors*. 2014; Available from: http://www.nanosensors.com.
12. Team Nanotec GmbH. *Team Nanotec, Micro- and Nanofabrication Technology*. 2014; Available from: http://www.team-nanotec.de/.
13. nanotools GmbH. *Nanotools*. 2014; Available from: http://www.nanotools.com/home.html.
14. Liu, H., et al., *Advanced atomic force microscopy probes: Wear resistant designs.* Journal of Vacuum Science & Technology B: Microelectronics and Nanometer Structures, 2005. **23**(6): p. 3090-3093.
15. Dahlen, G., et al., *Tip characterization and surface reconstruction of complex structures with critical dimension atomic force microscopy.* Journal of Vacuum Science & Technology B, 2005. **23**(6): p. 2297-2303.
16. International Technology Roadmap for Semiconductors (ITRS). 2010; Available from: http://www.itrs.net/Links/2010ITRS/Home2010.htm.
17. Kumar, R.T.R., et al., *Nanobits: customizable scanning probe tips.* Nanotechnology, 2009. **20**(39): p. 395703.
18. Ansel, Y., et al., *Development of tools for handling and assembling microcomponents.* Journal of Micromechanics and Microengineering, 2002. **12**(4): p. 430.
19. Greitmann, G. and R.A. Buser, *Tactile microgripper for automated handling of microparts.* Sensors and Actuators A: Physical, 1996. **53**(1–3): p. 410-415.
20. Boggild, P., et al. *Customizable nanotweezers for manipulation of free-standing nanostructures*. in *Nanotechnology, 2001. IEEE-NANO 2001. Proceedings of the 2001 1st IEEE Conference on*. 2001.
21. Mølhave, K., et al., *Towards Pick-and-Place Assembly of Nanostructures.* Journal of Nanoscience and Nanotechnology, 2004. **4**(3): p. 279-282.
22. Guckel, H., et al. *Thermo-magnetic metal flexure actuators*. in *Solid-State Sensor and Actuator Workshop, 1992. 5th Technical Digest., IEEE*. 1992.
23. Mølhave, K. and O. Hansen, *Electro-thermally actuated microgrippers with integrated force-feedback.* Journal of Micromechanics and Microengineering, 2005. **15**(6): p. 1265.
24. Carlson, K., et al., *A carbon nanofibre scanning probe assembled using an electrothermal microgripper.* Nanotechnology, 2007. **18**(34): p. 345501.

25. Kim, P. and C.M. Lieber, *Nanotube Nanotweezers.* Science, 1999. **286**(5447): p. 2148-2150.
26. Akita, S., et al., *Nanotweezers consisting of carbon nanotubes operating in an atomic force microscope.* Applied Physics Letters, 2001. **79**(11): p. 1691-1693.
27. NANOSENSORS™, *AdvancedTEC™ Silicon-SPM-Probes, Advanced Tip at the End of the Cantilever*. 2002, NanoWorld AG: Neuchâtel, Switzerland.
28. Bartenwerfer, M., et al. *Automated handling and assembly of customizable AFM-tips*. in *Assembly and Manufacturing (ISAM), 2011 IEEE International Symposium on*. 2011.
29. van Honschoten J.W., et al., *Elastocapillary fabrication of three-dimensional microstructures.* Applied Physics Letters,, 2010. **97**: p. 014103.
30. Freund L.B. and Suresh S., *Thin Film Materials: Stress, Defect Formation and Surface Evolution*. 2003, New York: Cambridge University Press.
31. Thornton, J.A. and D.W. Hoffman, *Stress-related effects in thin films.* Thin Solid Films, 1989. **171**(1): p. 5-31.
32. Savenko, A., I. Yildiz, and P. Bøggild, *Out-of-plane bending based on SiN-ion-irradiation and bilayer structures for easy access for micromanipulation.* Microelectronic Engineering, 2013. **110**(0): p. 398-402.
33. Malm, B., et al., *Optimization of FIB milling for rapid NEMS prototyping.* Microelectronic Engineering, 2011. **88**(8): p. 2671-2674.
34. McCord, M.A. and M.J. Rooks, *Electron Beam Lithography*, in *Handbook of Microlithography, Micromachining, and Microfabrication. Volume 1: Microlithography*, P. Rai-Choudhury, Editor. 1997, SPIE Press: Bellingham, Washington. p. 139-251.
35. Seo, E., B.K. Choi, and O. Kim, *Determination of proximity effect parameters and the shape bias parameter in electron beam lithography.* Microelectronic Engineering, 2000. **53**(1–4): p. 305-308.
36. Owen, G., *Methods for proximity effect correction in electron lithography.* Journal of Vacuum Science and Technology B, 1990. **8**(6): p. 1889-1892.
37. Haller, I., M. Hatzakis, and R. Srinivasan, *High-resolution Positive Resists for Electron-beam Exposure.* IBM Journal of Research and Development, 1968. **12**(3): p. 251-256.
38. Nishida, T., et al., *Quantum Wire Fabrication by E-Beam Elithography Using High-Resolution and High-Sensitivity E-Beam Resist ZEP-520.* Japanese Journal of Applied Physics, 1992. **31**(12S): p. 4508.
39. Zhang, J., et al., *Charging effect reduction in electron beam lithography with nA beam current.* Microelectronic Engineering, 2011. **88**(8): p. 2196-2199.
40. ZEON CORPORATION, *ZEONREX® Electronic Chemicals, High Resolution Positive Electron Beam Resist, ZEP520A Technical Report*. 2010, ZEON CORPORATION: Louisville, KY.
41. Yamaguchi, T. and H. Namatsu, *Effect of developer molecular size on roughness of dissolution front in electron-beam resist.* Journal of Vacuum Science & Technology B, 2004. **22**(3): p. 1037-1043.
42. Mohammad, M.A., et al., *Study of Development Processes for ZEP-520 as a High-Resolution Positive and Negative Tone Electron Beam Lithography Resist.* Japanese Journal of Applied Physics, 2012. **51**(6S): p. 06FC05.
43. Greeneich, J.S., *Developer Characteristics of Poly - (Methyl Methacrylate) Electron Resist.* Journal of The Electrochemical Society, 1975. **122**(7): p. 970-976.
44. Postek M.T. and Joy D.C., *Submicrometer microelectronics dimensional metrology: scanning electron microscopy.* Journal of Research of the National Bureau of Standards, 1987. **92**(3): p. 205.
45. Kanaya, K. and S. Okayama, *Penetration and energy-loss theory of electrons in solid targets.* Journal of Physics D: Applied Physics, 1972. **5**(1): p. 43.
46. Marchman H.M., et al., *Critical-Dimensional Metrology for Integrated-Circuit Technology*, in *Microlithography: Science and Technology*, Suzuki K. and Smith B.W., Editors. 2007, CRC Press Taylor & Francis Group: Boca Roton, FL.
47. Frase C.G., et al., *Analysis and Comparison of CD-SEM Edge Operators: A Contribution to Feature Width Metrology*, in *Nanoscale Calibration Standards and Methods: Dimensional and Related*

Measurements in the Micro- and Nanometer Range, Wilkening G. and K. L., Editors. 2006, Wiley-VCH: Weinheim. p. 385–403.
48. Reimer L., *Scanning Electron Microscopy — Physics of Image Formation and Microanalysis*. Springer Series in Optical Sciences, ed. Enoch J.M., et al. Vol. 45. 1985, Berlin: Springer.
49. Frase, C.G., E. Buhr, and K. Dirscherl, *CD characterization of nanostructures in SEM metrology.* Measurement Science and Technology, 2007. **18**(2): p. 510.
50. Williams, D. and C.B. Carter, *The Transmission Electron Microscope*, in *Transmission Electron Microscopy*. 1996, Springer US. p. 3-17.
51. NanoWorld Group, *Probes Catalog: Pointprobe® Non-contact / Soft Tapping Mode (NCST)*, NanoWorld Group, Editor. 2014: Neuchâtel, Switzerland.
52. Mølhave, K., et al., *Transmission Electron Microscopy Study of Individual Carbon Nanotube Breakdown Caused by Joule Heating in Air.* Nano Letters, 2006. **6**(8): p. 1663-1668.
53. Shenoy V.B. and Gracias D.H., *Self-folding thin-film materials: From nanopolyhedra to graphene origami.* MRS Bulletin, 2012. **37**: p. 847-854.
54. Boncheva, M., et al., *Magnetic self-assembly of three-dimensional surfaces from planar sheets.* Proceedings of the National Academy of Sciences of the United States of America, 2005. **102**(11): p. 3924-3929.
55. Smela, E., *Microfabricated Conjugated Polymer Actuators for Microvalves, Cell Biology, and Microrobotics*, in *Biomedical Applications of Electroactive Polymer Actuators*. 2009, John Wiley & Sons, Ltd. p. 249-264.
56. Janssen, G.C.A.M., et al., *Celebrating the 100th anniversary of the Stoney equation for film stress: Developments from polycrystalline steel strips to single crystal silicon wafers.* Thin Solid Films, 2009. **517**(6): p. 1858-1867.
57. McSkimin, H.J. and P. Andreatch, *Measurement of Third-Order Moduli of Silicon and Germanium.* Journal of Applied Physics, 1964. **35**(11): p. 3312-3319.
58. Hall, J.J., *Electronic Effects in the Elastic Constants of n-Type Silicon.* Physical Review, 1967. **161**(3): p. 756-761.
59. Stoney, G.G., *The Tension of Metallic Films Deposited by Electrolysis.* Proceedings of the Royal Society of London. Series A, 1909. **82**(553): p. 172-175.
60. Zhang, Y. and Y.-p. Zhao, *Applicability range of Stoney's formula and modified formulas for a film/substrate bilayer.* Journal of Applied Physics, 2006. **99**(5): p. -.
61. Huang, S. and X. Zhang, *Extension of the Stoney formula for film–substrate systems with gradient stress for MEMS applications.* Journal of Micromechanics and Microengineering, 2006. **16**(2): p. 382.
62. Chou, T.-L., S.-Y. Yang, and K.-N. Chiang, *Overview and applicability of residual stress estimation of film–substrate structure.* Thin Solid Films, 2011. **519**(22): p. 7883-7894.
63. Hu, Y.Y. and W.M. Huang, *Elastic and elastic-plastic analysis of multilayer thin films: Closed-form solutions.* Journal of Applied Physics, 2004. **96**(8): p. 4154-4160.
64. Freund, L.B., J.A. Floro, and E. Chason, *Extensions of the Stoney formula for substrate curvature to configurations with thin substrates or large deformations.* Applied Physics Letters, 1999. **74**(14): p. 1987-1989.
65. Klokholm, E. and B.S. Berry, *Intrinsic Stress in Evaporated Metal Films.* Journal of The Electrochemical Society, 1968. **115**(8): p. 823-826.
66. Holmström, E., et al., *Atomic-scale effects behind structural instabilities in Si lamellae during ion beam thinning.* AIP Advances, 2012. **2**(1): p. -.
67. Kim, Y.-R., et al., *Focused ion beam induced deflections of freestanding thin films.* Journal of Applied Physics, 2006. **100**(10): p. -.
68. Arora W.J., *Ph.D. Thesis*, in *Electrical Engineering*. 2008, Massachusetts Institute of Technology.

69. Bartenwerfer, M., et al. *Design of a micro-cartridge system for the robotic assembly of exchangeable AFM-probe tips*. *IEEE International Conference on Robotics and Automation (ICRA)*. 2013.
70. Ziegler J.F., *SRIM – The Stopping and Range of Ions in Matter*.
71. Madou M.J, *Fundamentals of Microfabrication: The Science of Miniaturization*. Second Edition ed. 2002, Boca Raton, FL: CRC Press LLC.
72. Hoffman, R.W., *Stresses in thin films: The relevance of grain boundaries and impurities.* Thin Solid Films, 1976. **34**(2): p. 185-190.
73. Schneider, D. and M.D. Tucker, *Non-destructive characterization and evaluation of thin films by laser-induced ultrasonic surface waves.* Thin Solid Films, 1996. **290–291**(0): p. 305-311.
74. Shackelford, J.F. and W. Alexander, *CRC Materials Science and Engineering Handbook, Third Edition*. 2000: Taylor & Francis.
75. Doljack, F.A. and R.W. Hoffman, *The origins of stress in thin nickel films.* Thin Solid Films, 1972. **12**(1): p. 71-74.
76. Hsueh, C.-H., *Modeling of elastic deformation of multilayers due to residual stresses and external bending.* Journal of Applied Physics, 2002. **91**(12): p. 9652-9656.
77. Sebag, J., et al., *Substrate temperature and strain during sputter deposition of aluminum on cast borosilicate glass in a Gemini Observatory coating chamber.* Applied Optics, 2010. **49**(24): p. 4610-4620.
78. Schulz, U., *Review of modern techniques to generate antireflective properties on thermoplastic polymers.* Applied Optics, 2006. **45**(7): p. 1608-1618.
79. Krebs, F.C., et al., *Large area plastic solar cell modules.* Materials Science and Engineering: B, 2007. **138**(2): p. 106-111.
80. Bowden, N., et al., *Spontaneous formation of ordered structures in thin films of metals supported on an elastomeric polymer.* Nature, 1998. **393**(6681): p. 146-149.
81. Cheng, L.W., et al., *Effects of stress on the formation and growth of nickel silicides in Ni thin films on (0 0 1)Si.* Materials Science and Engineering: A, 2005. **409**(1–2): p. 217-222.
82. Qin, M., M.C. Poon, and C.Y. Yuen, *A study of nickel silicide film as a mechanical material.* Sensors and Actuators A: Physical, 2000. **87**(1–2): p. 90-95.
83. Deng, F., et al., *Salicidation process using NiSi and its device application.* Journal of Applied Physics, 1997. **81**(12): p. 8047-8051.
84. Tinani, M., et al., *In situ real-time studies of nickel silicide phase formation.* Journal of Vacuum Science and Technology B, 2001. **19**(2): p. 376-383.
85. Sasaki, T., et al. *Raman Study of Low-Temperature Formation of Nickel Silicide Layers*. in *Advanced Thermal Processing of Semiconductors, 2006. RTP '06. 14th IEEE International Conference on*. 2006.
86. Lauwers, A., et al., *Low temperature spike anneal for Ni-silicide formation.* Microelectronic Engineering, 2004. **76**(1–4): p. 303-310.
87. Lavoie, C., et al., *Towards implementation of a nickel silicide process for CMOS technologies.* Microelectronic Engineering, 2003. **70**(2–4): p. 144-157.
88. Hu, Y. and S.P. Tay, *Spectroscopic ellipsometry investigation of nickel silicide formation by rapid thermal process.* Journal of Vacuum Science and Technology A, 1998. **16**(3): p. 1820-1824.
89. Eichhorn, V., et al. *NanoLab: A nanorobotic system for automated pick-and-place handling and characterization of CNTs*. in *Robotics and Automation, 2009. ICRA '09. IEEE International Conference on*. 2009.
90. Becker, M., et al., *Cantilever Based Connector Platform for Exchangeable and Customizable Scanning Probe Tips.* Procedia Engineering, 2012. **47**(0): p. 220-223.
91. Diederichs, C., et al. *A Rapid Automation Framework for Applications on the Micro- and Nanoscale*. in *Australasian Conference on Robotics and Automation*. 2013. Sydney Australia.
92. Howland, R. and L. Benatar, *A Practical Guide to Scanning Probe Microscopy*. 1998: DIANE Publishing Company.

93. Nanotools GmbH, *M1, Extreme Aspect Ratio*, N. GmbH, Editor. 2014: München.
94. Villarrubia, J.S., *Algorithms for Scanned Probe Microscope Image Simulation, Surface Reconstruction, and Tip Estimation.* Journal of Research of the National Bureau of Standards and Technology, 1997. **102**(4).

List of publications

1. A. Savenko, **I. Yildiz**, and P. Bøggild; *Out-of-plane bending based on SiN-ion-irradiation and bilayer structures for easy access for micromanipulation.* Microelectronic Engineering, 2013. **110**(0): p. 398-402.
2. A. Savenko, **I. Yildiz**, D. H. Petersen, P. Bøggild, M. Bartenwerfer, F. Krohs, M. Oliva and Torsten Harzendorf; *Ultra-high aspect ratio replaceable AFM tips using deformation-suppressed focused ion beam milling*. Nanotechnology, 2013. **24**(46): 465701.
3. M. Bartenwerfer, V. Eichhorn, S. Fatikow, M. Becker, A. Savenko, **I. Yildiz**, P. Bøggild; *Design of a Micro-Cartridge System for the Robotic Assembly of Exchangeable AFM-Probe Tips*. IEEE International Conference on Robotics and Automation (ICRA), Karlsruhe (Germany), 2013.
4. **I. Yildiz**, A. Savenko, D. M. A. Mackenzie, D. H. Petersen, O. Hansen, K. Nilson, P. Bøggild; *Bimorph bending for fast mounting of nanolithographically designed scanning probe tips*. In preparation.